UNIVERSITY OF CALIFORNIA
SANTA CRUZ

BENEATH THE SURFACE OF GIANT PLANETS: EVOLUTION, STRUCTURE, AND COMPOSITION

A dissertation submitted in partial satisfaction of the
requirements for the degree of

DOCTOR OF PHILOSOPHY

in

ASTRONOMY AND ASTROPHYSICS

by

Neil L Kelly Miller

March 2013

The Dissertation of Neil L Kelly Miller
is approved:

Jonathan Fortney, Chair

Professor D. Lin

Professor P. Garaud

Professor P. Bodenheimer

Tyrus Miller
Vice Provost and Dean of Graduate Studies

Table of Contents

List of Figures

List of Tables

Abstract

Beneath the Surface of Giant Planets: Evolution, Structure, and Composition

by

Neil L Kelly Miller

This thesis is focused on utilizing the combination of giant exoplanet mass via radial velocity observations and radius via transit observations to study their structure and evolution. In Chapter 2, Giant planet thermal evolution models are coupled to tidal evolution dynamics, including orbital evolution and planet interior heating. Viable tidal evolution histories are explored to explain inflated radii of hot Jupiters. Tidal evolution is demonstrated to be a viable heating mechanism in some cases, but for other cases it can not explain the large radii. The thesis continues in Chapter 3 by exhibiting cases when the tidal-thermal evolution model, including energy-limited mass loss, can be used to infer interior properties and demonstrate a possible evolution history. Specifically, I utilize the thermal evolution models to examine planets CoRoT-2b, CoRoT-7b, and the Kepler-11 system. In Chapter 4, planets with lower incident irradiation are examined to infer the heavy element composition inside a range of planets. These planets don't appear to be significantly inflated by the unknown radius inflation mechanism, thus the mysterious mechanism can be ignored. It is shown that the heavy element mass inside these planets correlates with the metallicity of the star. The heavy element mass also correlates with the mass of the planet. However, the heavy element enrichment is inversely related to the mass of the planet. In the final chapter, I develop a mixing

equation of state code for the MESA stellar evolution project. This code is developed with the intention of studying inhomogeneous thermal evolution of planets.

This thesis is dedicated

to my parents

Acknowledgments

UC Santa Cruz has been an excellent place for me to pursue my studies as it has been an extremely supportive environment. My Ph.D. Advisor, Jonathan Fortney, was consistently supportive and encouraging throughout the ups and downs of my research. Jonathan has lead a research group at Santa Cruz that is exploring multiple exciting aspects of exoplanet science and does so by being as inclusive to as many people as possible.

Many of the people that I have had the opportunity to collaborate with were not from UC Santa Cruz or directly part of our research group. I believe that we benefit by having collaborative and friendly relationships with other research groups. Inside the Forney research group, I've really enjoyed working beside Megan Shabram, Eric Lopez, Caroline Morley, Philip Nutzman, Angie Wolfgang, Eliza Kempton, Katie Morzinski, and Nadine Nettelmann.

I have greatly benefited by conversations and discussions with Doug Lin, Peter Bodenheimer, and Pascale Garaud about this work and appreciate their help in finishing this PhD. Pascale consistently promoted a highly rigorous approach to science, which is an example I aspire to. Doug always is able to find new and inspiring problems to explore, pushing me to think beyond my existing understanding. Peter has always provided exceptionally kind encouragement and guidance from the first stellar structure model through my defense.

I also appreciate the opportunity to work with Bill Paxton at KITP, Santa

Barbara, who was always available regarding MESA. I think this project has an exciting future involving people from many parts of the astrophysics community, which is only possible due to Bill's hard work.

An important component of my experience as a graduate student in this department that I really enjoyed was the high degree of interaction between other graduate students as well as between faculty, postdocs, graduate students and undergrads. Part of the reason for this is a tradition of community spirit and the willingness to try new ideas. There is an overall attitude of volunteerism in the community at all levels makes this a special place. People often are willing to ask, what can we do to make this department a better place? Some examples that come to mind are the Vox Charta web site for morning coffee developed by James Guillochon, the Ski weekend championed by Sandy Faber, the grad retreat, the grad store, the prospective visit, or the Friday social hour. These are efforts create tangible benefits that make our community closer and were made possible through the efforts of volunteers and people that took initiative. It is nicely summarized as

"Create your own reality"

–Kevin Schlaufman

I hope that this attitude and tradition continues to be enjoyed by future members of the community.

As a graduate student, I have been given the opportunity to meet and get to know a lot of interesting and good people and made my experience in Santa Cruz special.

My roommates Luke Roberts and Kevin Schlaufman have been very good friends to me and provided a lot of support and encouragement. Its amazing how many hours you spend with your officemates. I've really enjoyed the company and friendship of Laura Lopez and James Guillochon who were my officemates for the longest time.

Chapter 1

Introduction

We are currently in a fascinating epoch in human history. Through technology and methodology advances, astronomers are beginning to detect and characterize planets outside of our home Solar System for the first time. By systematically studying the population of exoplanets, we are able to test our hypotheses for how planets form. Often, we have found unexpected behavior that forced us to broaden our preconceptions.

The first important method of observing exoplanets is through the "radial velocity method" - where the spectroscopic Doppler motion of the planet's host star is observed over time. As the planet travels through its orbit, its gravitational pull periodically and systematically accelerates the star. The observer is able to see how the star's velocity in the line-of-sight or "radial" coordinate is changing as a result of this interaction. This information can be used to constrain the planet's mass, orbital period, and orbital eccentricity. The first exoplanet discovered using this method was around the star 51 Pegasi (Mayor & Queloz 1995), a 4.23 day period orbit with mass of

0.46 $M_{\rm J}$. This revealed a class of close-in hot Jupiters, which was unexpected as there is no similar planet in our own system.

A second method, the transit method, creates an additional constraint on the properties of planets. This method is possible when the planet passes between its parent star and our line of sight. By carefully monitoring the brightness of the star over time, observers are able to constrain the planet's radius. In some cases, it is also possible to detect the secondary eclipse - when the planet's light is blocked by the parent star. This can be difficult because the surface temperature of the planet is typically much lower than that of the parent star. Observing the planet's radius works well in combination with observing its mass through the radial velocity method because it allows us to infer the planet's density and thereby its composition. Again, when astronomers first observed HD 209458 b, they found something unexpected. The planet's radius was unexpectedly "inflated" (Charbonneau et al. 2000) which has resulted in theorists postulating multiple physical mechanisms to explain the phenomenon.

The transit method has recently become extremely productive with the introduction of the *Kepler* space telescope (Borucki et al. 2011). *Kepler* is systematically observing 100,000 stars and an automatic software pipeline searches for transit events within the data. This is an ongoing effort that is currently discovering a wide variety of interesting systems, extremely efficiently. Being a space telescope, Kepler has been able to find smaller radii planets than were previously detectable from the ground. The Kepler community is fairly focused on trying to find an Earth-like analogue as finding the first such object would be extremely exciting for the general public.

The combination of the transit method determination of the planet's radius and the radial velocity measurement of the planet's mass allows us to study the structure and thermal evolution of exoplanets. This is a central theme of this thesis - by combining both types of observations we are able to understand aspects that would not be possible otherwise. For example, this allows us to probe information about the energy budget and the interior composition.

1.1 The Solar System Giant Planets

Although exoplanets are the new exciting arena where observers are pushing the limit, it is also useful to continue to study the giant planets within our own Solar System. These are interesting in their own right as they are members of our home system. Studying these planets adds scientific value because we can perform many detailed measurements that will not be possible for exoplanets. For example, the Galileo probe was sent into Jupiter to measure the composition of the outer atmosphere. This probe verified that Jupiter's heavy element composition is enriched by a factor of 4. For Solar System planets we can observe exquisite features such as storms, band structures, waves, and rings.

Orbiting spacecraft also are able to measure a planet's gravitational moments - which inform astronomers about the interior density distribution. Oscillations in the planet may also be detectable - which would probe the interior structure. There are many uncertainties that remain. What is the composition profile of the interior of these

planets? The equation of state itself is also uncertain - meaning that the models are imperfect.

1.2 From Individual Systems to Samples

Often the pioneering observations have occurred by studying individual systems in detail such as HD 209458 b. Observers often focus significant resources on the most interesting cases - pushing the limits of what can be understood with current instruments. This focused approach allows us to learn details about these specific systems that would not be possible to do for a larger sample. For example, secondary eclipse observations allow observers to construct broadband spectra of the atmosphere of the planet. In other cases, frequent radial velocity observations on a specific star allow observers to find signals that would not be possible for a broad sample.

It is also important to try to characterize the sample of planets to understand the general processes that are important for formation and evolution. The study of populations often will requires performing more, less specialized observations. Typically the methods used here are able to utilize the expertise that is gained through studying individual systems.

At this point in time, astronomers have collected a broad sample, perhaps somewhat inhomogeneously selected, of planets at a range of orbital radii, planet radii, and planet mass. In Figure 1.1, the most recent distribution of observed planets is plotted (Wright et al. 2011). The colored planets are those with observed radii, while

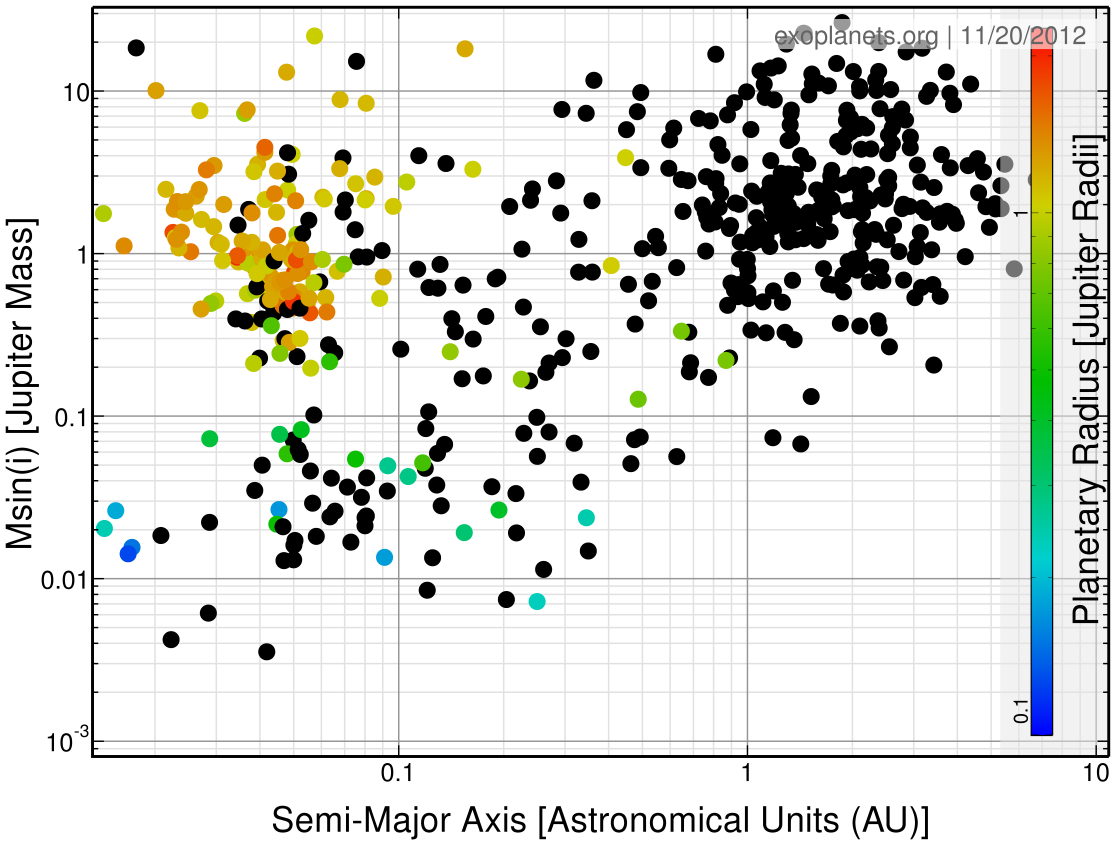

Figure 1.1: Current observed planets by Semi-major axis and mass, colored by radius. The black points are those where a radius is not measured. This figure was generated from Exoplanets.org

the black planets are only observed with radial velocities. The over-densities and under-densities are due to a combination of selection effects convolved with the true distribution of exoplanet properties.

Models by Ida & Lin (2010) or Mordasini et al. (2009) make predictions on the distribution of planets' orbital parameters and planet mass as a function of properties of the star such as the star mass, age, or metallicity. These models are controlled by

assumptions about the physical processes of planet formation. Therefore, the observed distribution of planets places a constraint on formation models. This continues to be an area of ongoing research, but a picture of the planet formation process is emerging.

Giant planets are generally believed to be formed through core accretion near the ice line. In this process, a solid core of heavier elements first forms. When the mass exceeds a critical mass, typically around 10 M_E, disk gas begins to accrete. This is the time when the escape velocity of the planet exceeds the thermal velocity of gas in the disk. When the mass of the core is comparable to the mass of the gas envelope, the accretion from the disk accelerates rapidly (Mizuno 1980, Pollack et al. 1996). If this formation model is correct, it would predict that all giant planets initially have a core of heavy elements in their center.

An alternate formation scenario is called the "gravitational instability" formation mechanism. In this model, a gravitational disk instability develops - typically requiring a relatively massive disk (Boss 2001b;a). This instability causes gas to coagulate over a dynamical time. This difference of formation model will have an impact on the distribution of heavy elements inside the planet as this model does not require the existence of a core. However, heavier elements may arrive at later times through accretion of asteroids, comets, or even planetary sized objects after the initial formation. Therefore, gravitational instability doesn't preclude the existence of enrichment in heavy elements relative to the parent star (Helled et al. 2006, Helled & Schubert 2009, Helled et al. 2010).

Giant planets can only form via core accretion near the ice line at multiple

AU away from their parent star. If this is how planets form, it is necessary to explain how there exist many giant planets at significantly closer distances. There are a few migration mechanisms by which the orbit of the planet can transition to a lower energy orbit.

1. **Disk Migration** - Through the coupling of the primordial disk with the young proto-planets, tidal tails in the disk may exert torques on the planet causing it to migrate inward (Ward 1997a;b, Lin et al. 1996). In this mechanism, the disk damps out the planet's eccentricity so planets that migrated would be expected to initially have circular orbits.

2. **Planet Scattering** - In this mechanism multiple planets in nearby orbits may disrupt each other's orbits resulting in one planet having a much lower semi-major axis and high eccentricity (Rasio & Ford 1996), which may be damped down to a lower eccentricity via tidal interaction with the star. This mechanism predicts many planets with high eccentricities and explains why the planets at small semi-major axis are preferentially circularized. A difficulty with this mechanism is that the planets must be circularized in such a way that they are not disrupted.

3. **Kozai Mechanism** - In the case when a planet forms around a star with a binary companion, the planet's semi-major axis may be reduced by the combination of secular interactions between the planet and binary as well as tidal dissipation between the planet and its host star (Fabrycky & Tremaine 2007). This mechanism also predicts the creation of highly eccentric planets and explains how the closest

planets would be circularized. It also predicts a connection between the presence of a binary and eccentric planetary orbits. This mechanism also produces orbits that are misaligned relative to the spin of the host star. This is consistent with observations of misaligned systems via the Rossiter-McLaughlin effect (Fabrycky & Winn 2009).

4. **Secular Chaos** - If there are multiple planets that are closely spaced, they may be able to excite each other's eccentricity through secular interactions (Wu & Lithwick 2011). In this picture, hot Jupiters are being migrated continuously over Gyr time-scales.

1.3 Physical Processes in the Evolution of Giant Planets

After formation, we are interested in how giant planets' interior structure evolves over Gyr time-scales. The presence of transit observations, giving us the radius of the planet, in combination with the planet's mass gives us the planet's average density which gives us a simple measure of the interior of the planet.

The equation of state describes the relationship between thermodynamic quantities such as density, temperature, pressure, internal energy, and entropy. The equation of state is centrally important for determining the hydrostatic balance between gravity and the pressure gradient. This has a direct impact on the observed planet radius. In combination with the chemical gradient, the equation of state will also determine the density distribution in the interior of the planet, which can be constrained for Solar Sys-

tem planets via gravitational moments. The equation of state acts as a closure to the hydrostatic balance equations by modeling the material properties, which are ultimately determined by particle interactions.

The hydrostatic equations that apply in the planetary case are as follows. These equations assume that the planet is spherically symmetric

$$\frac{\partial r}{\partial m} = \frac{1}{4\pi r^2 \rho} \tag{1.1}$$

$$\frac{\partial P}{\partial m} = -\frac{Gm}{4\pi r^4} \tag{1.2}$$

$$\frac{\partial l}{\partial m} = \epsilon - c_P \frac{\partial T}{\partial t} - \frac{\delta}{\rho}\frac{\partial P}{\partial t} \tag{1.3}$$

$$\frac{\partial T}{\partial m} = -\frac{GmT}{4\pi r^4 P}\nabla \tag{1.4}$$

where $\delta \equiv -(\partial \ln \rho / \partial \ln T)_P$, $\nabla \equiv d\ln T / d \ln P$. These standard equations are derived in Kippenhahn & Weigert (1990). The equation of state provides the relationships

$$\rho = \rho(P, T, X_i) \tag{1.5}$$

$$c_P = c_P(P, T, X_i) \tag{1.6}$$

$$\nabla_{ad} = \nabla_{ad}(P, T, X_i) \tag{1.7}$$

$$\tag{1.8}$$

The equation of state is also important in that the specific heat, $c_P \equiv (dq/dT)_P$, determines the ratio between heat added per unit mass and changes in the temperature. Therefore, the equation of state not only determines the planet's density profile, but will determine how that profile changes when energy is lost (or input).

Typically, giant planets are convective in their interior. This property is pri-

marily determined by the opacity and to a lesser extent the equation of the state, at the pressures and temperatures found in planet interiors. Convection is the process by which energy is transported via large scale advection rather than a diffusive process. These fluid motions are driven by the convective instability. This is the condition where adiabatically rising fluid in pressure equilibrium with the surrounding profile, decreases in density faster than the surrounding medium. This causes the fluid element to experience buoyancy and accelerate upward. This fluid instability then drives turbulence at large scales.

The net effect is that planet interiors are typically fairly close to adiabatic - meaning the entropy is roughly constant throughout the interior of the planet. This property can be used to construct simple structure and evolution models by building hydrostatic structures from adiabatic pressure-density profiles. The profile may not be adiabatic if there are composition gradients that inhibit the thermal instability.

Composition gradients can inhibit convection if there is a decreasing mean molecular weight moving away from the center of the planet (Stevenson 1985, Leconte & Chabrier 2012). These mean molecular weight gradients may arise from either core erosion or through Helium rain (Stevenson & Salpeter 1977b;a, Fortney & Hubbard 2003; 2004).

The planet's atmosphere is important to the evolution of planets in that it regulates the flow of energy out of the planet. The structure of the atmosphere is heavily dependent on the incident radiation from the parent star. This incident radiation can inhibit the rate at which energy leaves the planet, which ultimately results in larger

planet radii. Grids of non-gray model atmospheres (Fortney et al. 2007a) can be used to connect interior properties (e.g., T at 1000 bars or the specific entropy), surface gravity, and $T_{\rm Int}$, the flux from below. Alternatively, a simple analytic treatment (Guillot 2010) can capture much of this behavior as well.

The planet's atmosphere is also important since in some cases it can be directly observed. Observing the spectra of the atmosphere can constrain the composition of the atmosphere and atmosphere thermal profile. The observed temperature of the planet is useful for determining the age of the system in the case of directly observed planets at large distances from their parent star.

The planet's orbit may also evolve over Gyr time-scales due to either secular interactions with other planets in the system or through tidal interaction with the parent star. As will be described in Chapter 2, tidal evolution between the parent star and hot Jupiter can transport the planet closer to the star. This may in some cases result in the complete destruction of the planet as it is engulfed into its parent star (Jackson et al. 2009, Gu et al. 2003, Li et al. 2009). Tides on the planet may act to also heat the interiors of these planets and temporarily inflate their radius, as we will show in Chapter 2. However, we find that for many systems, the tidal evolution model alone has difficulty explaining both the observed orbital properties and the observed radius. As many of these planets currently have low eccentricity orbits, it is difficult to explain an inflated radii as planets contract fairly quickly, once their orbits have circularized. In Chapter 3, the thesis continues with an examination of three interesting systems: CoRoT-2b, CoRoT-7b, and Kepler-11.

This thesis then goes on in Chapter 4 to show how transit observations in conjunction with radial velocity masses can be used to measure the composition of giant planets for low incident flux planets. All of the inflated planets appear to have an average incident flux larger than 2×10^8 ergs / s / cm^2. Since the heating mechanism is poorly understood it is difficult to constrain the heavy element mass for these inflated planets. For the low incident flux planets we can assume that the heating process is negligible. This allows us to constrain their compositions through structure and evolution models using the observed radii, masses, ages, and incident fluxes.

Chapter 5 presents first steps toward a more sophisticated planet thermal evolution model by extending the open source stellar evolution code MESA. MESA was chosen as it is an open source code that has been highly tested over a broad range of stellar evolution applications. As described above, composition gradients may be essential for understanding observed properties of giant planets inside our Solar System and in the exoplanets arena. For example, the luminosity of Uranus is significantly lower than that of Neptune, which may be a result of composition gradients in the interior of Uranus. In the area of exoplanets, composition gradients may sufficiently inhibit convection of close-in Jupiter class planets, explaining a currently observed "inflated" radius (Chabrier & Baraffe 2007). Towards this objective, this chapter describes the construction of an equation of state code that uses the additive volume method to add multiple species, each independently described by their own equation of state. This code has been developed to be a flexible tool that is entirely accessible for other researchers.

The overall big picture questions that this thesis is interested in are as follows

- What inflates Hot Jupiters? Can they be explained by a single process such as tidal heating or are there multiple mechanisms at work?

- Is the composition of Solar System giant planets consistent with those we observe outside the Solar System? Is there anything unique about Jupiter and Saturn's heavy element enrichment? How does the composition of a planet vary with other properties such as the metallicity of the star or mass of the planet?

- Is the inferred composition of giant exoplanets consistent with the core-accretion formation scenario?

- What is the role of composition gradients in the evolution of giant planets?

With the continued collection of data about our Solar System and exoplanets and utilizing improved theoretical models, there remains significant opportunity to further our understanding of these interesting questions.

Chapter 2

Coupled Thermal and Tidal Evolution of Giant Expolanets

2.1 Abstract

We examine the radius evolution of close-in giant planets with a planet evolution model that couples the orbital-tidal and thermal evolution. For 45 transiting systems, we compute a large grid of cooling/contraction paths forward in time, starting from a large phase space of initial semi-major axes and eccentricities. Given observational constraints at the current time for a given planet (semi-major axis, eccentricity, and system age) we find possible evolutionary paths that match these constraints, and compare the calculated radii to observations. We find that tidal evolution has two effects. First, planets start their evolution at larger semi-major axis, allowing them to contract more efficiently at earlier times. Second, tidal heating can significantly inflate

the radius when the orbit is being circularized, but this effect on the radius is short-lived thereafter. Often circularization of the orbit is proceeded by a long period while the semi-major axis slowly decreases. Some systems with previously unexplained large radii that we can reproduce with our coupled model are HAT-P-7, HAT-P-9, WASP-10, and XO-4. This increases the number of planets for which we can match the radius from 24 (of 45) to as many as 35 for our standard case, but for some of these systems we are required to be viewing them at a special time around the era of current radius inflation. This is a concern for the viability of tidal inflation as a general mechanism to explain most inflated radii. Also, large initial eccentricities would have to be common. We also investigate the evolution of models that have a floor on the eccentricity, as may be due to a perturber. In this scenario we match the extremely large radius of WASP-12b. This work may cast some doubt on our ability to accurately determine the interior heavy element enrichment of normal, non-inflated close-in planets, because of our dearth of knowledge about these planet's previous orbital-tidal histories. Finally, we find that the end state of most close-in planetary systems is disruption of the planet as it moves ever closer to its parent star.

2.2 Introduction

The precise mass and radius measurements for transiting exoplanets provide information about the planets' interior structure and composition, which are often apparently unlike that of Jupiter and Saturn. Indeed, it is the incredible diversity of

measured radii of transiting planets that has been most surprising. In the solar system, Jupiter and Saturn differ in mass by a factor of three while their radii differ by only 18%. However, amongst exoplanets, planets with the same mass can differ in radius by a factor of two. A hope amongst planetary astrophysicists was that the measurement of the mass and radius, when compared to models, would cleanly yield information on planetary interior composition. Although there are clearly examples where this has been done successfully, including heavy element rich planets such as HD 149026b (Sato et al. 2005, Fortney et al. 2006) and GJ 436b (Gillon et al. 2007), in general modelers have been foiled by planets with very large radii, larger than can be accommodated by "standard" cooling/contraction models.

Considerable work has been done in the past several years to understand the large radii of some planets, as well as the radius distribution of the planets as a whole. Explanations for the "anomalously" large planets have fallen into three categories: those that are a current or recent additional internal energy source, which has stalled the interior cooling and contraction (Bodenheimer et al. 2001, Guillot & Showman 2002, Bodenheimer et al. 2003, Gu et al. 2003, Winn & Holman 2005, Liu et al. 2008, Jackson et al. 2008b, Ibgui & Burrows 2009), those that instead merely delay the contraction by slowing the transport of interior energy (Burrows et al. 2007, Chabrier & Baraffe 2007), and those that invoke various evaporation mechanisms (Baraffe et al. 2004, Hansen & Barman 2007). These are briefly reviewed in Fortney (2008).

Tidal heating as an explanation for these large-radius planets was suggested by Bodenheimer et al. (2001) for HD 209458b and has been revisited frequently by

other authors (e.g. Bodenheimer et al. 2003, Winn & Holman 2005, Liu et al. 2008, Gu et al. 2003; 2004, Jackson et al. 2008a;b, Ibgui & Burrows 2009). We note that the mechanism of heating by obliquity tides (Winn & Holman 2005) has been cast in considerable double by several authors (Levrard et al. 2007, Fabrycky & Tremaine 2007, Peale 2008).

At this time, tidal heating by orbit circularization is generally believed to be the most important type. The largest uncertainties in the standard tidal theory is the "tidal Q" value, a standard parameterization of the rate of tidal effects. In this work, we use the standard notation for the planet tidal Q value as $Q'_{\rm p}$ and the stellar tidal Q value as $Q'_{\rm s}$. Jupiter's $Q'_{\rm p}$ value has been constrained to be between 10^5 and 10^6 (Goldreich & Soter 1966). For tidal heating by circularization to take place, the planet must either initially have an eccentric orbit or the system must be driving the eccentricity of the planet at recent times.

The former scenario would have the following qualitative stages. The planet is left with an eccentric orbit through planet-planet interactions (Rasio & Ford 1996, Chatterjee et al. 2008, Ford & Rasio 2008). Tides on the star gradually reduce the semi-major axis. These tidal effects accelerate as the semi-major axis decreases. Tides on the planet become more important and the planet's orbit circularizes; at the same time depositing orbital energy into the planet's interior. Scattering/tidal evolution models of this sort were recently computed by Nagasawa et al. (2008). At this point, the system might be observed to have a fairly circular orbit and a larger-than-expected radius. Ibgui & Burrows (2009) use a coupled tidal-thermal evolution model, quite similar to

the one we present here, to show that this scenario might be possible for the HD 209458 system, and by extension, many hot Jupiter planets. Such a model is necessary to self-consistently explain a planet's radius in this picture. One potential issue with this scenario is that it can require large-radius planets to be observed at a "special time" since after the orbit is circularized, the planet may rapidly contract.

Alternatively, some planets might be found in an equilibrium state where their eccentricity is being forced by a third body while at the same time tides on the planet are damping the eccentricity (Mardling 2007). This is an attractive explanation because the planet might be found in an inflated state for a long period of time. Previously, Bodenheimer et al. (2001) calculated the tidal power required to maintain the radius for HD 209458 b, Ups And b, and Tau Boo b, as a function of the assumed core size, in a stationary orbit. Recently, thermal evolution calculations with constant heating have been performed for TrES-4, XO-3b and HAT-P-1b by Liu et al. (2008), who placed constraints on $\bar{e}^2/Q'_p$ - where $\bar{e}$ is the recent time-averaged eccentricity of the orbit. These calculations are useful for estimating the required recent tidal heating. In some cases, where the eccentricity is non-zero and a perturber is necessary to invoke, then this constant heating picture might accurately describe the recent thermal history of the planet. In many cases the eccentricity is observed to be close to zero, which either implies that a) the planet's eccentricity is at a non-zero equilibrium, but the planet's $Q'_{\rm p}$ value is much smaller than inferred from Jupiter or b) the planet's orbit is circularized and this calculation does not apply.

Clearly it is important to accurately measure the eccentricity of inflated sys-

tems to determine if either scenario is plausible. For many transiting systems, the eccentricity has been only weakly constrained with several radial velocity points and it is very difficult to distinguish a small eccentricity from one that is truly zero (Laughlin et al. 2005). For systems with an observed secondary eclipse, stronger upper limits on eccentricity can be found based on the timing of the eclipse (Deming et al. 2005, Charbonneau et al. 2005, Knutson et al. 2009). Note that secondary eclipse timing only constrains $e \cos \Omega$ so it is possible that some of these systems have much larger eccentricity, but it is unlikely.

The above possibilities are also consistent with the popular planet formation and migration theories. These planets form while the protoplanetary disk is still present at much larger orbital distances and migrate early in their life to small orbital distances (e.g. Lin et al. 1996). After this initial phase, tidal evolution between the star and the planet occurs on Gyr time scales. The migration mechanism is important because it determines the initial orbital parameters for tidal evolution. There are multiple postulated migration mechanisms.

1. Planet-disk interaction: Gravitational interactions between the planet and protoplanetary disk can exert torque on the planet (Ward 1997a;b). These mechanisms tend to circularize the planet's orbit very early on and decrease the semi-major axis. The disk migration time scales is significantly shorter than the lifetime of the disk, as described in Papaloizou et al. (2007) and references therein.

2. Planet-planet interaction: Gravitational interactions with other nearby planets

can transfer orbital energy and angular momentum between the two bodies. This can result in quickly decreasing or increasing the orbital distance of one of the planets as well as producing non-zero initial eccentricity orbits. Using N-body simulations, (Rasio & Ford 1996, Weidenschilling & Marzari 1996, Chatterjee et al. 2008, Ford & Rasio 2008) have shown that this effect can be important and can result in the inner bodies having initial eccentricity as large as 0.8, before tidal damping ensues.

3. The Kozai mechanism occurs when a planet's host star has a binary companion that exchanges angular momentum with the planet. In combination with tidal dissipation from tides on the planet induced by the host star, the planet's orbit may decrease to lower semi-major axis (**?**).

4. Secular Chaos may occur if there are multiple closely spaced planets with non-zero initial eccentricity. Its possible that this mechanism acts in combination with tidal dissipation to deposit energy into the interior of giant planets (Wu & Lithwick 2011).

There are also a handful of single transiting planets that have non-zero eccentricity today, which can be explained by either planet-planet scattering or the Kozai mechanism. It is also suggestive that many of these eccentric planets are more massive and have longer circularization time scales. Since the circularization time is longer for massive planets, this observation is consistent with the idea that planets of all masses can have large initial eccentricity, but that the lower mass planets have circularized

while the massive planets may still be circularizing.

We expect that all of these mechanisms do happen to some extent. Therefore, we assume that a wide range of initial orbital parameters are possible, and we following the orbital and structural evolution of planets from a wide range of possible initial eccentricities, as described below. In the absence of a theory to predict likely initial eccentricities for a given planetary system, we seek to understand the physics of the evolution from a variety of initial states.

Most of the detected transiting planets currently have small eccentricities consistent with zero. These can be explained by either migration mechanism. If the planet migrated through planet-disk interactions, then it would have zero eccentricity when tidal evolution began. If the planet migrated through planet-planet interactions, then the orbit may have circularized due to tides on the planet.

2.3 Model: Introduction

In this work we would like to test the possibility that tidal heating by orbit circularization can explain the transit radius observations for each particular system. A necessary condition for this model is that a self-consistent evolution history can be found that agrees with all of the observed system parameters. To check this condition, we forward-evolve a coupled tidal-thermal evolution model over a large grid of initial semi-major axis and eccentricity for each system. We perform this test for $Q'_{\rm s} = 10^5$, $Q'_{\rm p} = 10^5$ and $Q'_{\rm s} = 10^5$, $Q'_{\rm p} = 10^{6.5}$. Also, for each system with non-zero current eccentricity,

we emulate an eccentricity driving source by performing runs with an eccentricity floor equal to the observed value. Later we also explore some higher Q'_s cases.

To properly understand the planet's thermal evolution, it is necessary to couple the planet thermal evolution to the orbital-tidal evolution. Generally planets with initial semi-major axis of 0.1 AU or less will spiral into the star in Gyr timescales (Jackson et al. 2008a). This has a large impact on the incident flux on the planet, and therefore the loss of intrinsic luminosity of the planet. For some systems, this more efficient cooling at early times makes it possible to achieve smaller radii at the present. As the planet moves closer to the star, the tidal effects accelerate. If the orbit is eccentric, then at some point the planet's orbit undergoes a period of circularization. At this time a significant amount of orbital energy is deposited into the planet, which increases its radius. The question of this work is whether, at this stage, the system's observables (a, e, age, R) can simultaneously be achieved in the model. After this stage, the planet may lose mass by Roche lobe overflow (Gu et al. 2003), which can temporarily prevent the planet from falling into the star. However, the planet's destiny is to fall into the star (Levrard et al. 2009, Jackson et al. 2009). These final stages of the planet's life, including the mass loss stage, are not modeled in this work.

We typically find that tides on the star are the dominant source of semi-major axis evolution (Jackson et al. 2008a;b). When the eccentricity is large and damping, the tides on the planet can be the dominant semi-major axis damping source (Jackson et al. 2008a, Ibgui & Burrows 2009). After surveying our suite of systems, we find that tidal heating can usually provide sufficient energy to inflate planetary radii as large as

observed, but we do not always find an evolutionary history where the radius, semi-major axis, eccentricity and age all simultaneously fall within the observed error bars. Regardless, we find that tidal processes are an important aspect of planet evolution, particularly for hot Jupiter systems.

2.4 Model: Implementation

The Fortney et al. (2007b) giant planet thermal evolution model has been coupled to the Jackson et al. (2008b) tidal evolution model. Therefore, the semi-major axis, eccentricity, and radius of the planet all evolve simultaneously. The tidal power is assumed to be deposited uniformly into the envelope of the planet. The planet structure model is assumed to be composed of four parts:

1. a 50% rock/ 50% ice core (by mass) with the ANEOS equations of state (Thompson 1990). The core does not participate in the thermal evolution of the planet, as in Fortney et al. (2007b).

2. a H/He envelope with $Y = 0.27$, which uses the equation of state of Saumon et al. (1995). The envelope is assumed to be fully convective and thus has constant specific entropy throughout. At each time step the envelope is assumed to be in hydrostatic equilibrium.

3. a series of radiative-convective, equilibrium chemistry, non-grey atmosphere models described in more detail in Fortney et al. (2007b) and Fortney et al. (2008). These grids are computed for the incident fluxes at 0.02, 0.045, 0.1, and 1 AU

from the Sun. This correctly determines the atmospheric structure and luminosity of the planet as a function of the planet's surface gravity, incident flux from the host star, and interior specific entropy. In cases where the planet migrates to a semi-major axis with more incident flux than the innermost grid, then the boundary condition at the innermost grid is used.

4. an extension of the atmosphere to a radius where the slant optical depth in a wide optical band (the *Kepler* bandpass) reaches unity. Therefore, all plotted radii are at the "transit radius," as discussed by several authors (Hubbard et al. 2001, Baraffe et al. 2003, Burrows et al. 2003). The slant optical depth as a function of pressure is computed with the code described in Hubbard et al. (2001) and Fortney et al. (2003). We have found that the atmosphere height approximately follows the following relation

$$h = 10^{8.74} \frac{T_{eff}}{g} \tag{2.1}$$

where h is the height in cm of the atmosphere from 1 kbar (approximately the depth where the radiative/convective zone boundary lies) to 1 mbar (where the planet becomes optically thin), g is the planet's surface gravity (cgs), and $T_{\rm eff}$ is the effective temperature in Kelvin. Taking into account this atmosphere height is significant when the planet has low gravity or high effective temperature. In Fortney et al. (2007b), the radii at 1 bar were presented.

The orbital-tidal evolution model is described in detail by Jackson et al. (2008b; 2009) and references therein. The equations used in this work are

$$\begin{aligned}
\frac{1}{a}\frac{da}{dt} &= -\left[\frac{63\sqrt{GM_{\rm s}^3}R_p^5}{2Q'_{\rm p}M_p}e^2\right. \\
&\quad \left. + \frac{9\sqrt{G/M_{\rm s}}R_{\rm s}^5M_p}{2Q'_{\rm s}}\left(1+\frac{57}{4}e^2\right)\right]a^{-13/2} \qquad (2.2)\\
\frac{1}{e}\frac{de}{dt} &= -\left[\frac{63\sqrt{GM_{\rm s}^3}R_{\rm p}^5}{4Q'_{\rm p}M_p} + \frac{225\sqrt{G/M_{\rm s}}R_{\rm s}^5M_p}{16Q'_{\rm s}}\right]a^{-13/2} \qquad (2.3)\\
P_t &= \frac{63}{4}\left[(GM_{\rm s})^{3/2}\left(\frac{M_{\rm s}R_{\rm p}^5e^2}{Q'_{\rm p}}\right)\right]a^{-15/2} \qquad (2.4)
\end{aligned}$$

where a is the semi-major axis, e is the eccentricity, and P_t is the tidal power deposited into the planet. This model attempts to describe tidal heating only by orbit circularization and ignores other forms of tides such as spin synchronization or obliquity tides, which are not believed to be as important. This model assumes that the star is rotating slowly relative to the orbit of the planet and is second order in eccentricity. Therefore the evolution histories that include periods when the orbit has high eccentricity should be regarded with caution. Because there is a lot of other uncertainty with regard to tidal theory, we choose to use this simple model instead of more complex models such as Wisdom (2008). For at least 1 of the 45 systems, HAT-P-2, the planet-star system may be able to achieve a double tidally locked equilibrium state (star is tidally locked to the planet and the planet is tidally locked to the star) as shown by Levrard et al. (2009); in this system it is not a good assumption that the star is rotating slower than the period of the orbit. However, Levrard et al. (2009) find that this assumption is valid for most stars. We find that tidal heating is largest where e is not particularly large ($\lesssim 0.4$ falling

towards zero) so this theory suffices for our purposes. $Q'_{\rm p}$ is the tidal Q parameter of the planet and $Q'_{\rm s}$ is the tidal Q parameter of the star. In this work we have predominantly investigated cases when $Q'_{\rm p} = Q'_{\rm s} = 10^5$ as well as the case of $Q'_{\rm p} = 10^{6.5}$, $Q'_{\rm s} = 10^5$. Since the Q value is in principle a function of the driving frequency (Ogilvie & Lin 2004), amplitude of the distortion, and internal structure of the body, the Q value for close-in extra solar giant planets is potentially not equal to the Q value for Jupiter. If the Q value is a very "spiky" function of the driving frequency, then the system might spend a lot of time in a state where the tidal effects are occurring at a slow rate and quickly pass through states where tidal effects are rapid. The stellar Q value is typically estimated through the observed circularization of binary stars orbits, but has also been estimated by modeling the dissipation inside of a star (Ogilvie & Lin 2007).

We assume that the tidal power is uniformly deposited into the envelope of the planet. The net energy loss is given by the following equation:

$$(L - P_t)\Delta t = \int T \Delta S dm. \tag{2.5}$$

where L is the luminosity at the planet's surface, Δt is some small nonzero time step, and S is the specific entropy. If $P_t > L$, then the planet's envelope will be increasing in entropy and the planet's radius will increase. More typically, $P_t < L$ and the planet's entropy is decreasing and thus the planet is contracting. The power ratio P_t/L is a useful measure of how important tidal effects are. It clearly indicates whether there is a net energy input (ratio larger than unity) or net energy loss (ratio smaller than unity).

For a given radius, assumed core size and average incident flux of the planet, $\dot{R}_p \propto -L_{net}$. Therefore, if we calculate $\dot{R_{NH}}$, the radius contraction rate when there is no internal heat source, we can use the following relationship to calculate $\dot{R}_p$ when there is an assumed P_t tidal heating (or an input power of another source).

$$\frac{\dot{R}}{\dot{R_{NH}}} = \frac{L - P_t}{L} \tag{2.6}$$

Due to tidal migration the incident flux upon the planet increases with time. Based on the planet's incident flux at a given time, we interpolate in the 4 grids which include the incident flux level from the Sun at 0.02, 0.045, 0.1, and 1 AU. Here we neglect the more minor effect that parent star spectra can differ somewhat from that of the Sun.

In order to examine all the plausible evolutionary tracks for each of the 45 transiting planets studied, we modeled their thermal evolution over a range of

1. initial semi-major axis: the observed semi-major axis to five times the observed value.

2. initial eccentricity: from 0 to 0.8.

3. core mass: 0, 10 $M_\oplus$, 30 $M_\oplus$, 100 $M_\oplus$. For very massive planets we also consider core masses of 300 and 1000 $M_\oplus$. Except for GJ 436b, HAT-P-11b, and HD 149026b, the core was required to be at most 70% of the mass of the planet. For GJ 436b, we sample up to 21 $M_\oplus$and for HAT-P-12, we sample up to 23 $M_\oplus$.

Each of these possible evolution histories were run until either a) the time reached 14 Gyr, b) the entropy of the envelope became larger or smaller than the range

of entropy values in the grid of hydrostatic equilibrium structures, or c) the planet reaches a small orbital distance $\sim R_s$ (realistically, the planet would be disrupted before this stage, but in this work we do not model the mass loss process).

For each run, we searched the evolution history during the estimated system age range for times when the orbital parameters were also within their observed range. If this occurred we then recorded the transit radius during these times and compared the range of achieved values to observed values. In situations where a good estimate on the age is not available, we searched within 1 to 5 Gyr. When a secondary eclipse constraint on the eccentricity is not available we assume that the eccentricity value is 0.025 ± 0.025 (i.e. the likely range is between 0 and 0.05). In cases where the eccentricity is observed to be consistent with zero from a secondary eclipse, we assume that the eccentricity value is 0.005 ± 0.005 (ie. the likely range is between 0 and 0.01). We use the observed semi-major axis and error. We then search for instances of evolution histories during the possible age range that have an error-normalized distance less than 3 to the observed value. This distance is defined as

$$\sqrt{(a_i - a_m)^2/\sigma_a^2 + (e_i - e_m)^2/\sigma_e^2} \tag{2.7}$$

where a_i and e_i are the orbital parameters for the instance of a particular run and a_m, σ_a, e_m, and σ_e are the measured/assumed semi-major axis, semi-major axis sigma, eccentricity, and eccentricity sigma. Planet orbital parameters, transit radii, and stellar parameters are from F. Pont's website at http://www.inscience.ch/transits/ and The Extrasolar Planets Encyclopedia at http://exoplanet.eu/.

2.5 General Examples

Here we add different components of the model step-by-step, such that each effect can be appreciated independently. The two opposing effects of tidal evolution are late-time heating that is associated with eccentricity damping and more efficient early-time cooling due to initial semi-major axes that are larger then the present value. The four cases present are for a 1 M_J planet orbiting a 1 $M_\odot$ star at 0.05 AU. In each of these cases we assume that the planet has a 10 $M_\oplus$ core.

Case 1: no tidal effects, Figure 2.1. In the left panel, the solid line is the planet transit radius and the dot-dashed line is the radius at 1 kbar (near the convective-radiative boundary). In the right panel, the intrinsic planet luminosity is plotted as a function of time. As the planet contracts the luminosity of the planet significantly decreases. Without an internal heat source or semi-major axis evolution the planet's radius monotonically decreases with time.

Case 2: no orbital evolution, constant interior heating, in Figure 2.2. In this case the net output power is the difference between the intrinsic luminosity and a constant interior heating source of unspecified origin. In these evolution runs, the planet stops contracting when the intrinsic luminosity is equal to the constant heating source. This is equivalent to when the ratio between the input power and the luminosity of the planet is equal to unity. The upper 3 evolution tracks (purple, cyan, and blue) all reach an equilibrium between the interior heating and luminosity of the planet within 2 Gyr, but the evolution runs with lower input power do not reach an equilibrium state

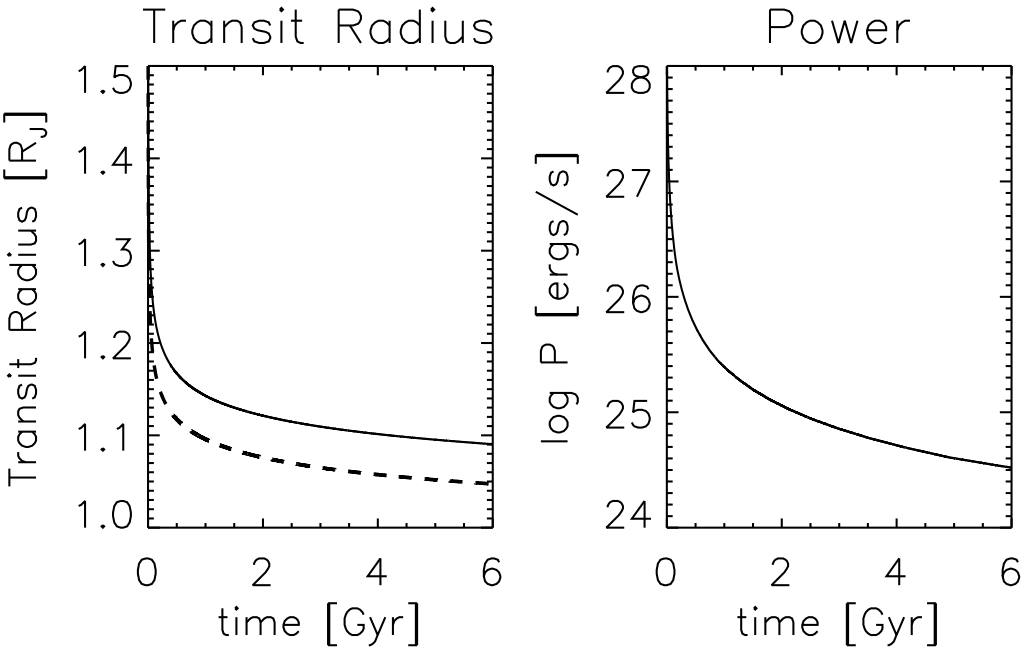

Figure 2.1: Radius and intrinsic planet luminosity evolution for a 1 M_J planet at 0.05 AU around a 1 $M_\odot$ star without any tidal effects. In the left panel, the dashed line is the radius at 1 kbar, near the convective/radiative boundary at gigayear ages. The solid line is the radius where the atmosphere reaches 1 mbar - approximately the radius that would be observed in transit.

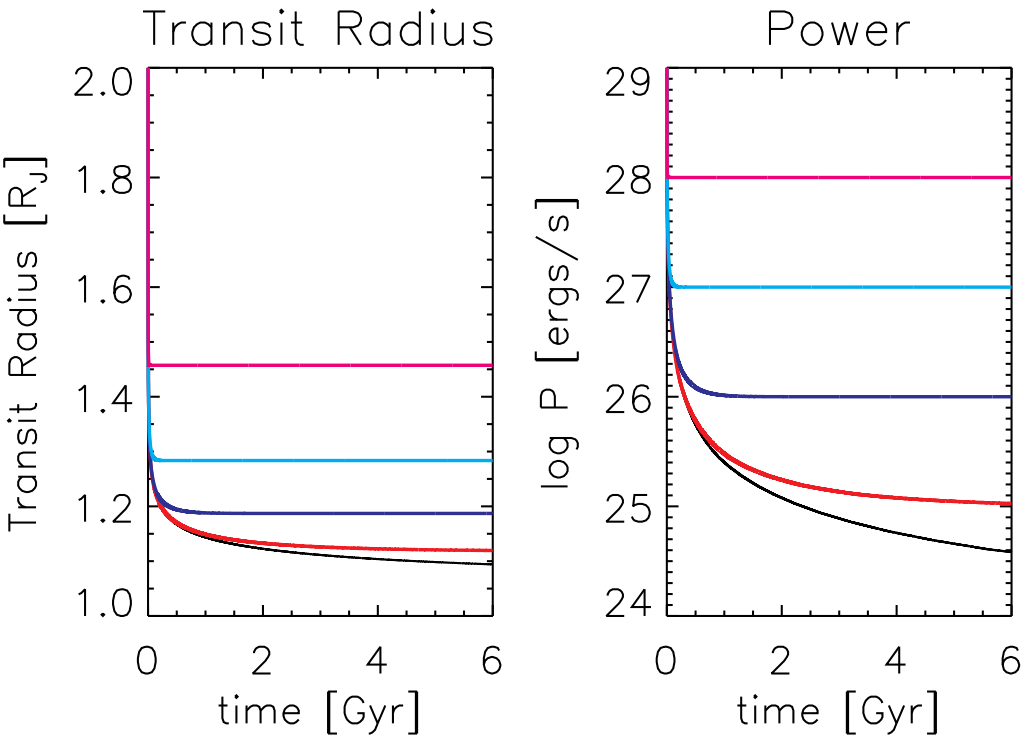

Figure 2.2: Similar to Figure 2.1, but with various constant heating applied in the interior of the planet. Moving from bottom to top, the constant heating rates are 10^{24}, 10^{25}, 10^{26}, 10^{27} and 10^{28} erg s^{-1}.

in the 6 Gyr plotted. As expected, when there is more input power, the equilibrium radius is larger. In practice, the input power through tides or other processes will not be constant over gigayears, but a planet may be inflated to a radius such that it is in a temporary equilibrium state.

Case 3: tidal orbital evolution, but without tidal heating, Figure 2.3. This case demonstrates how the orbital evolution due to tides effects the thermal evolution

of the planet. Here we plot both the $Q'_{\rm p} = 10^5$ (tidal effects on the planet occur faster) and $Q'_{\rm p} = 10^{6.5}$ (tidal effects on the planet occur slower) cases with $Q'_{\rm s} = 10^5$ in black and red respectively. These curves exactly track each other because the tides on the planet do not significantly contribute to the migration when the eccentricity is small (here $e = 0$). When comparing Figure 2.1 to Figure 2.3, notice that in the second case, the power drops off more rapidly as the semi-major axis decreases. This is due to the increase in insolation by the parent star, which deepens the atmospheric radiative zone, lessening transport of energy from the interior (e.g. Guillot et al. 1996). Another result of moving the planet closer to the star is that there is an up-tick in the transit radius. This is due only to an increase in the effective temperature, which increases the atmosphere height. The semi-major axis evolution accelerates as the planet moves inward due to the tidal migration rate's strong dependence on semi-major axis.

Case 4: tidal orbital evolution and tidal heating, Figure 2.4. We now put both the orbital evolution and corresponding tidal heating together. Black is the $Q'_{\rm p} = 10^5$ case and red is $Q'_{\rm p} = 10^{6.5}$ case. Notice that in the low $Q'_{\rm p}$ case, the planet circularizes quickly and tidal heating becomes less important. In the high $Q'_{\rm p}$ case, the planet is still undergoing circularization and significant tidal heating at late times. As a result, the radius in the high $Q'_{\rm p}$ case (slower rate of tidal effects in planet) can be larger than the low $Q'_{\rm p}$ case (faster rate of tidal effects in planet) at late times. Both trials start out with fairly modest eccentricity ($e = 0.3$).

In Figure 2.5, we compare the radius evolution in all four of these cases: Case 1 (no tidal effects, black), Case 2 (no orbital evolution, constant heating, blue), Case

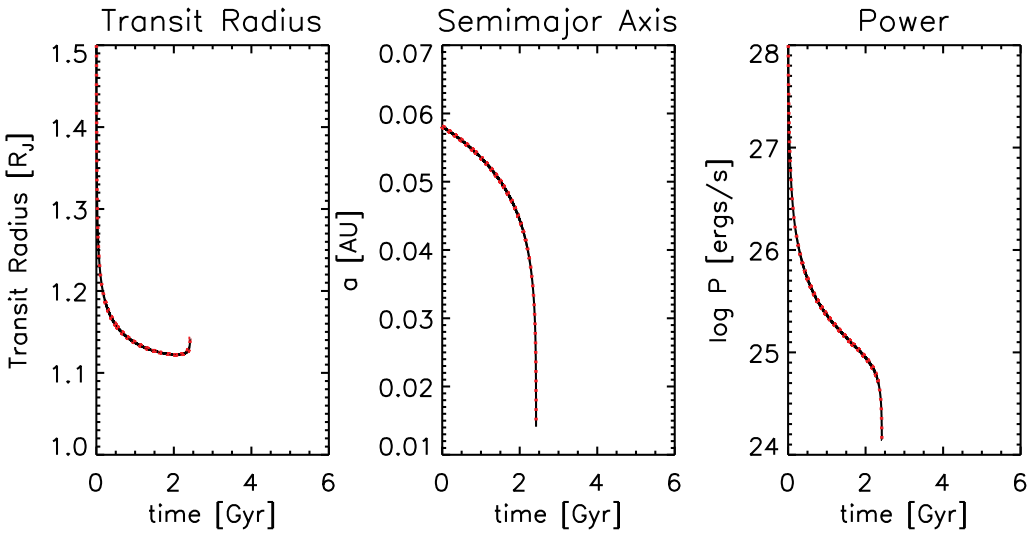

Figure 2.3: Planet thermal evolution with orbit evolution, but without tidal heating. Transit radius, semi-major axis and the planet's intrinsic luminosity are plotted from left to right. $Q'_{\rm p} = 10^5$ and $Q'_{\rm p} = 10^{6.5}$ cases are plotted in black and red respectively.

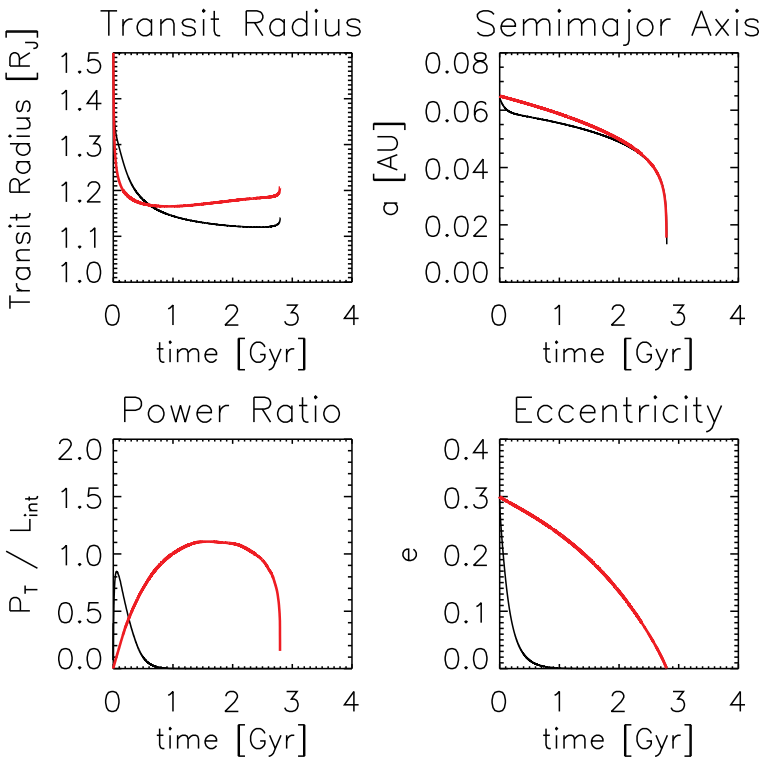

Figure 2.4: Coupled planet thermal evolution and orbital evolution. $Q'_{\rm p} = 10^5$ and $Q'_{\rm p} = 10^{6.5}$ cases both with $Q'_{\rm s} = 10^5$ are plotted in black and red respectively. We plot, the radius evolution in the upper left, semi-major axis evolution in the upper right, ratio between tidal heating and intrinsic planet luminosity in the lower left, and eccentricity in the lower right.

3 (tidal orbital evolution, but not tidal heating, red), and Case 4 (full tidal evolution model, cyan). The cases with tidal evolution are plotted for the high $Q'_{\rm p}$ case. Clearly, when tidal heating is included (cyan or blue), it can result in a radius larger than achieved without including tidal heating (red or black). Since tidal heating is a time-varying quantity, the planet's radius when tidal heating will not be as simple as in Case 2. Generally, the planet will experience significant tidal heating when the orbit is being circularized. At this time, the radius will increase, but after this time the radius of the planet will contract again. Also, because the planets in Case 3 (red) start at larger orbital distance than that of Case 1 (black), the radius contracts marginally faster when the planet is at larger semi-major axis. This is why the red line is lower than the black line before 2 Gyr. After this point, the transit radius increases in the red line case because the planet has moved close to the star, the effective temperature of the planet increases, and the atmosphere height also increases.

To examine how different levels of internal heating affect the radius of the planet, we plot the planet radius after 5 Gyr as a function of mass in Figure 2.6. Again, these models assume a 10 $M_{\oplus}$ core, at a orbital distance of 0.05 AU around a 1 Solar Mass star. In this figure, the black dotted line is the prediction of the thermal evolution model without tidal heating. The red dashed line is the base of the atmosphere at 1 kbar. Clearly, the height of the atmosphere is much larger for smaller planets due to their smaller gravities. The solid blue line is the radius relation from (Fortney et al. 2007b). The solid black lines are the radius of the planet given a constant heating rate after 5 Gyr of evolution. The pink dotted curves are constructed in the same

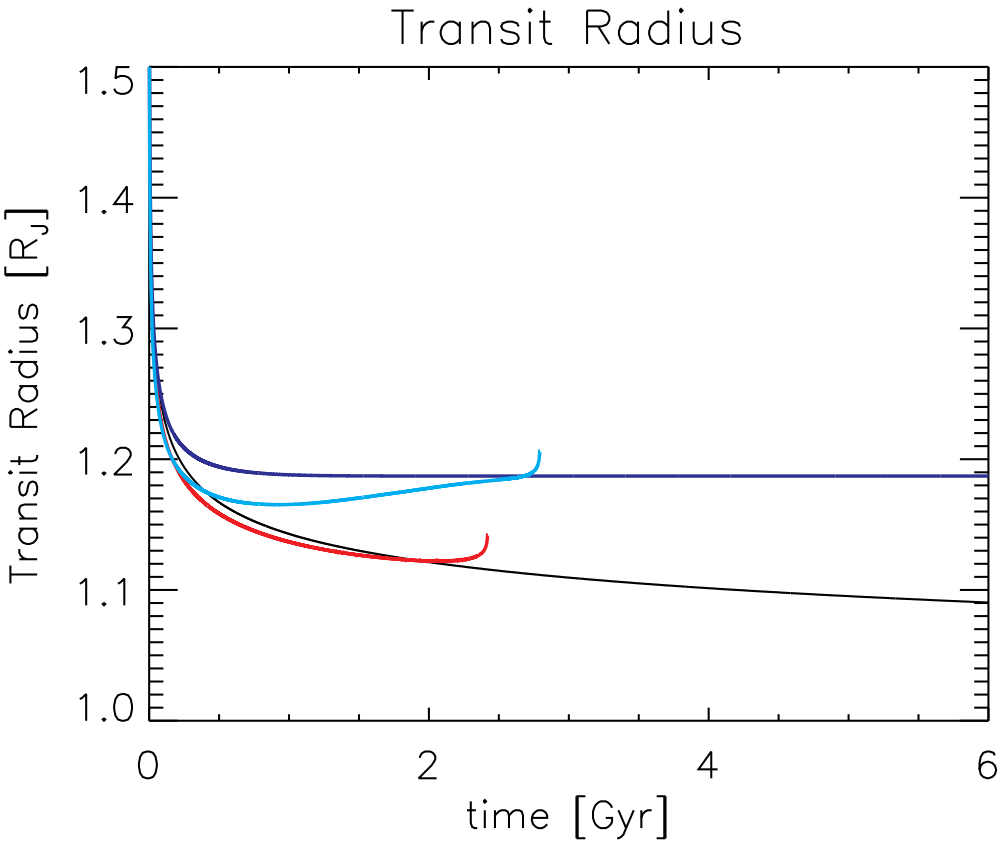

Figure 2.5: Radius evolution in different cases. Cases 1, 2, 3, 4 (see text) are plotted in black, blue, red, and cyan.

manner as the solid black curves, but required extrapolation (here, quadratic) off of the calculated atmosphere grid. At this point in time, most of these planets have reached an equilibrium state where an equal amount of internal heating is balanced by the planet's intrinsic luminosity. Clearly, the effect on the radius for a given heating is larger for smaller mass planets.

2.6 Results

2.6.1 Specific Systems

While we have computed the evolution history of 45 systems, here we show representative calculations for particular samples of planets. These are TrES-1b, XO-4b, HD 209458b, and WASP-12b, and are shown in Figures 2.7, 2.8, 2.10, and 2.11 respectively. These four cases demonstrate qualitatively different cases. TrES-1b is a circularized planet with a "normal" radius value. XO-4b, HD 209458b, and WASP-12b are large-radii planets with a small relatively unconstrained eccentricity, zero eccentricity, and a nonzero value, respectively. In Figures 2.7 - 2.11, the transit radius evolution is plotted in the upper left panel, the semi-major axis evolution is plotted in the upper right panel, the ratio between the tidal power and luminosity is plotted in the lower left panel, and the eccentricity evolution is plotted in the lower right panel. The observed semi-major axis, eccentricity, and transit radius are plotted on each of the respective panels. The power ratio, tidal power to luminosity, describes how important tidal effects are to the energy flow of the planet. When this ratio is somewhat smaller than unity,

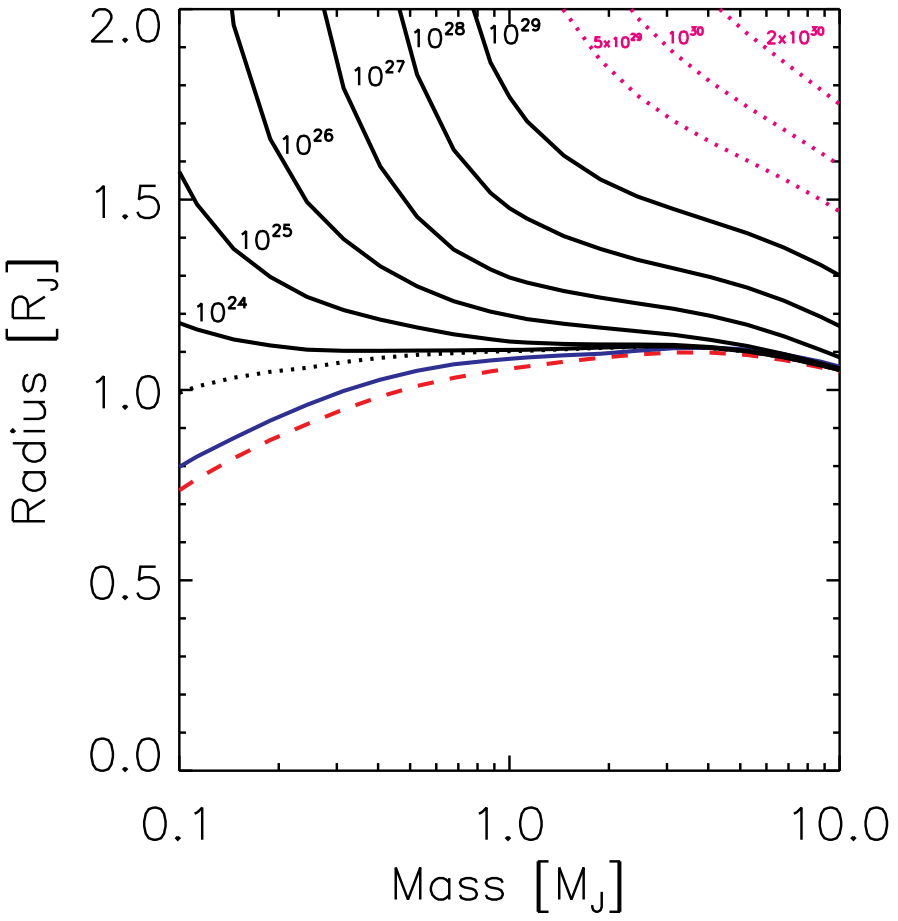

Figure 2.6: The dotted black line is the transit radius without any internal heating as a function of mass assuming a 10 $M_{\oplus}$ core. In these models, we hold the planet at 0.05 AU around a 1 Solar Mass star. The dashed red line is the 1 kbar radius—near the convective/radiative zone boundary. The blue line is the relation from Fortney 2007. The solid black lines are the radius one would find if there were a constant heating source (values between 10^{24} and 10^{29} erg s^{-1}). The pink dotted lines were calculated in the same way, but required extrapolation (quadratic) off of the grid of atmosphere models.

tidal heating is relatively un-important for the thermal evolution of the planet and when this ratio reaches or surpasses unity, tidal heating plays a more significant role in the thermal evolution. In each of these figures, a set of runs were selected such that the orbital parameters and transit radius are closest to the observed values.

TrES-1b is a transiting hot-jupiter planet with zero or small eccentricity and a typical radius observation. The system is composed of a 0.76 $M_{\rm J}$ planet orbiting a 0.89 $M_{\odot}$ star with a 0.04 AU semi-major axis. Tidal heating is not necessary to invoke to explain this system; we demonstrate that this tidal model can still explain these kinds of modest radius systems. Possible evolution histories with tidal effects are shown in Figure 2.7. These possible histories are selected such that their orbital parameters at the current age agree with the observed values and the transit radius that is close to the observed value. We show various core sizes in different colors: black for zero core, red for a 10 $M_{\oplus}$ core, and blue for a 30 $M_{\oplus}$ core. The cyan dotted line is the evolution history of a non-tidal thermal evolution model with a 10 $M_{\oplus}$ core. Notice the radius evolution of the non-tidal model doesn't differ significantly from the radius evolution of the corresponding 10 $M_{\oplus}$ (red) tidal model. In these possible evolution histories with tidal effects, the initial eccentricity is relatively small and tidal heating doesn't dominate the energy flux budget (in the lower left panel, the power ratio is always less than 1). However, the orbit decays significantly due to tides raised on the star by the planet, which continues even at $e = 0$. These tides cause these planet to migrate from an initial semi-major axis of 0.05 AU to 0.04 AU with the assumed $Q'_{\rm s} = 10^5$. Figure 2.7 demonstrates that this model easily explains the radius of TrES-1b with a core between

10 $M_\oplus$ and 30 $M_\oplus$.

There is a slight upturn in radius just before an age of 4 Gyr. This is due to the heating of the planet's atmosphere at very small semi-major axis, and is *not* due to tidal power. As the planet reaches smaller orbital distances the incident flux it intercepts increases dramatically, leading to an enlarged atmospheric extension, and greater transit radius. This feature is also present in the recent paper by Ibgui & Burrows (2009). The tracks end when we stop following the evolution, with the assumption that the planet is disrupted or collides with the parent star. This is merely the first of many evolution tracks that we present with the end state being the disruption of the planet. This finding is essentially quite similar to that of Levrard et al. (2009) who find that all of the known transiting planets, save HAT-P-2b, will eventually collide with their parent stars. Robust observational evidence for this mechanism was recently detailed by Jackson et al. (2009).

XO-4b is an inflated planet where the eccentricity has not been well constrained, due to sparse radial velocity sampling (McCullough et al. 2008). In these cases we search for instances over the evolution histories where the eccentricity is between 0 to 0.05, because we assume that a larger value would have been clearly noticed in radial velocity data. With this eccentricity constraint we show in Figure 2.8 that there is a narrow period of time when we can explain the inflated state with a recent circularization of the orbit that has deposited energy into the interior of the planet. The evolution curves shown here are for tidal parameters $Q'_{\rm p} = 10^5$ and $Q'_{\rm s} = 10^5$; in the higher $Q'_{\rm p}$ case, the radius evolution curves do not agree with the observed value.

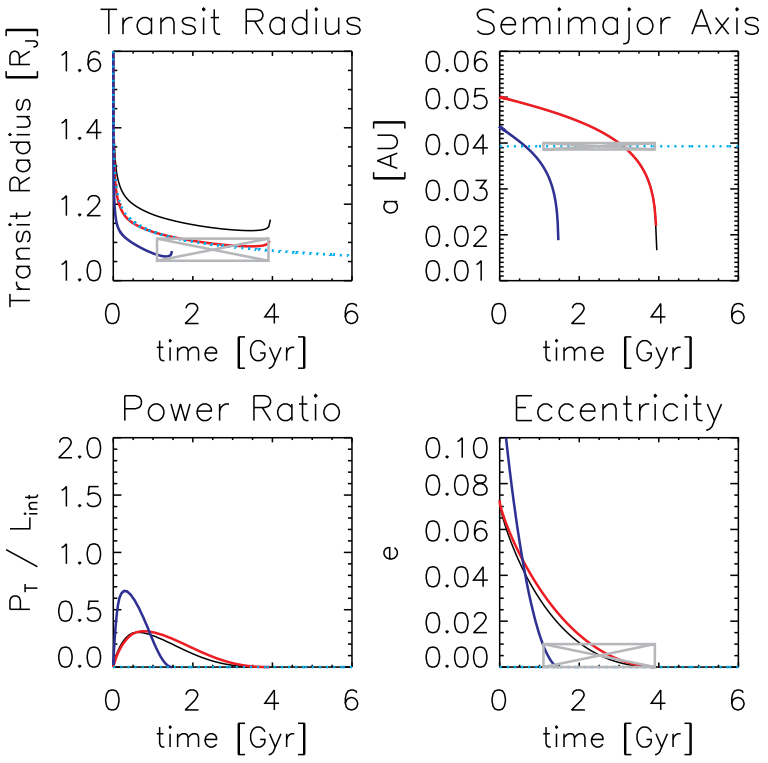

Figure 2.7: Possible tidal/thermal evolution tracks for the planet around the star TrES-1. Black: no core. Red: 10 $M_\oplus$ core. Blue: 30 $M_\oplus$ core. Cyan dotted: 10 $M_\oplus$ core evolution history without tidal effects. This is a 0.76 M_J planet orbiting a 0.89 $M_\odot$ star. Upper left panel: transit radius evolution. Upper right panel: semi-major axis evolution. Lower left panel: ratio between tidal power injected into the planet and intrinsic planet luminosity. Lower right panel: eccentricity evolution. Observed semi-major axis, eccentricity and observed radius are plotted in their respective panels. These evolution tracks were selected to have orbital parameters that agree with the observed values. $Q'_\mathrm{p} = 10^{6.5}$, $Q'_\mathrm{s} = 10^5$.

In Figure 2.8, we show black, red, and blue curves for evolution runs with no core, 10 $M_\oplus$ core, and 30 $M_\oplus$ core respectively. The pink curve is an evolution history for low initial eccentricity with a 30 $M_\oplus$ core. Again, the cyan curve is a no-tidal evolution history with 10 $M_\oplus$ core. Since tidal power is deposited mainly when the planet is being circularized, *high initial eccentricity orbits are required for these planets to experience significant later tidal inflation.* Another interesting feature of this plot, is that when comparing the radius of the runs for different cores at any given time, we find that the radius is not always monotonically decreasing with core size. This shows that uncertain past orbital-tidal history can lead to uncertainly in derived structural parameters such as the core mass.

As an example of the kind of calculation that was performed for every planet, in Figure 2.9 we show snapshots of the orbital parameters (a and e) of the ensemble of systems that are at some point consistent with the observed orbital parameters and age of XO-4b. Note that we do not require that the radius simultaneously also agree with the observed radius, but rather compare the range of possible radius values achieved by the model to the actual observed value. The black points are the original orbital parameters. The red points are the orbital parameters for one of these runs at a later point in time (0.5 Gyr, 1.5 Gyr, and 2.1 Gyr). The filled green circle marks the 1 σ observed orbital parameters, while the dashed region is the 3 σ zone.

HD 2094598b is a large-radius planet with eccentricity that has been observed to be very close to zero (Deming et al. 2005). The planet is observed to have a radius of 1.32 $R_{\rm J}$ and mass of 0.657 $M_{\rm J}$. Therefore we require evolution histories where the

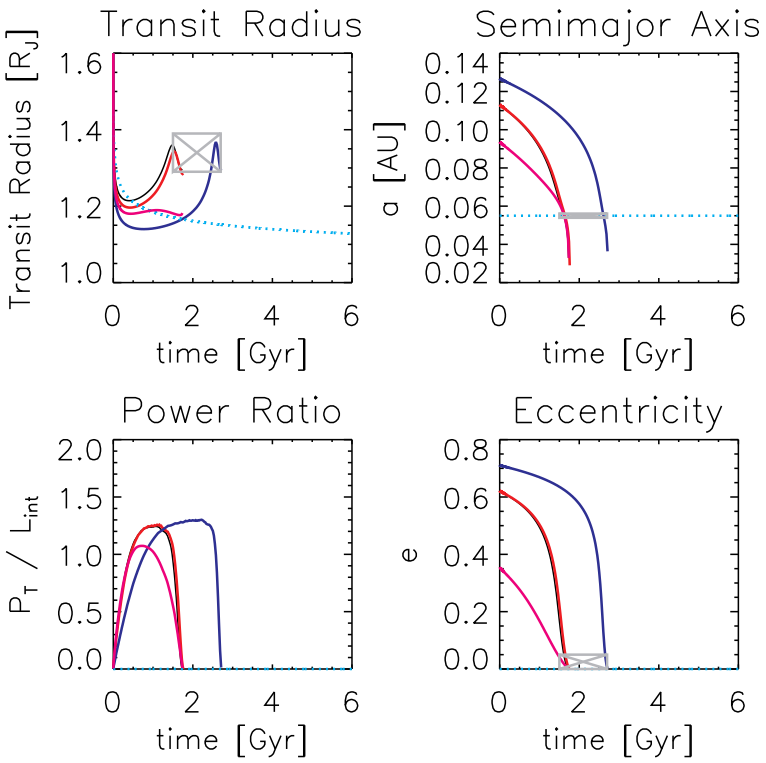

Figure 2.8: Possible tidal/thermal evolution tracks for the planet around the star XO-4. This is a 1.72 $M_{\rm J}$ planet orbiting a 1.32 $M_{\odot}$ star. Black: no core. Red: 10 $M_{\oplus}$ core. Blue: 30 $M_{\oplus}$ core. Magenta: 30 $M_{\oplus}$ core with a low initial eccentricity. Cyan dotted: 10 $M_{\oplus}$ evolution history without tidal effects. Panels are analogous to Figure 2.7. The eccentricity that is marked in the lower right panel is our assumed possible range (0 to 0.05). These evolution tracks were selected to have orbital parameters that agree with the observed values. $Q'_{\rm p} = Q'_{\rm s} = 10^5$. Notice that the tidal models initially have smaller radii than the non-tidal model because the tidal models are able to more efficiently cool at early times due to their larger semi-major axis.

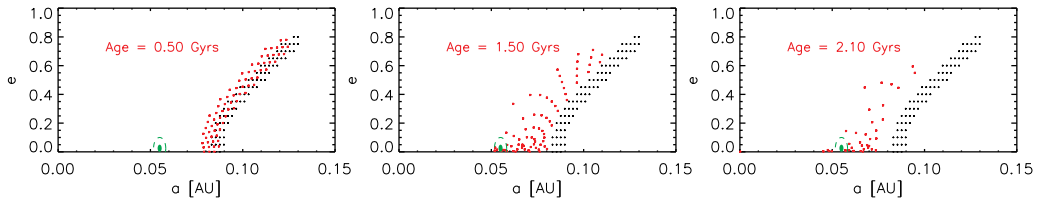

Figure 2.9: Grid of evolution histories for XO-4b that were found to be consistent with the orbital parameters at a later time. These histories are not required to also have a radius value that is consistent with the observed value. These evolution runs assume a core size of 10 $M_{\oplus}$, $Q'_{\rm p} = 10^5$, and $Q'_{\rm s} = 10^5$. This serves as a sample for the type of calculation that was performed for every planet. Black: original orbital parameters of each run. Red: orbital parameters at a later marked time (0.5 Gyr, 1.5 Gyr, and 2.1 Gyr). The filled green circle is the 1 σ zone, while the dashed region is the 3 σ zone.

current eccentricity is < 0.01. Evolution histories for this system are shown in Figure 2.10 with $Q'_{\rm p} = 10^5$ and $Q'_{\rm s} = 10^5$. With these chosen Q values, we find that the planet could have experienced tidal heating at a previous time, however by the time it has an eccentricity of 0.01 or less the planet's radius has since deflated below the observed value. It is possible to find an evolution histories that agrees with the observations by allowing different Q values, as shown by Ibgui & Burrows (2009). Although the tidal Q value is not strongly constrained and may even vary depending on the configuration of the system (Ogilvie & Lin 2004), it is our view that it makes the most sense to fix the Q value close to prior inferred values. Again, the black, red, and blue curves correspond to no core, 10 $M_\oplus$ core, and 30 $M_\oplus$ core sizes respectively. The cyan curve is a non-tidal thermal evolution history for a 10 $M_\oplus$ core. In these cases, tidal power is sufficient to inflate the planet's radius to its observed value, however we do not find evolution histories that also agrees with the other observed parameters—especially the eccentricity. In the semi-major axis evolution, there is a clear transition knee where the rate of orbital evolution decreases. The first phase is due to tidal effects of both the star and planet while the eccentricity is nonzero. The second phase is mainly due to tides on the star when the eccentricity is zero.

WASP-12b is a planet with an especially large radius of 1.79 $R_{\rm J}$ with a non-zero eccentricity of 0.05 (Hebb et al. 2009). An interesting property of this system is that the planet is filling at least 80 % of its Roche lobe by radius which is depicted in Figure 2.12 (Li et al. 2009). The solid purple surface shows the radius as implied by the transit radius. A thin atmosphere may connect this surface to the inner Lagrange

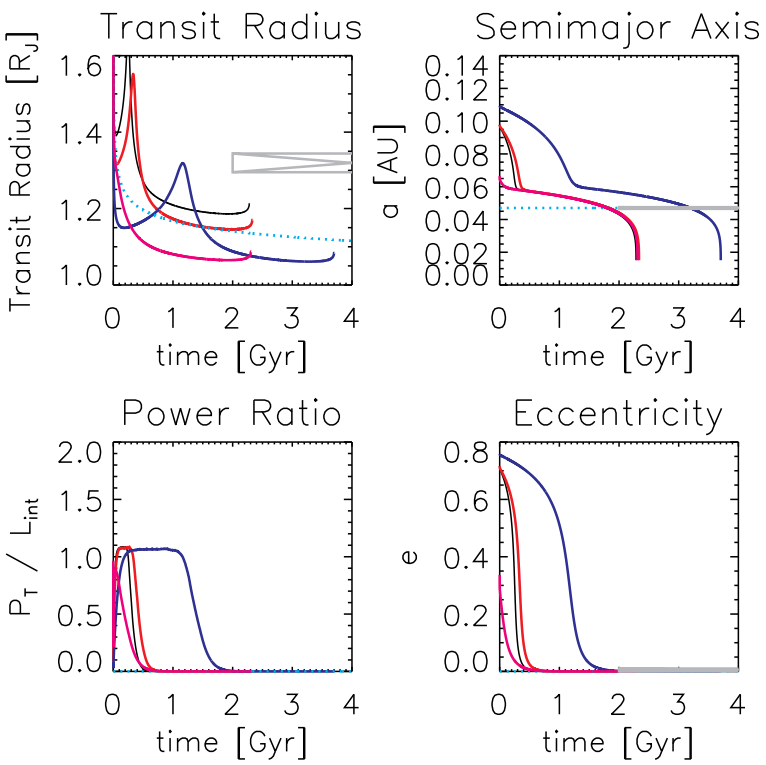

Figure 2.10: Possible tidal/thermal evolution tracks for the planet around the star HD 209458. This is a 0.657 $M_{\rm J}$ planet orbiting a 1.101 $M_{\odot}$ star. The planet has a radius of 1.32 $R_{\rm J}$ and an observed eccentricity of zero. Black: no core. Red: 10 $M_{\oplus}$ core. Blue: 30 $M_{\oplus}$ core. Purple: 30 $M_{\oplus}$ core with low initial eccentricity. Cyan dotted: 10 $M_{\oplus}$ core evolution model without tidal effects. Panels are analogous to Figure 2.7. $Q'_{\rm p} = Q'_{\rm s} = 10^5$.

point where mass may be flowing onto the star. Figure 2.11 shows evolution curves in black, red, and blue for no core, 10 $M_\oplus$ core, and 30 $M_\oplus$ core cases respectively when an eccentricity floor is imposed. Also, in cyan is the non-tidal model. In these tidal cases the tidal power increases in strength as the semi-major axis decays until the planet undergoes a rapid expansion. When the semi-major axis gets small enough, the tidal power exceeds the luminosity and the planet's radius rapidly increases. This happens both because the incident flux decreases the intrinsic luminosity of the planet and tidal heating has a strong semi-major axis dependence ($P_t \sim a^{-15/2}$). We do not model the mass loss process, which is likely to occur at late times for systems such as these (Gu et al. 2003) This should only be taken as evidence that if there was an eccentricity driving companion similar to mechanisms suggested by Mardling (2007), then it may be possible to heat this planet to quite large radii.

2.6.2 Summary for Suite

We have summarized our results for all 45 planetary systems in Figures 2.13 and 2.14 for $Q'_{\rm p}$ equal to 10^5 and $10^{6.5}$. In these figures, we have plotted the observed radius range (lower limit to upper limit) in black. The achieved radius range under various assumptions is plotted in color. Possible radii are recorded in instances of the evolution histories when the orbital parameters and age all agree with the observed a, e, and age values (as defined previously, within 3 error-normalized distance units of the observed value). The age of each system is often quite uncertain; since the possible radius values are sensitive to the age of the system, this is a large source of uncertainty

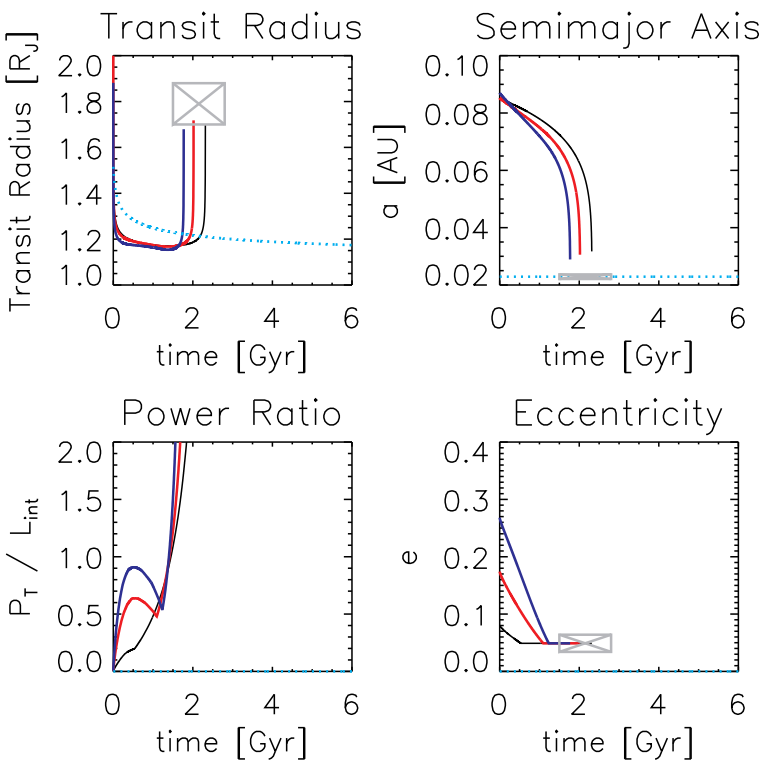

Figure 2.11: Possible tidal/thermal evolution for WASP-12b. This is a 1.41 $M_{\rm J}$ planet orbiting a 1.35 $M_{\odot}$ star. The planet has a very large observed transit radius of 1.79 $R_{\rm J}$ and an eccentricity of 0.05. In these evolution histories, we impose an eccentricity floor mimicking the effects of an eccentricity driving force. Black: no core. Red: 10 $M_{\oplus}$ core. Blue: 30 $M_{\oplus}$ core. Cyan dotted: 10 $M_{\oplus}$ core evolution history without tidal effects. Panels are analogous to Figure 2.7. $Q'_{\rm p} = 10^5$ and $Q'_{\rm s} = 10^5$.

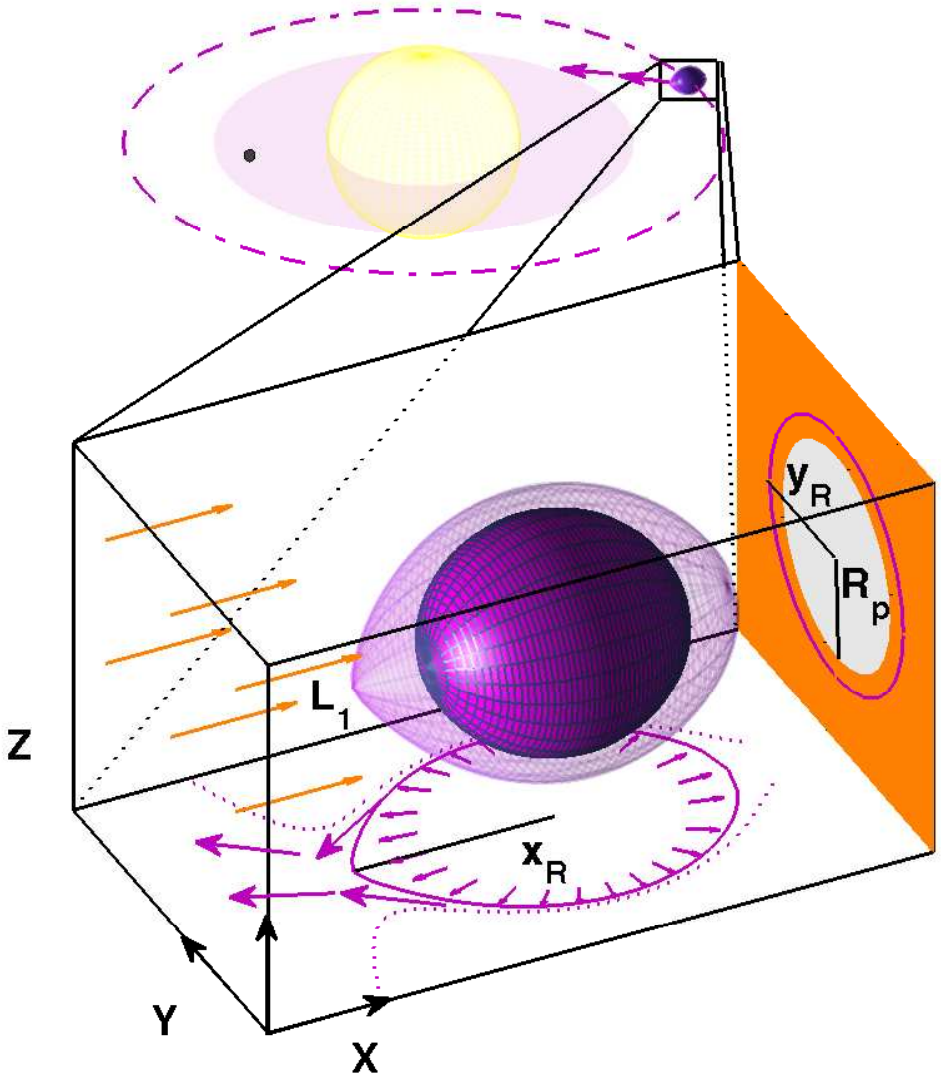

Figure 2.12: Diagram of WASP-12 b. The solid surface depicts the radius as determined from the observed radius R_p from transit observations. y_R is the distance to the Roche lobe along the plane of the planet. The planet's radius is 80% of the Roche radius. It is likely that WASP-12 b is losing mass onto its parent star through the inner Lagrange point.

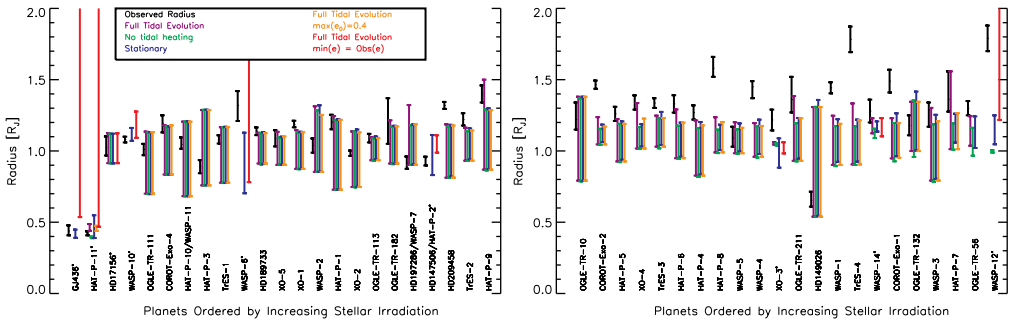

(a) (b)

Figure 2.13: Observed planet radius (black) compared to a range of achieved model radii (colors) using $Q'_{\rm p} = 10^5$; $Q'_{\rm s} = 10^5$. Planets are ordered by increasing incident flux according to their current observed parameters. Planets are marked with a * if they have nonzero observed eccentricity. The range of possible radius values under the full tidal evolution model is plotted in purple with initial eccentricity between 0 and 0.8. The radius range for a model with tidal-orbital evolution, but without the tidal heating into the interior of the planet is plotted in green. The radius range for a standard stationary model without any tidal effects is plotted in blue. The radius range for the full tidal evolution model with a maximum initial eccentricity of 0.4 is plotted in orange. In cases where a nonzero eccentricity has been observed, the radius range with an eccentricity floor equal to the observed value is shown in red.

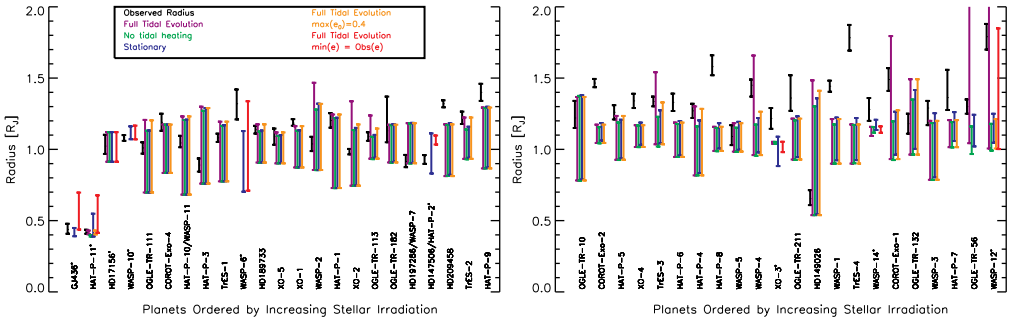

(a) (b)

Figure 2.14: Observed planet radius (black) compared to a range of viable model radii (colors) using $Q'_{\rm p} = 10^{6.5}$; $Q'_{\rm s} = 10^{5}$. Qualitatively, we observe the same trends that were observed in Figure 2.13). A larger $Q'_{\rm p}$ value decreases the rate of tidal effects via tides on the planet. Typically the tides on the planet from the star are responsible for circularizing the orbit, while tides on the star from the planet are responsible for decreasing the semi-major axis. In the larger $Q'_{\rm p}$ case, the tidal circularization can be delayed for longer, which can make the possible radius of the planet larger. On the other hand, a larger $Q'_{\rm p}$ also decreases the power deposited into the planet.

for our results. For each planet, a range of radius values is plotted for up to five different successful types of models. These are models computed as discussed in §2.5.

1. The full tidal evolution model is shown in purple. In this model the initial eccentricity was sampled from 0 to 0.8 and the initial semi-major axis was sampled from the observed semi-major axis to 5 $\times$ the observed value. This is case 4 in §2.5.

2. The model with tidal migration but without heating is shown in green. We perform the same search procedure as in the full tidal model. This model is not meant to be physical, but to give us an understanding of how tidal orbital migration alone effects the planet's radius. This is case 3 in §2.5.

3. The "stationary" model is shown in blue with all tidal effects turned off. These are "standard" cooling/contraction models, quite similar to those in Fortney et al. (2007b). These models differ slightly than the models listed in Fortney et al. (2007b) in two ways. First, these models more accurately take into account the height of the atmosphere. Second, some of these models explore a wider range of core sizes. This is case 1 in §2.5.

4. For planets whose current observed eccentricity is less than 0.4, the full tidal evolution with an maximum initial eccentricity of 0.4 is plotted in orange. Because tidal heating in the planet is directly connected to eccentricity damping, these runs serve as a demonstration of relatively less tidal heating due to circularization. This is a subset of case 4 from Section 2.5.

5. For systems where there is a measured non-zero eccentricity, we simulate the effects of an eccentricity source by performing the full tidal evolution with an eccentricity floor equal to the observed value. These cases are shown in red. This is essentially a combination of Case 4 and Case 2.

For some planets, some of these "cases" were either not possible to compute or in no instances were the observed parameters consistent with the model parameters. For instance in cases when the observed eccentricity is larger than 0.4, the tidal evolution histories with 0.4 maximum initial eccentricity never are consistent with the observation. In these cases, no radius range is drawn. In some of the cases where tidal heating is included, an evolution history is found where a large amount of energy is deposited into the planet while the orbital parameters are consistent with observations. These result in a maximum achieved radius that sometimes exceeds 2 R_J. In some of these cases, the planet will later cool off before the evolution stops. In other cases, the tidal power is sufficient to increase the planet's entropy beyond the maximum entropy of our grid, which ends the evolutionary calculation. In the future we plan to include mass loss and the subsequent evolution history.

By comparing these models we find a few interesting patterns. When comparing the full tidal evolution model (purple) to the stationary model (blue), notice that there are some cases where the full tidal model has a larger maximum radius and other cases where the reverse is true. This can be understood to be caused by the two competing effects of tidal evolution. Tidal heating puts power into the planet and inflates the radius, and tidal orbital evolution allows the planet to cool more efficiently

at earlier times when the planet is less irradiated by the parent star. It is also useful to compare these two cases to the no heating model. The no heating model generally has a smaller maximum radius than the stationary model because of the second effect. The tidal model has a larger maximum radius than the no heating model because of energy deposition into the planet.

Often the model achieves large radius values through a recent circularization of an originally high eccentricity orbit. During the circularization event (when the eccentricity drops significantly), tidal dissipation in the interior of the planet may deposit sufficient energy to significantly inflate the planet. The orange case (maximum initial eccentricity equal to 0.4) has been plotted to compare against the purple (initial eccentricity up to 0.8) to show how large initial eccentricity evolution histories contribute to the maximum achieved radius. Note that in the low $Q'_{\rm p}$ case in Figure 2.13, extremely large radii can be achieved for GJ 436b and HAT-P-11. This happens in our model through a recent rapid circularization of the orbit.

It may also be possible to have tidal heating without large initial eccentricities if there is a eccentricity driving source in the system. In some cases, such as in WASP-6b or WASP-12b, the resulting tidal heating may be enough to explain the large transit radius. By comparing the red (tidal evolution with an eccentricity floor) to the purple (regular tidal evolution), larger radius values can be achieved when the orbit is not allowed to circularize.

Tidal evolution and heating clearly have important effects on a planet's evolution, but not all of the large-radius planets could be explained through this mechanism,

given our chosen Q values. The planets HD 209458b, COROT-EXO-2b, HAT-P-9b, WASP-1b and TrES-4b have radii that are larger than achieved in our models in both the low and high $Q'_{\rm p}$ cases. Typically, while it is possible to inflate the radius to the observed values, it difficult to find the system with an inflated radius and low current eccentricity. WASP-12b was explained if we assume that its eccentricity is maintained.

When comparing Figure 2.13 to Figure 2.14, it is interesting that some of the planets that are not explainable in the lower $Q'_{\rm p}$ case can be explained with larger $Q'_{\rm p}$. Although $Q'_{\rm p} = 10^5$ results in tidal heating being stronger than the $Q'_{\rm p} = 10^{6.5}$ case, it also results in circularization on a shorter time scale. In the $Q'_{\rm p} = 10^{6.5}$ cases, it is often common for there to be a possible recent circularization of a high initial eccentricity orbit where no such history was found in the $Q'_{\rm p} = 10^5$ evolution runs.

In Table 1, we have selected a set of the largest planets and listed various properties. In the left column, we list the observed parameters. For various core sizes, we list the achieved radius of the tidal model in the low $Q'_{\rm p}$ and high $Q'_{\rm p}$ cases, the estimated luminosity of the planet at its current radius, and the current contraction rate of the planet without internal heating (previously defined as $\dot{R_{NH}}$). Also, on the top row for each planet, we list the coefficient of tidal heating. This is defined as

$$C_T \equiv \frac{P_T}{\left(\frac{e}{0.01}\right)^2 \left(\frac{10^5}{Q_{\rm P}}\right)} \tag{2.8}$$

$$= \frac{63}{4}(GM_*)^{3/2} M_* R_p^5 a^{-15/2} \times 10^{-9} \tag{2.9}$$

This quantity allows one to get an order-of-magnitude idea of recent tidal heating given the more constrained properties of the system (radius of the planet, masses of the bodies,

and semi-major axis). The actual tidal power will greatly depend on the eccentricity and Q values, which are more uncertain. The ratio between the luminosity of the planet and this coefficient of tidal heating is a dimensionless number that describes how important tidal effects can be for a given core size. Certainly, since $P_T \propto e^2$ and $Q'_{\rm p}$ is quite uncertain, this ratio is not a strong test of tidal effects, but it is a simple way of testing how important tidal effects presently can be. Notice also that for an assumed tidal power, we can compute the present contraction rate using this table and Equation 2.6.

When calculating the contraction rate, the planet is assumed to be located at the current observed semi-major axis, which determines the incident flux from the star, structure of the planet's atmosphere, and thus the intrinsic luminosity of the planet at each time. For these large-radius systems, the contraction rate is often very fast. If we assume that tidal heating is the cause of large radii, but that an eccentricity driving companion is not present, then either the system is in a transient period or that this thermal evolution model is not correct. On the other hand, if we rule out transient explanations, then either a constant heating is present or it is necessary to invoke another mechanism.

2.6.3 High $Q'_{\rm s}$ cases

Although $Q'_{\rm s}$ is generally thought to be closer to 10^5 based on the observed circularization time in binaries, it is possible that that tidal dissipation in the stars is less efficient in the planet-star case. Since tidal evolution is not fully understood, the high $Q'_{\rm s}$ case may or may not be physical. However, an advantage of this case is that

it allows for orbital history solutions with a recent circularization. In this regime, the planet migrates inward at a slower rate and thus the circularization would occur at a later time. Also, after the tidal power is deposited, the planet is not rapidly migrating into the star as in the low $Q'_{\rm s}$ cases. Ibgui & Burrows (2009) have suggested that high $Q'_{\rm s}$ case can better explain the radius of HD 209458b.

We have explored this parameter regime as shown in Table 2 for five of the systems that we were not able to explain in the low $Q'_{\rm s}$ cases. We test the cases $Q'_{\rm s}$ $= 10^6$ and $Q'_{\rm s} = 10^7$ with both $Q'_{\rm p} = 10^5$ and $Q'_{\rm p} = 10^{6.5}$. In the table the radius range is reported for a given core size, $Q'_{\rm p}$ and $Q'_{\rm s}$ model parameters, as well as the number of runs that were found at some point in time to be consistent with the observed age, semi-major axis and eccentricity of the system.

Also, in Figure 2.15, we show snapshots in semi-major axis / eccentricity space of possible evolution histories of HD 209458 b that are consistent with the observed parameters. The black points are the original orbital parameters, while the red points are the orbital parameters at a later time. The green oval is the 1 σ orbital parameters. The dashed green line is the 3 σ orbital parameters, which we require an evolution histories to fall within during the expected age range of the system. Eccentricity was sampled from 0.2 to 0.8 in this particular case.

We also show in Figure 2.16 possible radius evolution histories for the planets HD 209458b, WASP-1b, and CoRoT-Exo-2b. When $Q'_{\rm s}$ is allowed to be larger, the qualitative effect is that the planet's semi-major axis decreases slower and thus the circularization event occurs at a later time. This makes it possible to sometimes achieve

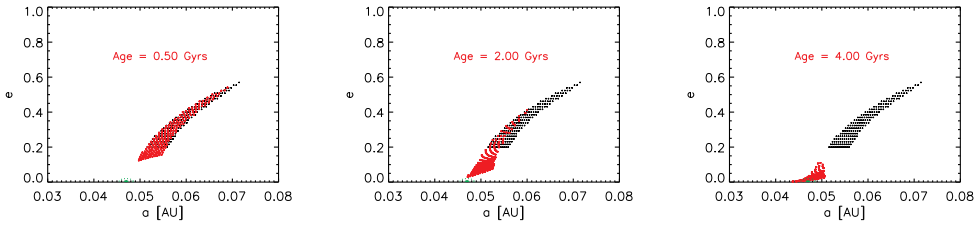

Figure 2.15: Grid of evolution histories (with initial $e > 0.2$) that were found to be consistent with the orbital parameters at a later time for the system HD 209458. These evolution runs assume there is no core, $Q'_{\rm p} = 10^{6.5}$ and $Q'_{\rm s} = 10^{6}$. Black: original orbital parameters of each run. Red: orbital parameters at a later marked time (0.5 Gyr, 1.5 Gyr, and 2.1 Gyr). The filled green circle is the 1 σ zone, while the dashed region is the 3 σ zone.

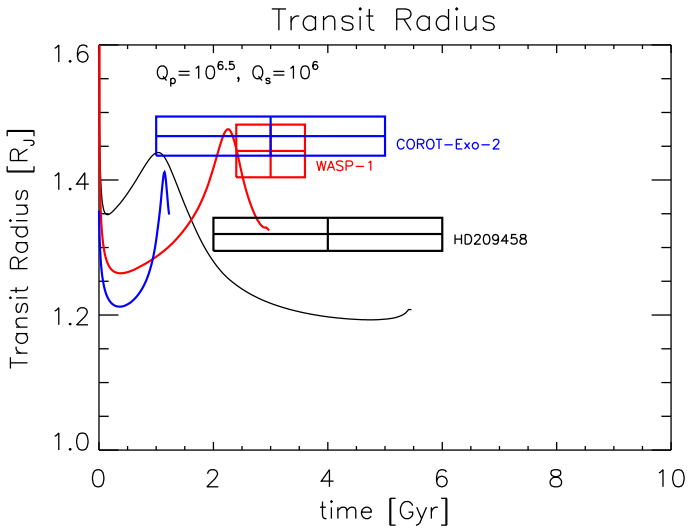

Figure 2.16: Potential radius evolution histories for HD 209458b, WASP-1b, and CoRoT-Exo-2b with no core, $Q'_{\rm p} = 10^{6.5}$ and $Q'_{\rm s} = 10^6$ (larger than our standard case). As usual, these evolution histories have been selected from an ensemble of possible initial conditions such that at some point during the estimated age of the system, the planet has orbital parameters that are consistent with the observed values.

higher radius values at the expected age of the system with the model. However, even for these high $Q'_{\rm s}$ runs for these large-radius planets, only for two of the five can the observed radius be matched.

2.7 Discussion & Conclusions

This paper presents a coupled tidal and thermal evolution model applicable to close-in extrasolar giant planets. The model is tested against 45 of the known transiting systems. Generally, tidal evolution yields two competing effects on the radii of close-in

EGPs:

1. Tidal evolution requires that, after planet formation and subsequent fast migration to a relatively close-in orbit, the planet start at a larger semi-major axis than is currently observed (Jackson et al. 2008a). This results in less incident flux at earlier times, which allows the planet to cool more efficiently and contract more at a young age, which moves the range of feasible model radii at the current time to smaller values. Generally this is a minor effect, but it is more important for cases when the current incident flux is larger.

2. Tidal evolution deposits energy into the planet when the orbit is being circularized. This typically increases the radius of the planet at this time. If there is an eccentricity driving source for the inner planet, then tidal heating can be important for the duration of the planet's life. If the planet starts with a highly eccentric orbit, it might not circularize for gigayears. The semi-major axis of the planet's orbit will initially slowly decrease due to tides on the star. As the planet moves closer to the star, tides on the planet become more effective. This delay of circularization can sometimes allow tidal heating to significantly inflate planets multiple gigayears after formation despite these systems having shorter "circularization" time scales.

We have shown that for the close-in giant planets that orbital history can play a large role in determining the thermal evolution and current observed radius. While the effects are larger for planets with larger initially eccentricities, tidal evolution still

affects the thermal evolution of planets with zero eccentricity as well. Varying amounts of time-dependent tidal heating are degenerate with the radius effects due to the core of a planet (or more generally, a heavy element enrichment).

Since at the current time we are ignorant of the exact orbital history, it is generally not possible to determine the mass of the core with complete confidence for any specific system. However, in cases when the radius of the planet is especially small, a large core or increased heavy element abundance is required. For larger radius planets, it is not possible to determine the planet's core size because recent tidal heating is degenerate with smaller core sizes. Furthermore, some systems likely have more complex orbital dynamics than described here due to the effects a third body. The uncertainty is increased since despite our expectation that tidal effects do occur, the rate that at which they occur (controlled by Q) is uncertain to an order of magnitude.

This paper serves as a *forward* test of the tidal theory for close-in EGPs outlined by Jackson et al. (2008b), who had previously only investigated heating rates *backwards* in time, from current small eccentricities from 0.001 to 0.03. Quite often however, the forward modeling of these single-planet systems, across a wide swath of initial a and e, is not consistent with current eccentricities as large as Jackson et al. (2008b) assumed. If initial eccentricities were indeed large, then final circularization and tidal surge may indeed by fairly recent, but this cannot be expected to be the rule in these systems. We have taken an agnostic view as to whether initial migration to within 0.1 AU was via scattering or disk migration. In the former, initial eccentricities up to 0.8 are possible (Chatterjee et al. 2008) while in the latter the initial eccentricity

would be zero. The viability of tidal heating to explain even some of the inflated planets with very small *current* eccentricities rests on the notion that planet scattering does occur, such that circularization (and radius inflation) can occur at gigayear ages. The detection of misalignment between the planetary orbital plane axis and stellar rotation axis via the Rossiter-McLaughlin Effect (e.g. Winn et al. 2007; 2008) is beginning to shed light on migration. Fabrycky & Winn (2009) have found tentative evidence that is consistent with two modes of migration, one which may yield close alignment (perhaps from disk migration) and one with which may yield random alignment (perhaps from scattering), although to date only XO-3b in the published literature shows a large misalignment (Hébrard et al. 2008). Further measurements will help to constrain the relative importance of these two modes of migration.

Most of the systems investigated do not require tidal heating to match their radius, but these systems can also be readily explained when including tidal evolution. Some of the planets investigated can be matched with tidal heating that could not be explained with a standard contraction model. Depending on the $Q'_{\rm p}$ value chosen, HAT-P-4, HAT-P-9, XO-4, HAT-P-6, OGLE-TR-211, WASP-4, WASP-12, TrES-3, HAT-P-7, and OGLE-TR-56 can all be explained with an evolution history with non-zero initial eccentricity. WASP-6 and WASP-12 can be explained by invoking a minimum eccentricity, which may suggest the presence of a companion. Other systems were not explained by the model for our chosen $Q'_{\rm p}$ values. This suggests that either $Q'_{\rm p}$ and $Q'_{\rm s}$ may be much different then our expectation or that other mechanisms are at work in these large-radius planets.

This work should be taken as a simplified analysis of how tidal evolution can affect a planet's thermal evolution. Strong quantitative conclusions should not be drawn because of the large uncertainties in the tidal evolution model, especially at large eccentricity. Also, the rate of tidal effects may be a very strong function of frequency. If this is the case, the planet may spend a lot of time at certain states where tidal effects are slow and rapidly pass through states where tidal effects are more rapid. If a constant Q value can even be applied, the actual value is highly uncertain. The Q values that we choose were meant only to span the range that we considered to be likely. The rate of tidal effects may depend on the interior structure of the planet and may be different for different exoplanets. Also, this analysis only takes into account orbit-circularization tidal heating.

The conclusion that should be drawn from this work is that a planet's tidal evolution history can play an important role on the planets' current radius, especially for systems that are born at semi-major axis less than 0.1 AU. In some cases, tidal heating could have inflated the radius of the planet in the recent past, even though tidal heating in the present might not be happening. In other cases, we were not able to explain the large-radius observations with our coupled tidal-thermal evolution model. This suggests that tidal heating will not be able to explain all of the large-radius planets, which has been a hope of some authors (Jackson et al. 2008b, Ibgui & Burrows 2009). For some of the planets that we are able to explain, we require a recent circularization, such that this model can only explain these observations if we at at a "special time" in its evolution. This has to be reconciled with the fraction of planets that have large radii

that require such an explanation. Improved constraints on the eccentricities of these systems will better constrain recent tidal heating.

A more robust treatment of the effects of tidal heating on transiting planet radius evolution may require a coupling of the model presented here to a scattering/disk migration model, which could derive the statistical likelihood of various initial orbital a and e configurations, which would then serve as the initial conditions to subsequent orbital-tidal and thermal evolution. This is important because for any particular planetary system the orbital evolutionary history of the close-in planet may be difficult to ascertain. Recently Nagasawa et al. (2008) have simulated the formation of hot Jupiters with a coupled scattering and tidal evolution code, and find a frequent occurence of hot Jupiter planets. A further coupled undertaking of this sort, to be compared with an statistically significant number of transiting planets, could be performed in the future.

JJF and NM are supported by NSF grant AST-0832769. We thank the referee, G. Chabrier, as well as E. Ford, D. Fabrycky, and S. Gaudi for their comments.

Table 2.1. MODEL CALCULATIONS FOR SELECTED TRANSITING SYSTEMS

System	**Core** $[M_E]$	R_p **Range**		**Power : Tidal Coefficient & Luminosity**	$\dot{R}_{NH}$
	$[M_E]$	$(Q'_{\rm p} = 10^5)$	$(Q'_{\rm p} = 10^{6.5})$	[ergs/s]	$[R_J/{\rm yr}]$
HD209458				$C_T = 6.3 \times 10^{25}$	
$M_p = 0.69\ M_J$	0.0	1.12 - 1.19	1.13 - 1.18	$L = 1.5 \times 10^{26}$	-4.2×10^{-7}
$R_p = 1.32\ R_J$	10.0	1.08 - 1.15	1.08 - 1.15	$L = 3.8 \times 10^{26}$	$-1. \times 10^{-6}$
a = 0.05 AU	30.0	1.02 - 1.08	1.02 - 1.07	$L = 1.6 \times 10^{27}$	-4.5×10^{-6}
$e = 0.00$	100.0	0.81 - 0.90	0.81 - 0.84	$L = 7.6 \times 10^{28}$	-1.5×10^{-4}
COROT-Exo-1				$C_T = 9.2 \times 10^{27}$	
$M_p = 1.03\ M_J$	0.0	1.14 - 1.23	1.16 - 1.79	$L = 1.2 \times 10^{27}$	-2.2×10^{-6}
$R_p = 1.49\ R_J$	10.0	1.11 - 1.21	1.13 - 1.79	$L = 1.8 \times 10^{27}$	-3.3×10^{-6}
a = 0.03 AU	30.0	1.07 - 1.15	1.08 - 1.52	$L = 3.8 \times 10^{27}$	-7.3×10^{-6}

Table 2.1 (cont'd)

System	**Core** $[M_E]$	R_p **Range**		**Power : Tidal Coefficient & Luminosity**	$\dot{R}_{NH}$
	$[M_E]$	$(Q'_{\rm p} = 10^5)$	$(Q'_{\rm p} = 10^{6.5})$	[ergs/s]	$[R_J/{\rm yr}]$
$e = 0.00$	100.0	0.95 - 1.03	0.93 - 1.07	$L = 5.3 \times 10^{28}$	$-1. \times 10^{-4}$
COROT-Exo-2				$C_T = 3.8 \times 10^{27}$	
$M_p = 3.31\ M_J$	0.0	1.11 - 1.23	1.11 - 1.17	$L = 6.1 \times 10^{28}$	-1.4×10^{-5}
$R_p = 1.47\ R_J$	10.0	1.11 - 1.24	1.11 - 1.16	$L = 7.0 \times 10^{28}$	-1.6×10^{-5}
a = 0.03 AU	30.0	1.09 - 1.23	1.09 - 1.15	$L = 8.7 \times 10^{28}$	$-2. \times 10^{-5}$
$e = 0.00$	100.0	1.05 - 1.20	1.05 - 1.10	$L = 1.6 \times 10^{29}$	-3.9×10^{-5}
XO-4				$C_T = 3.3 \times 10^{25}$	
$M_p = 1.72\ M_J$	0.0	1.15 - 1.34	1.15 - 1.17	$L = 1.7 \times 10^{27}$	-8.9×10^{-7}
$R_p = 1.34\ R_J$	10.0	1.14 - 1.30	1.13 - 1.15	$L = 2.4 \times 10^{27}$	-1.2×10^{-6}

Table 2.1 (cont'd)

System	**Core** $[M_E]$	R_p **Range**		**Power : Tidal Coefficient & Luminosity**	$\dot{R}_{NH}$
	$[M_E]$	$(Q'_{\rm p} = 10^5)$	$(Q'_{\rm p} = 10^{6.5})$	[ergs/s]	$[R_J/{\rm yr}]$
a = 0.06 AU	30.0	1.11 - 1.25	1.10 - 1.13	$L = 4.2 \times 10^{27}$	-2.2×10^{-6}
$e = 0.00$	100.0	1.02 - 1.11	1.02 - 1.03	$L = 3.2 \times 10^{28}$	-1.9×10^{-5}
HAT-P-6				$C_T = 4.3 \times 10^{25}$	
$M_p = 1.06\ M_J$	0.0	1.16 - 1.29	1.16 - 1.19	$L = 4.2 \times 10^{26}$	-4.7×10^{-7}
$R_p = 1.33\ R_J$	10.0	1.14 - 1.28	1.13 - 1.16	$L = 7.2 \times 10^{26}$	-8.3×10^{-7}
a = 0.05 AU	30.0	1.09 - 1.28	1.09 - 1.11	$L = 1.7 \times 10^{27}$	-2.1×10^{-6}
$e = 0.00$	100.0	0.95 - 1.09	0.95 - 0.96	$L = 3.2 \times 10^{28}$	-4.7×10^{-5}
HAT-P-7				$C_T = 8.0 \times 10^{26}$	
$M_p = 1.78\ M_J$	0.0	1.14 - 1.55	1.14 - 1.21	$L = 6.3 \times 10^{26}$	-3.2×10^{-7}

Table 2.1 (cont'd)

System	**Core** $[M_E]$	R_p **Range**		**Power : Tidal Coefficient & Luminosity**	$\dot{R}_{NH}$
	$[M_E]$	$(Q'_{\rm p} = 10^5)$	$(Q'_{\rm p} = 10^{6.5})$	[ergs/s]	$[R_J/{\rm yr}]$
$R_p = 1.36\ R_J$	10.0	1.13 - 1.56	1.12 - 1.19	$L = 8.3 \times 10^{26}$	-4.3×10^{-7}
a = 0.04 AU	30.0	1.11 - 1.50	1.10 - 1.16	$L = 1.4 \times 10^{27}$	-7.3×10^{-7}
$e = 0.00$	100.0	1.01 - 1.44	1.02 - 1.06	$L = 6.8 \times 10^{27}$	-4.2×10^{-6}
HAT-P-9				$C_T = 5.0 \times 10^{25}$	
$M_p = 0.78\ M_J$	0.0	1.16 - 1.49	1.16 - 1.29	$L = 7.0 \times 10^{26}$	-1.7×10^{-6}
$R_p = 1.40\ R_J$	10.0	1.13 - 1.50	1.13 - 1.25	$L = 1.3 \times 10^{27}$	-3.3×10^{-6}
a = 0.05 AU	30.0	1.06 - 1.36	1.06 - 1.17	$L = 3.7 \times 10^{27}$	$-1. \times 10^{-5}$
$e = 0.00$	100.0	0.87 - 1.00	0.87 - 0.95	$L = 8.6 \times 10^{28}$	-1.7×10^{-4}
TrES-4				$C_T = 3.9 \times 10^{26}$	

Table 2.1 (cont'd)

System	**Core** $[M_E]$	R_p **Range**		**Power : Tidal Coefficient & Luminosity**	$\dot{R}_{NH}$
	$[M_E]$	$(Q'_{\rm p} = 10^5)$	$(Q'_{\rm p} = 10^{6.5})$	[ergs/s]	$[R_J/{\rm yr}]$
$M_p = 0.93\ M_J$	0.0	1.15 - 1.33	1.14 - 1.17	$L = 1.0 \times 10^{28}$	-4.4×10^{-5}
$R_p = 1.78\ R_J$	10.0	1.12 - 1.32	1.11 - 1.14	$L = 1.4 \times 10^{28}$	$-6. \times 10^{-5}$
a = 0.05 AU	30.0	1.07 - 1.29	1.06 - 1.09	$L = 3.4 \times 10^{28}$	-1.2×10^{-4}
$e = 0.00$	100.0	0.91 - 0.99	0.90 - 0.92	-	-
OGLE-TR-211				$C_T = 6.4 \times 10^{25}$	
$M_p = 1.03\ M_J$	0.0	1.14 - 1.38	1.14 - 1.22	$L = 5.0 \times 10^{26}$	-6.7×10^{-7}
$R_p = 1.36\ R_J$	10.0	1.12 - 1.36	1.12 - 1.19	$L = 8.2 \times 10^{26}$	-1.1×10^{-6}
a = 0.05 AU	30.0	1.08 - 1.38	1.07 - 1.13	$L = 1.9 \times 10^{27}$	-2.7×10^{-6}
$e = 0.00$	100.0	0.93 - 1.10	0.93 - 0.97	$L = 3.6 \times 10^{28}$	-5.8×10^{-5}

Table 2.1 (cont'd)

System	**Core** $[M_E]$	R_p **Range**		**Power : Tidal Coefficient & Luminosity**	$\dot{R}_{NH}$
	$[M_E]$	$(Q'_{\rm p} = 10^5)$	$(Q'_{\rm p} = 10^{6.5})$	[ergs/s]	$[R_J/{\rm yr}]$
WASP-1				$C_T = 5.2 \times 10^{26}$	
$M_p = 0.87\ M_J$	0.0	1.16 - 1.25	1.16 - 1.21	$L = 6.1 \times 10^{26}$	-1.4×10^{-6}
$R_p = 1.44\ R_J$	10.0	1.13 - 1.22	1.13 - 1.18	$L = 1.0 \times 10^{27}$	-2.4×10^{-6}
a = 0.04 AU	30.0	1.07 - 1.18	1.07 - 1.10	$L = 2.4 \times 10^{27}$	-6.2×10^{-6}
$e = 0.00$	100.0	0.90 - 1.06	0.90 - 0.92	$L = 5.1 \times 10^{28}$	-1.2×10^{-4}
WASP-4				$C_T = 1.3 \times 10^{28}$	
$M_p = 1.27\ M_J$	0.0	1.12 - 1.20	1.13 - 1.66	$L = 3.3 \times 10^{27}$	-3.8×10^{-6}
$R_p = 1.45\ R_J$	10.0	1.11 - 1.18	1.10 - 1.51	$L = 4.6 \times 10^{27}$	-5.4×10^{-6}
a = 0.02 AU	30.0	1.07 - 1.11	1.08 - 1.52	$L = 8.2 \times 10^{27}$	$-1. \times 10^{-5}$

Table 2.1 (cont'd)

System	**Core** $[M_E]$	R_p **Range**		**Power : Tidal Coefficient & Luminosity**	$\dot{R}_{NH}$
	$[M_E]$	$(Q'_{\rm p} = 10^5)$	$(Q'_{\rm p} = 10^{6.5})$	[ergs/s]	$[R_J/{\rm yr}]$
$e = 0.00$	100.0	0.96 - 1.03	0.96 - 1.18	$L = 7.5 \times 10^{28}$	-8.7×10^{-5}
WASP-12				$C_T = 1.1 \times 10^{29}$	
$M_p = 1.41\ M_J$	0.0	-	1.18 - 2.02	$L = 2.5 \times 10^{28}$	-5.2×10^{-5}
$R_p = 1.79\ R_J$	10.0	-	1.16 - 1.57	$L = 3.6 \times 10^{28}$	$-7. \times 10^{-5}$
$a = 0.02$ AU	30.0	-	1.12 - 1.37	$L = 5.9 \times 10^{28}$	-1.1×10^{-4}
$e = 0.05$	100.0	-	1.01 - 1.11	-	-

Note. — Model results for large-radius hot Jupiters. Column 1: Observed parameters. Column 2: The assumed core mass. Column 3 & 4: The achieved radius range for two different $Q'_{\rm p}$. Column 5: Row 1: The coefficient of tidal power. Column 5: Rows 2+: The luminosity of the planet for the assumed core mass. Column 6: $\dot{R}_{NH}$, the radius derivative without an internal heating source.

Table 2.2. MODEL CALCULATIONS FOR SELECTED TRANSITING SYSTEMS

System	**Core** $[M_E]$	**Radius** $[R_J]$ (5,6)	**Radius** $[R_J]$ (5,7)	**Radius** $[R_J]$ (6.5,6)	**Radius** $[R_J]$ (6.5,7)
HD209458					
$M_p = 0.69\ M_J$	0.0	1.12 - 1.19 (683)	1.12 - 1.18 (737)	1.15 - 1.32 (816)	1.15 - 1.31 (1036)
$R_p = 1.32\ R_J$	10.0	1.09 - 1.16 (931)	1.09 - 1.15 (1136)	1.12 - 1.27 (765)	1.11 - 1.25 (945)
TrES-4					
$M_p = 0.93\ M_J$	0.0	1.16 - 1.22 (1291)	1.16 - 1.21 (849)	1.24 - 1.43 (665)	1.19 - 1.37 (1205)
$R_p = 1.78\ R_J$	10.0	1.13 - 1.19 (1285)	1.13 - 1.18 (959)	1.20 - 1.37 (512)	1.16 - 1.33 (1154)
HAT-P-8					
$M_p = 1.52\ M_J$	0.0	1.15 - 1.19 (1520)	1.15 - 1.19 (1390)	1.17 - 1.28 (538)	1.18 - 1.30 (728)
$R_p = 1.58\ R_J$	10.0	1.13 - 1.18 (1515)	1.13 - 1.18 (1390)	1.16 - 1.26 (501)	1.17 - 1.28 (694)
WASP-1					

Table 2.2 (cont'd)

System	**Core** $[M_E]$	**Radius** $[R_J]$ (5,6)	**Radius** $[R_J]$ (5,7)	**Radius** $[R_J]$ (6.5,6)	**Radius** $[R_J]$ (6.5,7)
$M_p = 0.87\ M_J$	0.0	1.17 - 1.21 (835)	1.17 - 1.20 (26)	1.23 - 1.48 (656)	1.19 - 1.39 (1463)
$R_p = 1.44\ R_J$	10.0	1.14 - 1.18 (829)	1.14 - 1.17 (297)	1.20 - 1.45 (636)	1.16 - 1.35 (1438)
COROT-Exo-2					
$M_p = 3.31\ M_J$	0.0	1.12 - 1.18 (1337)	1.12 - 1.19 (1069)	1.19 - 1.40 (1243)	1.13 - 1.33 (2127)
$R_p = 1.47\ R_J$	10.0	1.11 - 1.17 (1334)	1.11 - 1.19 (1092)	1.18 - 1.39 (1242)	1.12 - 1.32 (2120)

Note. — Achieved radius values for 5 systems with high $Q'_{\rm s}$ for core size 0.0 and 10 $M_\oplus$. The parameters used are denoted in the header with (log $Q'_{\rm p}$ log $Q'_{\rm s}$). In the body of the table, the range or achieved radius values is lested along with the number of runs found in parenthesis.

Chapter 3

Applications of Giant Planet Thermal Evolution Model

3.1 Introduction

In this chapter, I present additional interesting applications and extensions of the giant planet thermal evolution model that has been used thus far in Chapter 2. These sections are based primarily on Gillon et al. (2010), Jackson et al. (2010), and Lissauer et al. (2011). First, this chapter examines CoRoT-2b, which is a young inflated planet. In this case, tidal heating may be a good explanation for the observed radius. Second, this chapter discusses the possible energy limited mass loss history of CoRoT -7b. In this scenario, the planet may have initially been as large as 200 $M_{\rm E}$ and lost most of its mass except for a remnant core. Finally, this chapter goes on to Kepler-11, a system with six transiting planets. In this case, it is possible to learn a lot about

the composition of these planets. The primary tool is to compare model vs. predicted planet radii, depending on the assumed composition.

3.2 CoRoT-2b: Young Planet With Potentially Tidally Inflated Radius

This section is primarily based on Gillon et al. (2010) where I applied the coupled thermal-tidal evolution model.

CoRoT-2b is just one of many transiting planets with a radius larger than can be accommodated by solar composition with standard thermal evolution models. This planet has the following properties: $M_p = 3.47 \pm 0.22\ M_J$, $R_p = 1.466 \pm 0.044\ R_J$, and $e \cos \omega = -0.00291 \pm 0.00063$ where e is the orbital eccentricity and ω is the argument of periastron (Gillon et al. 2010). Constraining the age of the system to be at most a few hundreds of Myr and assuming that the non-zero orbital eccentricity is not due to a third undetected body, we model the coupled orbital-tidal evolution of the system with various tidal Q values, core sizes, and initial orbital parameters.

Given the relatively young age of the planet, compared to other known transiting planets, it is worthwhile to investigate the planet's radius evolution in some detail, as giant planets are expected to have larger radii at young ages. We use the coupled giant planet tidal and thermal evolution model of Miller et al. (2009) to calculate the planet's evolution and contraction. As in Miller et al. (2009), the planet's structure is assumed to have three components: first, a 50% rock 50% ice core, second, a fully

convective hydrogen-helium envelope with the equation of state of Saumon et al. (1995), and lastly a non-grey atmosphere model described by Fortney et al. (2007b). The tidal orbital evolution is described by Jackson et al. (2008a; 2009). This tidal evolution model assumes that the planet quickly reaches a spin-orbit synchronous state, that the only important source of tidal heating is due to orbital circularization, and the model is second order in eccentricity.

In order to determine if tidal heating can explain the large radius of CoRoT-2b, for a variety of tidal quality factors Q'_p, Q'_s, and core masses, a grid over initial semi-major axis and eccentricity is evolved forward in time. For each of these evolution histories, we searched for instances in which the semi-major axis, eccentricity, and radius are simultaneously within their observed error ranges. We choose to limit the age to between 20 Myrs and 400 Myrs. We find that in cases when the Q'_p value is too high (Q'_p of 10^6 or $10^{6.5}$) there is not sufficient dissipation inside the planet to achieve the observed radius. However, for the cases of $Q'_s = 10^5 - 10^6$ and $Q'_p \leq 10^{5.5}$ all of the observed parameters can be explained as a transient event. Evolution histories that agree closely with the observed parameters are shown in Figure 3.1. The planet radius that would be observed at optical wavelengths during the transit is shown in the upper left. The semi-major axis of the orbit is shown in the upper right. The ratio of input tidal power to net radiated power is shown in the lower left. The eccentricity is shown in the lower right. (See Miller et al. (2009) for further details.) In each panel, the runs correspond to models with no core (black), 10 $M_\oplus$ core (red), 30 $M_\oplus$ core (blue). A "standard" run without tidal effects with a 10 $M_\oplus$ core is in dotted cyan. The model

without tidal heating clearly cannot explain the planet's large radius, even given the young system age. This analysis suggests that if the Q'_p value is $10^{5.5}$ or smaller, then it is possible to explain this large radius as a transient event at the last stage of orbital circularization. Under this scenario, the planet is spiraling inwards at high speed to its final tidal disruption, and the fast rotation of the star would be due not only to its young age but also to the high rate of angular momentum transfer from the planet's orbit. With such values for Q'_s and Q_p, the future lifetime of CoRoT-2b is 20 Myr at most, which is a short duration on an astronomical time-scale but is still much larger than the remaining lifetime of the planet WASP-18b (Hellier et al. 2009) under similar assumptions.

In some planetary systems, an outer companion might continuously drive the eccentricity of the inner planet offsetting circularization by tides such that the eccentricity is found in a semi-equilibrium state, described by Mardling (2007). Let us assume this scenario is occurring and the planet's net radiated luminosity, L_p, at the surface is balanced by tidal heating inside, P_t. Using Table 1 from Miller et al. (2009)

$$\begin{aligned} L_p &= 7 \times 10^{28} \text{ ergs/sec} \\ &= P_t = \left\langle 4 \times 10^{27} \left(\frac{e}{0.01}\right)^2 \left(\frac{10^5}{Q'_p}\right) \right\rangle \end{aligned} \tag{3.1}$$

and assuming that the observed eccentricity of 0.0142 is close to its equilibrium value, then this would imply that $Q'_p \sim 10^4$. This is lower than the oft-quoted value for Jupiter between 10^5 and 10^6 (Goldreich & Soter 1966).

In summary, we find that a young age alone cannot explain the large radius of

CoRoT-2b, but that plausible tidal heating evolutionary histories, with $Q'_p \sim 10^4 - 10^{5.5}$, can explain it.

3.3 CoRoT-7b: Potential Evaporative Mass Loss Scenario

This section again utilizes the thermal-tidal giant planet evolution models and is based on the work of Jackson et al. (2010). In this case, we also include the effect of energy-limited evaporative mass loss due to XUV flux.

CoRoT-7 b is the first confirmed rocky exoplanet (Léger et al. 2009), but, with an orbital semi-major axis of 0.0172 AU, its origins may be unlike any rocky planet in our Solar System. In this study, we consider the roles of tidal evolution and evaporative mass loss in CoRoT-7 b's history, which together may have modified the planet's mass and orbit. If CoRoT-7 b has always been a rocky body, evaporation may have driven off almost half its original mass (Valencia et al. 2010), but the mass loss may depend sensitively on the extent of tidal decay of its orbit. As tides caused CoRoT-7 b's orbit to decay, they brought the planet in closer to its host star, thereby enhancing the mass loss rate. Such a large amount of mass loss also suggests the possibility that CoRoT-7 b began as a gas giant planet and had its original atmosphere completely evaporated. In this case, we find that CoRoT-7 b's original mass probably didn't exceed 200 Earth masses (about 2/3 of a Jupiter mass). Tides raised on the host star by the planet may have significantly reduced the orbital semi-major axis, perhaps causing the planet to migrate through mean-motion resonances with the other planet in the system, CoRoT-7

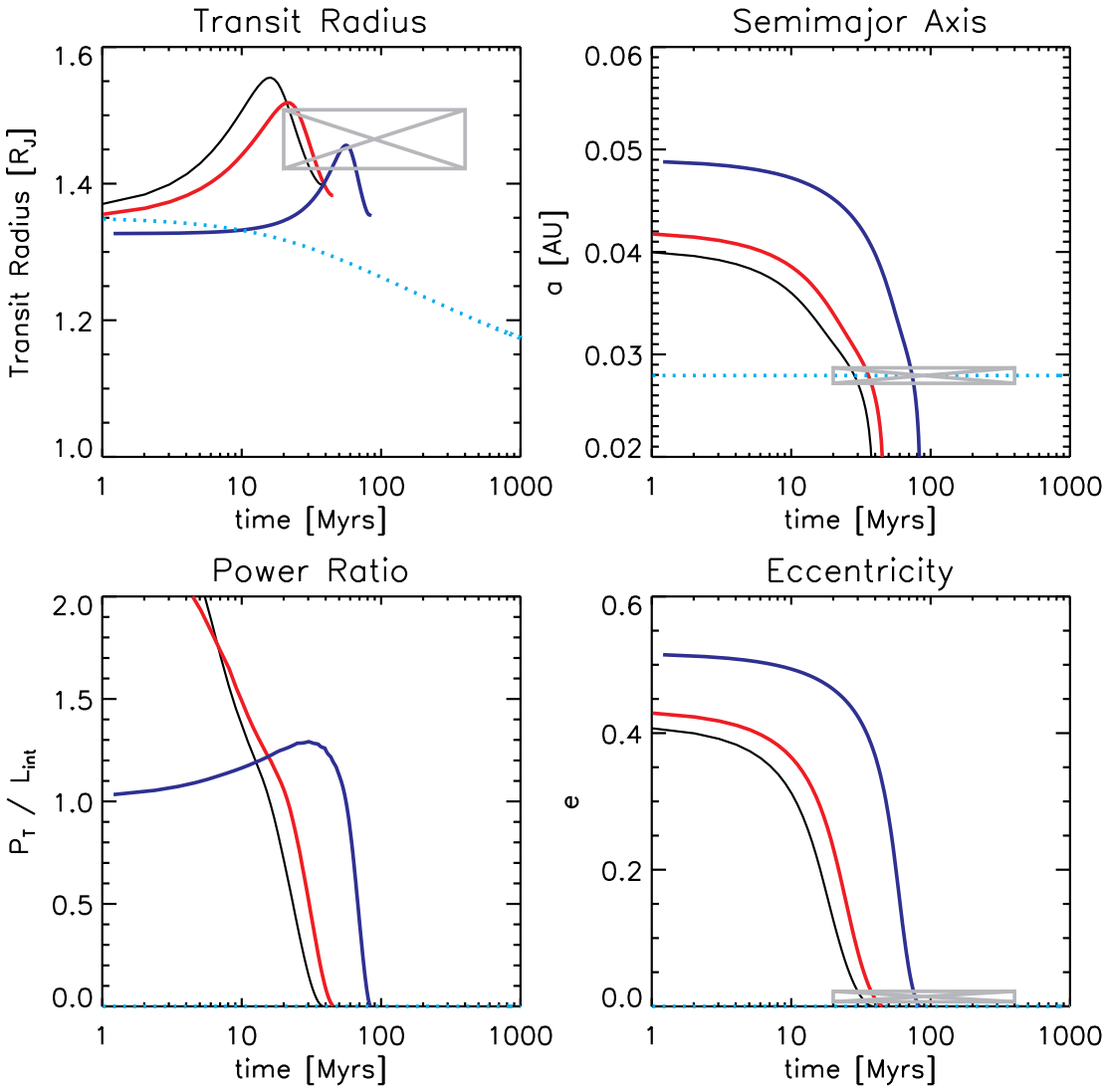

Figure 3.1: Possible tidal evolution histories for CoRoT-2. In these cases: $Q'_p = 10^{5.5}$ and $Q'_s = 10^5$. For these curves we assume that the planet has no core (black), 10 $M_\oplus$ core (red) and 30 $M_\oplus$ core (blue). The cyan run assumes that the planet has a 10 $M_\oplus$ core with no tidal evolution. See text for discussion

c. The coupling between tidal evolution and mass loss may be important not only for CoRoT-7 b but also for other close-in exoplanets, and future studies of mass loss and orbital evolution may provide insight into the origin and fate of close-in planets, both rocky and gaseous.

3.3.1 Evaporative Mass Loss Model

For energy-limited evaporative mass loss, the rate at which escaping gas molecules carry away energy from the planet is roughly proportional to the rate of input of energy from stellar insolation (Yelle et al. 2008). Relating the rate of energy input from insolation to the change in gravitational energy required for a gas molecule to escape yields estimates of mass loss rates. We take the mass loss rate to be (Erkaev et al. 2007):

$$\frac{dM_p}{dt} = -\frac{\pi R_p^3 \epsilon F_{xuv}}{G M_p K_{tide}} \tag{3.2}$$

where F_{xuv} is the extreme UV (XUV) flux from the star (wavelengths from 0.1 to 100 nm), evaluated at the planet's orbital distance (Ribas et al. 2005). R_p is the planet's radius, and G is the gravitational constant. This equation assumes that the planet's optical cross-section in the XUV is πR_p^2. ϵ represents the fraction of the incoming energy that is carried away by the escaping gas and is between 0.1 to 0.6 (Yelle et al. 2008, Lammer et al. 2009).

K_{tide} is given by:

$$K_{tide} = 1 - \frac{3}{2\xi} + \frac{1}{2\xi^3} \tag{3.3}$$

where ξ is the ratio of the Roche radius ($= (M_p/3M_*)^{1/3}a$) to R_p.

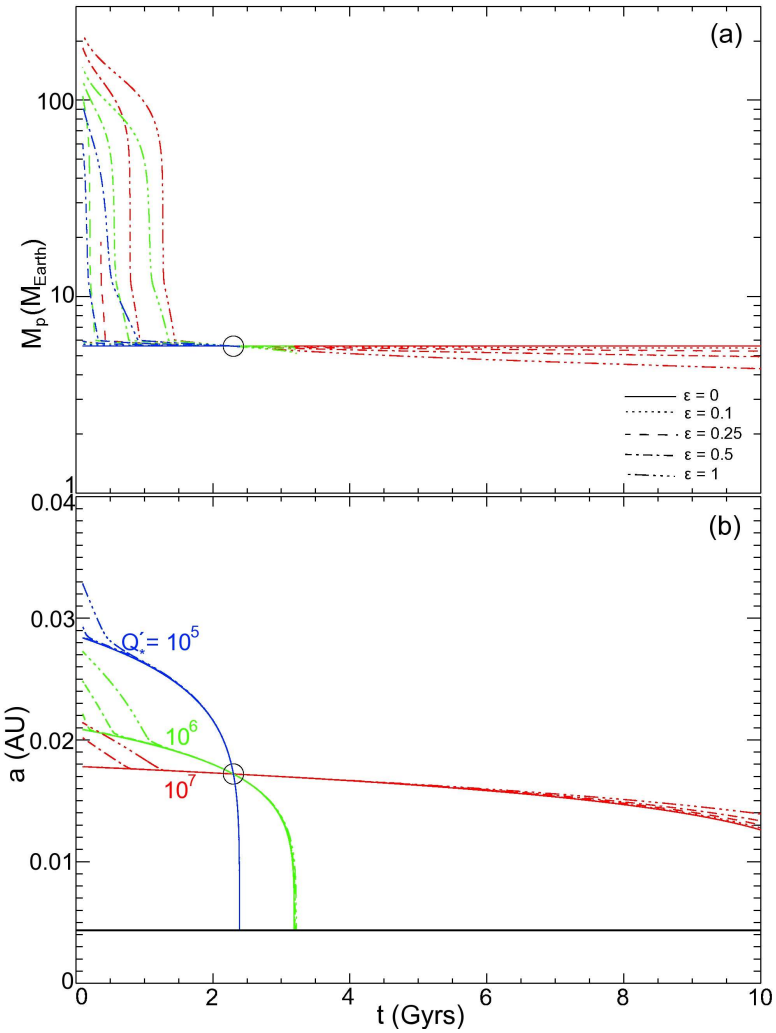

Figure 3.2: Evolution of M_p and a for CoRoT-7 b, including orbital migration. The empty circle in panel (a) represents an assumed current mass $M_{p,cur} = 5.6\ M_{Earth}$, and in panel (b), an assumed current semi-major axis $a_{cur} = 0.0172$ AU, both for a current age of 2.3 Gyr. We've assumed the rock mass fraction of the planet remains constant at 0.719. The different line colors correspond to different assumed values of Q'_*, as labeled. The solid black line represents the stellar surface.

3.3.2 Planet Evolution

This rocky exoplanet, CoRoT-7 b, could be the remnant core of a gas giant where most of the envelope was lost. In Figure 3.2, I plot mass and semi-major axis evolution including tidal evolution and the evaporative mass loss as described above. While explaining the observed orbital parameters, mass, and radius, this object may be explained via an extreme mass loss history. These models show that the initial mass may have been as large as 200 $M_{\rm E}$. Given the proximity to the star, tidal evolution may still be an important process affecting the planet's orbit.

3.4 Kepler 11

This section is based on Lissauer et al. (2011).

Kepler-11 is a single Sun-like star with six transiting planets, five with orbital periods between 10 and 47 days plus a sixth one with a longer period. The five inner planets are among the smallest whose masses and sizes have both been measured, and these measurements imply substantial envelopes of light gases. The degree of coplanarity and proximity of the planetary orbits imply energy dissipation near the end of planet formation.

3.4.1 Formation and Compositions of Kepler 11 Planets

By observing properties of multiple planets in the same system, we can attempt to get a more coherent picture of its formation and evolution. The planetary radii are

obtained from transit depths and planetary masses from dynamical interactions together give the mean density and therefore yield insight into planetary composition. Figure 3.3 plots radius as a function of mass for the five newly-discovered planets whose masses have been measured. Compared to Earth, each of these planets is large for its mass. Most of the volume in each of the planets Kepler-11c-f is occupied by low-density material. It is often useful to think of three classes of planetary materials, from relatively high to low density: rocks/metals, ices dominated by H_2O, CH_4, and NH_3, and H/He gas. All of these components could have been accumulated directly from the protoplanetary disk during planet formation. Hydrogen and steam envelopes can also be the product of chemical reactions and out-gassing of rocky planets, but only up to 6% and 20% by mass, respectively. In the Kepler-11 system, the largest planets with measured masses, planets d and e, must contain large volumes of H, as must low-mass planet f. Planets Kepler-11b and c could either be rich in ices (likely in the steam state, as in Uranus and Neptune) and/or a H/He mixture. In terms of mass, all five of these planets must be primarily composed of elements heavier than helium. Future atmospheric characterization to decipher between H-dominated or steam atmospheres would tell us more about the planets bulk composition and atmospheric stability. Planets Kepler-11b and c have the largest bulk densities and would need the smallest mass fraction of hydrogen to fit their radii. Using an energy-limited escape model, we estimate a hydrogen mass loss rate of several 10^9 g/s for each of the five inner planets, leading to the loss of ~ 0.1 $M_{\rm E}$ of hydrogen over the next 10 Gyr. This is less than a factor of 10 away from total atmosphere loss for several of the planets. The modeling of hydrogen escape for strongly

irradiated exoplanets is not yet well constrained by observations, so larger escape rates are possible. This suggests the scenario that planets Kepler-11b and c had larger H-dominated atmospheres in the past and lost these atmospheres during an earlier era when the planets had larger radii, lower bulk density, and a more active primary star, which would all favor higher mass loss rates. The comparative planetary science allowed by the planets in Kepler-11 system may allow for advances in understanding these mass loss processes.

These thermal evolution and mass loss models have been able to contribute in several additional studies. In Lopez et al. (2012), we use these models coupled to extreme ultraviolet driven mass loss to study the composition and history of Kepler-11 and the population of low-mass, low-density transiting planets. In Fortney et al. (2011), the models were used to understand the magnitude of interior power inflating the radius of Kepler-12b. In Cochran et al. (2011), the thermal evolution model was used to constrain the composition of Kepler-18 planets. This method is described in more detail in the next chapter.

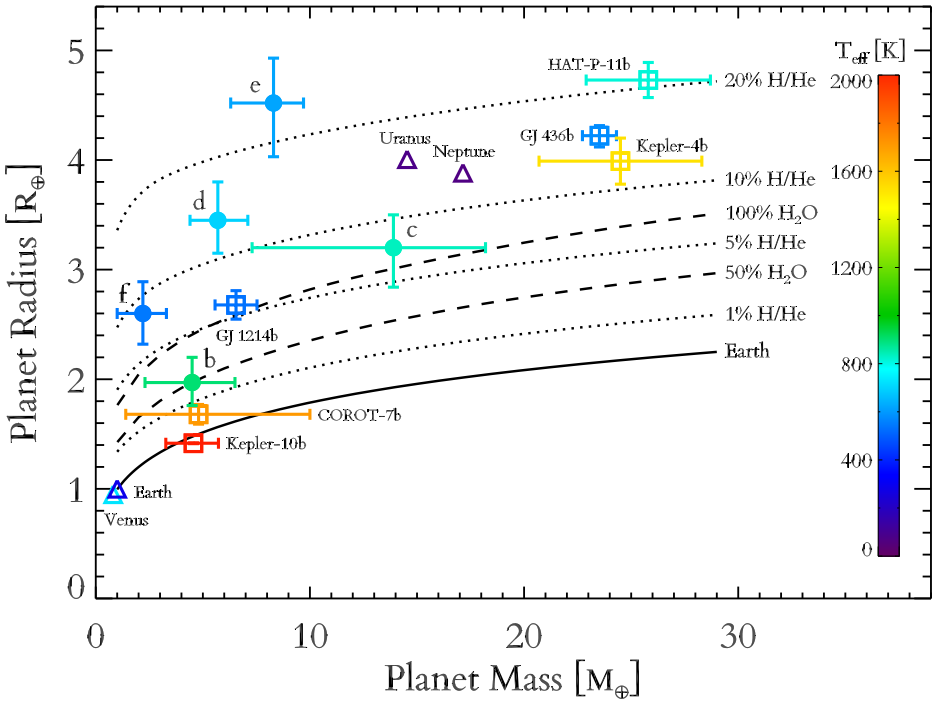

Figure 3.3: Mass-radius relationship of small transiting planets, with Solar System planets shown for comparison. Planets Kepler-11b-f are represented by filled circles with 1 σ error bars, with letters written above; values and ranges are as given in Table 1. Other transiting extrasolar planets in this size range are shown as open squares, representing in order of ascending radius Kepler-10b, CoRoT-7b, GJ 1214b, Kepler-4b, GJ 436b, and HAT-P- 11b. The triangles (labeled V, E, U and N) correspond to Venus, Earth, Neptune and Uranus, respectively. The colors of the points show planetary temperatures (measured for planets in our Solar System, computed mean planet-wide equilibrium temperatures for Bond albedo = 0.2 for the extrasolar planets), with values shown in the color bar at the right. Mass-radius curves for 8 Gyr-old planets, assuming Teff = 700 K are overplotted.

Chapter 4

Measuring the Heavy Element Composition of Giant Exoplanets with Lower Irradiation

4.1 Abstract

We investigate a population of transiting planets that receive relatively modest stellar insolation, indicating equilibrium temperatures < 1000 K, and for which the heating mechanism that inflates hot Jupiters does not appear to be significantly active. We use structural evolution models to infer the amount of heavy elements within each of these planets. There is a correlation between the stellar metallicity and the mass of heavy elements in its transiting planet(s). It appears that all giant planets posses a minimum of $\sim$ 10-15 Earth masses of heavy elements, with planets around metal-rich stars having larger heavy element masses. There is also an inverse relationship between

the mass of the planet and the metal enrichment ($Z_{\rm pl}/Z_{star}$), which appears to have little dependency on the metallicity of the star. Saturn- and Jupiter-like enrichments above solar composition are a hallmark of all the gas giants in the sample, even planets of several Jupiter masses. These relationships provides an important constraint on planet formation, and suggests large amounts of heavy elements within planetary H/He envelopes. We suggest that the observed correlation can soon also be applied to inflated planets, such that the interior heavy element abundance of these planets could be estimated, yielding better constraints no their interior energy sources. We point to future directions for planetary population synthesis models and suggest future correlations. This appears to be the first evidence that extrasolar giant planets, as a class, are enhanced in heavy elements.

4.2 Introduction

Transiting exoplanets are valuable for planetary characterization because they allow us to measure their masses through stellar radial velocity or other dynamical measurements, as well as their radii from the transit light curve. Together, these yield a planet's bulk density. In principle, this information could be used to determine a planet's composition as increasing the mass fraction of heavy elements increases the density. This apparently straightforward method has been difficult to implement, however. Transit observations have revealed that most of the highly irradiated "hot Jupiters" are inflated to large radii beyond what is expected from simple models. The reason for this effect

has not been determined; a variety of additional internal energy sources or contraction-stalling mechanisms have been proposed (Guillot & Showman 2002, Jackson et al. 2009, Batygin et al. 2011, Chabrier & Baraffe 2007, Arras & Socrates 2010). Since an inflated radius decreases a planet's density, the heating mechanism acts in opposition to the effect of adding heavy elements to the planet. Therefore interior composition for a transiting planet is generally left entirely unknown, unless planets are found to be dramatically overdense (e.g. Sato et al. 2005, Fortney et al. 2006, Leconte et al. 2009).

For the over-inflated planets it is possible to find a relation between the heavy elements in the planets and the metallicity of the stars by making an *assumption* about the relationship between the incident stellar radiation and the unknown power input into the planet (Guillot et al. 2006). A similar relationship has been found by using *ad hoc* enhanced atmospheric opacity to slow planetary contraction (Burrows et al. 2007). These studies are intriguing, although the resulting planet-star metallicity relationship is dependent on the assumed behavior of the unknown radius inflation mechanism. Since it is well-known that our solar system's four giant planets possess at least $10 - 15\ M_{\oplus}$ of heavy elements within their interiors, making them enriched compared to the Sun's composition (Fortney & Nettelmann 2010), it is paramount to determine the composition of giant exoplanets to understand the structure and formation of these planets as a class of astrophysical objects.

Empirically, the unknown heating mechanism affects the close-in planets at high incident stellar flux (Kovács et al. 2010a) or planet $T_{\rm eff}$ (Laughlin et al. 2011). This is shown in Figure 1, where we plot the observed planet radii as a function of their

average incident stellar flux. A thermal evolution model for a 1 Jupiter-mass (1 $M_{\rm J}$) planet with no extra heating source other than the effect of incident radiation on the planet's atmosphere is plotted with a heavy element core (25 Earth masses, $M_{\oplus}$, dotted) and without (solid) (Miller et al. 2009). At approximately $\langle F \rangle = 2 \times 10^8$ erg s^{-1} cm^{-2}, the sample is divided into two regions [1]: those in the higher flux region, most of which require extra heating to explain their radii, and those in the lower flux region, in which no inflated planets are found. This empirically suggests that the heating mechanism does not significantly contribute to the energy budget at low incident flux. Therefore, for this sample of 14 transiting exoplanets, we can neglect the heating mechanism and use our structural evolution models to estimate a planet's composition.

4.3 Model and Method

We consider two limiting types of planetary structures. We consider planets where all of the heavy elements are in an inert core with an adiabatic solar metallicity convective envelope above (layered model). We also consider a structure where heavy elements are uniformly mixed with the hydrogen and helium and the planet is fully convective (mixed model). The primary heavy element composition is a mixture of 50% rock and 50% ice using the equation of state ANEOS (Thompson 1990). By considering the two extreme cases of having all of the heavy element masses in the core or envelope, we bracket possible interior models of giant planets. For Jupiter, models that match

[1] $\langle F \rangle = 2 \times 10^8$ erg s^{-1} cm^{-2} corresponds to an equilibrium temperature of 990 K for an Bond albedo of 0.1 and efficient heat transport between the day and night side. This temperature is quite similar to that for which Ohmic heating is suggested to become important (Batygin et al. 2011)

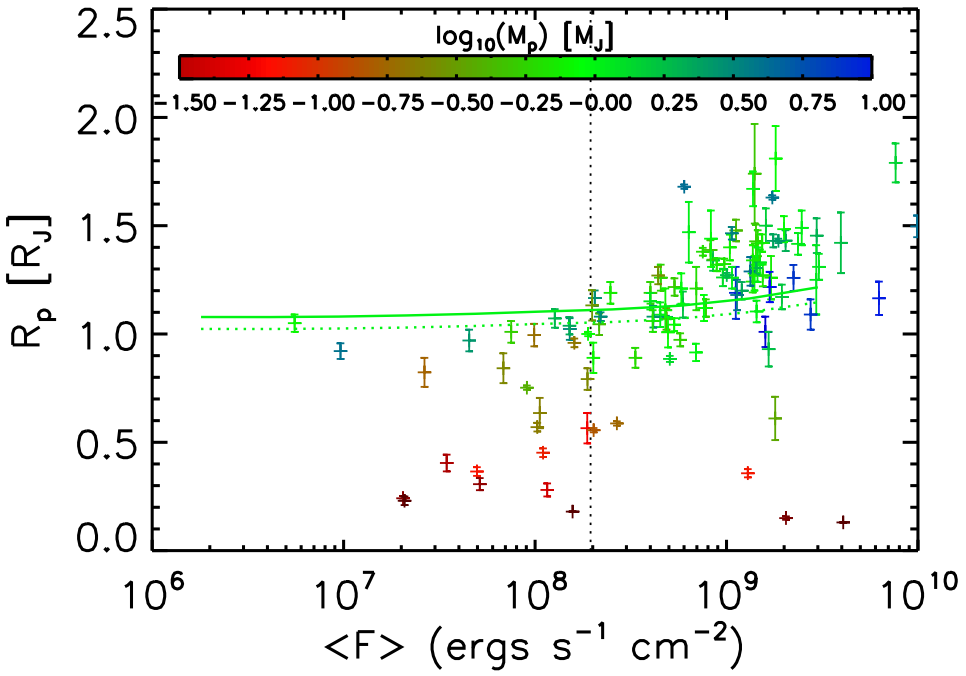

Figure 4.1: Planet radius as a function of average incident stellar flux. Planets are colored according to their mass. Model planet radii are plotted for a 1 $M_{\rm J}$ planet at 4.5 Gyr without a core (solid) and with a 25 $M_{\oplus}$ core (dotted) (Fortney, Marley, and Barnes, 2007, Miller Fortney and Jackson, 2009) Although the extra heating source is not well-determined, it is clear that it is more important at larger incident fluxes. We choose a cutoff of $\langle F \rangle < 2 \times 10^8$ erg s^{-1} cm^{-2} in order to obtain the largest sample of non-inflated planets. This corresponds to a planetary $T_{\rm eq} \lesssim 1000$ K.

gravity field constraints generally find that most of its heavy elements are in the envelope while for Saturn most are in the core (Fortney & Nettelmann 2010).

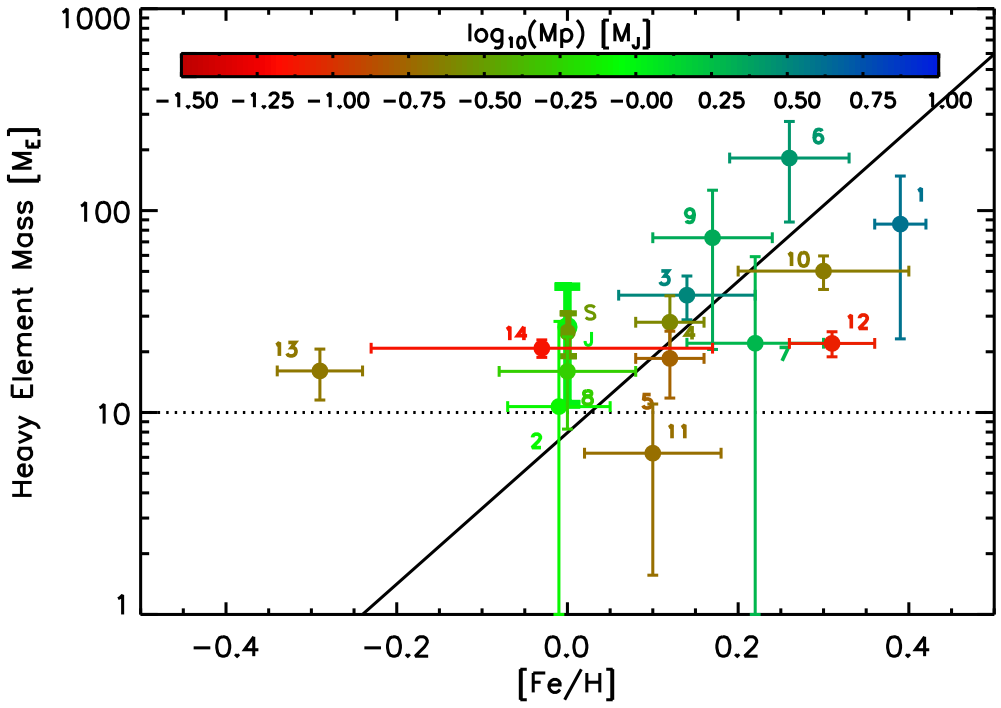

Figure 4.2: The stellar metallicity and inferred planet heavy element mass for exoplanets within our incident flux cut. The required heavy elements are from the "Average Case" in Table 1. (See text.) Planets are numbered corresponding to the entries in Table 1. The rarity of gas giants around metal-poor stars is well established (Fischer 2005). Using a least-squares fit, we find the relation $\log M_Z = (0.82 \pm 0.08) + (3.40 \pm 0.39)[\mathrm{Fe/H}]$ and a reduced Chi-squared value of 1.95. The fit excludes HAT-P-12b (planet 13) and includes Jupiter and Saturn. However, we do not expect this relation to hold at the lowest metallicities, where it may become flat at $\sim$ 10-15 $M_\oplus$.

A complete description of the thermal evolution model can be found in Fortney et al. (2007a) and Miller et al. (2009). Briefly, planets are composed of up to three components: 1) an inert core, 2) an adiabatic convective envelope (where heavy elements may be mixed in), and 3) a solar-metallicity non-grey atmosphere model (Fortney et al. 2007a) that includes the atmospheric extension to the transit radius. The primary effect of heavy elements either in the core or in the convective envelope is mainly to decrease the planet's radius at every time.

For each planet, the amount of heavy elements is determined under the constraint that the predicted model transit radius agrees with the observed radius at the observed age and incident flux. The average incident flux that a planet receives is given by

$$\langle F \rangle = \frac{L_*}{4\pi a^2 \sqrt{1-e^2}} \tag{4.1}$$

where L_* is the luminosity of the star, a is the semi-major axis of the orbit and e is the eccentricity of the orbit. This analysis was performed on all planets that met our average incident flux cut $\langle F \rangle < 2 \times 10^8$ erg s^{-2} cm^{-2} and had a mass greater than 20 $M_\oplus$–since our model is primarily designed to describe giants with masses greater than Neptune.

Note these heavy element masses should be taken as *minimum masses* since if the planet is internally heated or if higher atmospheric opacities (due to metal-enhanced atmospheres) slow the cooling (Ikoma et al. 2006, Burrows et al. 2007), then a planet would have more heavy elements than found here.

The required heavy element mass to fit the radius is determined as the average

of the layered and mixed cases. Each of the the observed system parameters (R_p, age, a, M_p) has an associated error on its published value. The propagated error on the heavy element mass (σ_H) is given by:

$$\begin{aligned}\sigma_H^2 &= \left|\frac{\partial M_c}{\partial R_p}\right|^2 \sigma_{R_p}^2 + \left|\frac{\partial M_c}{\partial \mathrm{Age}}\right|^2 \sigma_{\mathrm{Age}}^2 + \left|\frac{\partial M_c}{\partial a}\right|^2 \sigma_a^2 \\ &\quad + \left|\frac{\partial M_c}{\partial M_p}\right|^2 \sigma_{M_p}^2 + \left(\frac{M_c - M_{\mathrm{env}}}{2}\right)^2 \end{aligned} \tag{4.2}$$

where σ_{R_p}, σ_{Age}, σ_a, and σ_{M_p} are the observationally determined errors in planet radius, system age, semi-major axis, and planet mass respectively. The derivatives $\frac{\partial M_c}{\partial X}$ (calculated at the observed planet parameters assuming core heavy elements) describe the sensitivity of the predicted heavy element mass with respect to changes in a given parameter, X. The final term of the expression is the uncertainty due to the unknown structure of the planet. M_c and M_{env} are the predicted heavy element masses if the heavy elements are within the core, or the envelope, respectively.

We use the metallicity of the star [Fe/H] as given in each paper in Table 1. For each system, we compute the heavy element mass fraction $Z_{\mathrm{star}} \equiv 0.0142 \times 10^{[Fe/H]}$ - assuming that the total heavy element composition of other systems scales with their iron abundance, normalized to the solar metalicity as in Asplund et al. (2009).

4.4 Findings

In Figure 2 we plot the stellar metallicity, [Fe/H], against the planet heavy element mass for each of these systems. Using a least squares fit, we find that $\log M_Z = (0.82 \pm 0.08) + (3.40 \pm 0.39)[\mathrm{Fe/H}]$ for stars with $[\mathrm{Fe/H}] > -0.05$. The reduced Chi-

squared value of 1.95 implies that not all of the scatter can be explained by observational error. We expect a fairly flat relation (the dotted line in Figure 2) at subsolar stellar metallicity if 10-15 $M_{\oplus}$ of heavy elements are needed to trigger planet formation. In Table 1 we list the planets and observed parameters used. For each planet, we list the average predicted heavy elements between the core model and mixed model with the 50-50 rock-ice composition.

We have examined the sensitivity of our findings to alternate choices for the heavy element EOS, and the differences are small. On the low density EOS end, we have used 100% water (Thompson 1990), and on the high density end 2/3 rock (Thompson 1990) and 1/3 iron (Lyon & Johnson 1992). These generally lead to $Z_{\rm pl}/Z_{\rm star}$ that are 10-20% larger, for the water EOS, and 10-20% smaller, for the rock/iron EOS, than those found in the last column of Table 1. For example, for the HAT-P-17b average case, the best-fit heavy element mass of 16.0 ± 7.7 $M_{\oplus}$ increases to 17.7 ± 4.8 $M_{\oplus}$ for pure water, and 14.1 ± 3.9 $M_{\oplus}$ for rock/iron. This yields $Z_{\rm pl}/Z_{\rm star}$ values of 7.4 ± 2.5 and 5.9 ± 2.0 for the water and rock/iron cases, respectively, very similar to the 6.7 ± 3.5 value in Table 1.

Perhaps the clearest way of looking at this sample is to compare the planet mass against the inferred heavy element mass or heavy element enrichment ($Z_{\rm pl}/Z_{star}$), as shown in Figure 3. The mass of heavy elements appears to increase with planet mass. On the other hand, the heavy element *enrichment* decreases with increasing planet mass consistent with the pattern found in the solar system's four giant planets (Fortney & Nettelmann 2010). All of these planets are consistent with being enriched in heavy

elements and many of these must be enriched significantly.

Within the cluster of Saturn-like planets around 0.2 M_J, the most heavy element-rich planet (10, CoRoT-8b) orbits the most metal-rich parent star. For the planets more massive than Jupiter, the planets harbor large amounts of heavy elements, and orbit around metal-rich stars, which explains some of the steep slope from Figure 2. It is interesting to note that the relationship of $Z_{\rm pl}/Z_{\rm star}$ as a function of planet mass, appears fairly independent of stellar [Fe/H].

4.5 Discussion

The lower-irradiation planets are important for a better understanding of giant planet structure and formation since they allow us to probe the composition independent of major assumptions. By studying the relationship between stellar metallicity, planet mass, and heavy element mass within a planet, we will be able to test predictions of any planet formation theory, and specifically against predictions from population synthesis models such as Ida & Lin (2010), Mordasini et al. (2009), Thommes et al. (2008). These models are now being extended beyond just planet mass vs. period, to explore the relationship between [Fe/H] and planet heavy element mass (Mordasini et al. 2009).

The core accretion formation mechanism requires that heavy elements form a core of around $\sim 10\ M_\oplus$, which is followed by the accretion of gas from the protoplanetary disk (Pollack et al. 1996). Some models for Jupiter indicate that most of its heavy elements are in its envelope, not in its core (Fortney & Nettelmann 2010). Alternatively,

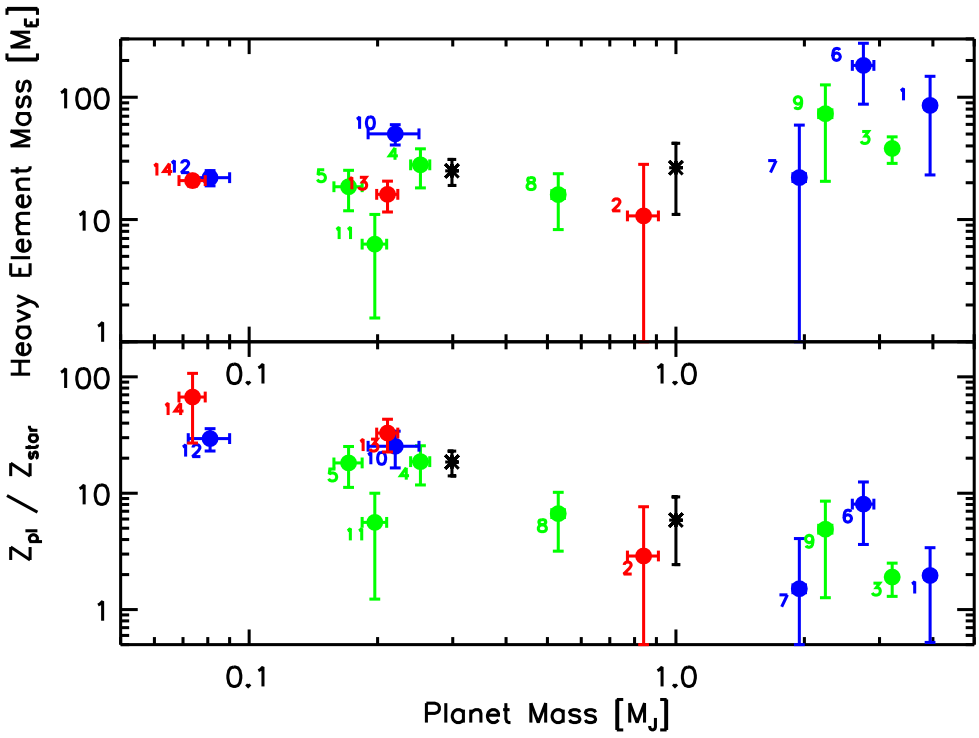

Figure 4.3: Top: The planet mass and heavy element mass for our sample. Planets are colored by metallicity in three bins: [Fe/H] < 0.0 (red), $0 \leq$ [Fe/H] < 0.2 (green), and [Fe/H] ≥ 0.2 (blue). Jupiter and Saturn are also shown in black (Guillot 1999). This plot is consistent with a minimum heavy element mass of 10-15 $M_{\oplus}$, with increasing heavy element masses for larger mass planets. Bottom: The planet mass and heavy element enrichment ratio $Z_{\rm pl}/Z_{\rm star}$. Lower mass planets are more metal enriched, but have less total heavy elements, which is consistent with the solar system's giants (Fortney and Nettelmann 2010)

gravitational instability could result in enhanced metallicity through planetesimal accretion (Guillot & Gladman 2000, Helled et al. 2006, Helled & Schubert 2009, Helled et al. 2010, Boley & Durisen 2010, Nayakshin 2010). The planets in our population, even the more massive planets, are consistent with being enhanced in heavy elements relative to their parent star. This enrichment in heavy elements is a distinguishing characteristic between planets and low mass brown dwarfs with more solar-like abundances (Chabrier et al. 2007, Leconte et al. 2009).

If this emerging relationship between stellar metallicity and planetary heavy elements continues to hold with additional data, then the relationship could be used to determine the amount of heavy elements in a given *inflated* hot Jupiter with some confidence, based only on the parent star metallicity and planet mass. This would be powerful as it would allow for a straightforward determination of the additional energy needed to explain a planet's inflated radius. The additional energy source could then be derived for each inflated planet, as a function of planet mass and irradiation level, and could be compared to model predictions (Guillot & Showman 2002, Batygin et al. 2011).

As additional data accumulate, modifications to the relations presented here could be in order. Perhaps a spread in $Z_{\rm pl}/Z_{\rm star}$ could be due to orbital period, which could tie into the planet's dynamical environment (Guillot & Gladman 2000). These relationships may be interesting to analyze in systems with multiple transiting planets. Another aspect related to orbital evolution is possible: Perhaps differences in heavy elements could be seen between planets that are well-aligned or mis-aligned with their

stellar spin axis, as measured by the Rossiter-McLaughlin Effect (Gaudi & Winn 2007), as these planets may have taken different paths to their current orbits. The relationship to stellar mass could also be investigated.

The planet formation process and composition may also be a function of the types of heavy elements that are in a protoplanetary disk. Previously, Robinson et al. (2006) showed empirically that [Si/Fe] or [Ni/Fe] are correlated with the existence of planets for a fixed [Fe/H]. Theoretically, they also showed that ice-rich disks tend to form cores faster. Therefore, as the sample of cooler planets in this domain increases, it will also be interesting to test how these planet composition trends are a function of $[\alpha/H]$ or on [Si/H], [O/H] or [C/H]. It may be possible to constrain the composition of the planetary heavy elements from such studies.

In closing, we find evidence from a sample of 14 transiting giant planets that these planets, as a class, are enhanced in heavy elements. The large heavy element abundances found indicate that all heavy elements cannot be found solely in a core. If the solar system and planet formation models are a guide, then, in addition to their dense cores, the H/He envelopes of these planets will be enhanced in heavy elements as well, which can be tested by observations of the atmospheres of planets via transit or direct imaging spectroscopy (see, e.g. Marley et al. 2007).

The trends identified here, that independent of stellar metallicity, all giant planets have a heavy element mass of 10 $M_{\oplus}$ or larger, that the abundance of heavy elements in giant planets increases steeply with stellar metallicity, that Jupiter-like enhancement over solar abundances are standard for gas giants, and that more massive

planets tend to have lower enrichment, could be enhanced or refuted by additional detections of transiting planets with equilibrium temperatures less than 1000 K. These longer-period systems will continue to be detected from the ground and recently NASA's *Kepler* spacecraft identified dozens of candidates for a potentially dramatically larger sample of these less-irradiated transiting giant planets (Borucki et al. 2011).

We thank Mark Marley, Kevin Schlaufman, James Guillochon, Philip Nutzman, and Eliza Kempton for providing feedback and encouragement. JJF acknowledges the support of NSF grant AST-1010017 and an Alfred P. Sloan Research Fellowship.

Table 4.1: Table of Planets with low incident flux

Number	Name	Mass	Radius	Age	$\langle F \rangle$	Core mass	References
1	hd80606b	3.940± 0.110	1.030± 0.036	$7.0\pm^{4.0}_{4.0}$	1.67 $\times 10^7$	87.0± 62.6	(Hidas et al. 2010)
2	corot9b	0.840± 0.070	1.050± 0.040	$4.0\pm^{5.0}_{3.0}$	6.58 $\times 10^6$	11.1± 17.6	(Deeg et al. 2010)
3	hd17156b	3.212± 0.007	1.087± 0.006	$3.4\pm^{0.6}_{0.4}$	1.96 $\times 10^8$	38.4± 9.3	(Nutzman et al. 2010)
4	kepler9b	0.252± 0.013	0.842± 0.069	$3.0\pm^{1.0}_{1.0}$	8.11 $\times 10^7$	31.0± 9.4	(Holman et al. 2010)
5	kepler9c	0.171± 0.013	0.823± 0.067	$3.0\pm^{1.0}_{1.0}$	3.14 $\times 10^7$	20.6± 6.4	(Holman et al. 2010)
6	corot10b	2.750± 0.160	0.970± 0.070	$2.0\pm^{1.0}_{1.0}$	5.38 $\times 10^7$	192.0± 93.8	(Bonomo et al. 2010)
7	hatp15	1.946± 0.066	1.072± 0.043	$6.8\pm^{2.2}_{1.8}$	1.51 $\times 10^8$	22.6± 37.1	(Kovács et al. 2010b)
8	hatp17	0.530± 0.018	1.010± 0.029	$7.8\pm^{2.2}_{2.8}$	8.91 $\times 10^7$	16.9± 7.7	(Howard et al. 2010)
9	wasp8b	2.240± 0.080	1.038± 0.047	$4.0\pm^{1.0}_{1.0}$	1.79 $\times 10^8$	76.6± 52.8	(Queloz et al. 2010)
10	corot8b	0.220± 0.030	0.570± 0.020	$3.0\pm^{1.0}_{2.0}$	1.22 $\times 10^8$	55.2± 8.1	(Bordé et al. 2010)
11	hatp18b	0.197± 0.013	0.995± 0.052	$12.4\pm^{4.4}_{6.4}$	1.18 $\times 10^8$	6.8± 4.7	(Hartman et al. 2010)
12	hatp11b	0.081± 0.009	0.422± 0.014	$6.5\pm^{5.9}_{4.1}$	1.31 $\times 10^8$	23.5± 2.7	(Bakos et al. 2010)
13	hatp12b	0.211± 0.012	0.959± 0.030	$2.5\pm^{2.0}_{2.0}$	1.90 $\times 10^8$	17.7± 4.2	(Hartman et al. 2009)
14	gj436b	0.074± 0.005	0.377± 0.009	$6.0\pm^{4.0}_{5.0}$	4.03 $\times 10^7$	22.1± 1.6	(Torres et al. 2008)

Chapter 5

Using MESA for Planet Thermal Evolution

5.1 Introduction

Giant planets are generally assumed to be fully convective and therefore homogeneous. The simplest way to relax the homogeneous assumption is by breaking up the planet into a small number of discrete layers with different materials. This is especially applicable for Neptune class planets where heavy elements make up a significant fraction of the planet's mass. Alternatively, a continuous composition gradient can be enforced from prior assumptions, but this only allows for the description of how the composition affects the energy transport. It is desirable to understand energy transport and composition gradients from a coupled perspective as the convective transport processes influence the composition profile.

There are multiple applications of interest that require an inhomogeneous giant planet thermal evolution model.

- It would be of interest to model thermal evolution of exo-Jupiter and exo-Neptune objects with composition gradients (Chabrier & Baraffe 2007). It has been suggested that composition gradients can dramatically suppress the interior cooling & planetary contraction. Would such a model be able to explain some of the close-in inflated planets?

- Can the solar system planets be better described with an inhomogeneous model?

  - Can Helium rain in Saturn explain its excess luminosity and Helium deficiency (Stevenson & Salpeter 1977b;a, Fortney & Hubbard 2004)? There has never been a quantitative investigation of how He gradients effect planetary cooling.

  - To what extent does core erosion in Jupiter and Saturn occur and what is its importance in the evolution of these planets (Wilson & Militzer 2012b;a)?

  - Can the intrinsic luminosity of Uranus, but relatively large luminosity of Neptune be explained? One explanation is that a remnant composition gradient. leftover from formation, is found in Uranus, but not in Neptune.

The long term objective of this work is to use the open source stellar evolution code MESA to describe some of these problems. MESA has already been shown to model Jupiter-type planets with a purely H/He envelope (Paxton et al. 2011). For the

applications discussed above, the giant planet can't be described by well-defined layers of H/He, water, and rock. In this work, I have developed an equation of state that mixes multiple species, with their own independent equation of state. This add-on to the MESA framework is a step towards addressing the problems above. The focus of this document is in showing that the equation of state is functioning correctly.

This work is an improvement to MESA in that there is no current way to implement high heavy element composition ratios using the current EOS. However, such a realistic EOS becomes more important for low-mass giant planets, where heavy elements make up a non-negligible fraction of the planet's mass.

5.2 Using MESA for Planet Evolution

Stellar evolution codes evolve each zone separately, while maintaining hydrostatic equilibrium. This is therefore the ideal type of method for understanding the coupling between the interior composition profile and transport mechanisms inside planets. However, the typical equation of state for a stellar evolution code is not suited for describing planets with significant amounts of heavy elements.

MESA itself is an open-source stellar evolution code that has broad support in the general astrophysics community. It has been developed primarily by Bill Paxton at KITP, UC Santa Barbara (Paxton et al. 2011). More details about the project itself are available at `mesa.sourceforge.net` or `mesastar.org/documentation/tutorials/planet-test-cases`. These test cases exist because there is broad interest in using

MESA for planet evolution models. The MESA code is divided up into a set of libraries such as the atmosphere, structure and evolution, equation of state, etc.

MESA has already been shown to work for pure H/He planets down to masses lower than 1 M_J, with results that agree well with Baraffe et al. (2003). Atmosphere models by Guillot (2010) have also been included specifically for irradiated giant planets.

There are a large number of users working on diverse subjects. It is hoped that the broad familiarity with MESA will make the EOS module developed here easier to use for others. MESA is more tested than a stellar evolution code developed by a single individual for a specific problem. MESA has been built such that certain physics such as the equation of state can be replaced by customized code. In order to allow MESA to be used for planetary evolution calculations, I have built a modified equation of state that conforms to the MESA design requirements that allows for the mixing of multiple species. Each species must be described with its own equation of state.

5.3 Mixeos Module Objective

The mixeos module aims to allow the user to mix an arbitrary species using a rule such as the additive volume rule for an input mass fraction vector. The additive volume method assumes that species are not interacting and simply take up space

$$\frac{1}{\rho(P,T)} = \sum \frac{X_i}{\rho(P,T)} \tag{5.1}$$

This is easy to implement as the additive volume is linear in specific volume,

entropy and internal energy. It is commonly used in giant planet models. In the additive volume rule, extensive quantities such as S and E add linearly. This is only strictly true if the particles are all identical or ideal, but can be used approximately for non-ideal equations of state (Fontaine et al. 1977).

$$v(P,T) = \sum X_i v_i(P,T) \tag{5.2}$$

$$S(P,T) = \sum X_i S_i(P,T) \tag{5.3}$$

$$E(P,T) = \sum X_i E_i(P,T) \tag{5.4}$$

It is a general aim of this code to be easily modifiable such that users can - with minimal effort - add their own equation of state to see how this affects the system being modeled. An equation of state could potentially be implemented as an analytic expression such as the ideal gas law. It could also be represented through a tabular method. One tabular method that we favor is described by Timmes & Swesty (2000) where a polynomial surface is determined for the free energy. The Timmes method produces free energy derivatives which allow for continuous and thermodynamic self-consistent EOS at each point.

Alternatively, the user may also have a tabular representation for Pressure, Internal Energy, and Entropy as independent tables. A disadvantage of this method is that the tables may not be self consistent with each other. However, it may be easier to guarantee smooth surfaces.

5.4 Design Overview

The mixeos library is actually composed of multiple Fortran modules in the MESA style. Within MESA there are public modules which are meant to be accessed by routines outside of the mixeos library. These provide the standard interface that is required by MESA for an alternative EOS.

There are also private modules. The private modules focus on the actual details of adding N equations of state using the additive volume method. In order to allow for the easiest extensibility, an individual EOS is a derived class of the base_eos object. The base_eos describes a standard interface that an implementation must conform to. When the mixeos module is handling the implementations it does not need to, nor is it desirable, for it to know the details of that implementation. A disadvantage may be that the object oriented Fortran features could potentially be slower than a direct implementation, or potentially even buggy as they are relatively new. The private module mixoes_mod puts everything together by implementing the required interface functions. It uses tested thermodynamic subroutines for standard transformations. The EOS tables are stored in a list - as pointers to the parent class. This is where the polymorphic behavior is occurring since mixeos_mod does not know how the EOS for each material is implemented.

5.5 Design Details

The following is the basic definition for the base_eos class.

See private/base_eos_mod.f also defines the interface for these type-bound procedures

```
type :: base_eos
   private
   character(len=256) :: name
 contains

   procedure :: Destroy => Destroy_base

   procedure :: set_name
   procedure :: get_name
   procedure :: DT_get => DT_get_base
   procedure :: PT_get => PT_get_base
   procedure :: PT_get_PRhorange => PT_get_PRhorange_base
   procedure :: PT_get_Trange => PT_get_Trange_base
end type base_eos
```

A derived equation of state class is defined in ideal_eos_mod.f with the following type definition

```
type, extends(base_eos) :: ideal_eos
   private
   real(dp) :: mu, lnalpha, m, alpha, lnN_A_mu
 contains
   procedure :: Construct => construct_ideal_eos

   procedure :: DT_get => DT_get_ideal
   procedure :: PT_get => PT_get_ideal
   procedure, private :: DT_getP => DT_getP_ideal
   procedure, private :: PT_getD => PT_getD_ideal
   procedure :: PT_get_PRhorange => PT_get_PRhorange_ideal
   procedure :: PT_get_Trange => PT_get_Trange_ideal
end type ideal_eos
```

Each of these overloaded type-bound procedures are defined in the ideal_eos_mod module.

Inside mixeos_mod.f, we can see the benefit of using the object oriented method. We have a list of pointers to equation of state objects. Inside the mixing module, it isn't desirable to be obligated to understand the details of the equation of state implementation. This allows us to write abstract code for the mixing routine that will work in general.

```
integer, parameter :: NUM_METALS = 5
type,private :: eos_entry
   class (base_eos), pointer :: eos_ptr
   integer :: isotope_number = 0
end type eos_entry
type(eos_entry), private :: mixeos_list(NUM_METALS)
```

One last aspect is necessary to mention. The user specifies to the mixeos module what equation of state they would like to use with a subroutine defined in mixeos_lib.f defined for the specific equation of state implementation. Here are the argument list for two functions that allow you to either create a Helmholtz free energy tabular object or an ideal gas object. After the object is setup, it is added to the list mixeos_list, which is defined in mixeos_mod.f.

```
subroutine mixeos_add_h5tbl(Xsize, Ysize, filename, name, &
  minlogRhoAlpha, minlogRhoBeta, maxlogRhoAlpha, maxlogRhoBeta, ierr)
 ...

subroutine mixeos_add_ideal(mu, name)
 ...
```

When the mixing equation of state is being used, it calls the equation of state for each substance in a loop similar to the following.

```
do i=1, ndef_metals
  current_eos_ptr => mixeos_list(i)%eos_ptr
```

```
  ...
  call current_eos_ptr%PT_get(P, T, Rho, &
           Pvect, Evect, Svect, weight, ierr)
  ...
enddo

...
call AddVolMix(VolMat_PT, SMat_PT, EMat_PT, X_i, NUM_METALS+1, &
          VolVect_mixPT, EVect_mixPT, SVect_mixPT)
```

This specifically demonstrates how the object-oriented behavior allows us to use the equation of state for a specific material without having to be aware of the details of its implementation. The function AddVolMix is defined in thermo.f and performs the additive volume step.

5.6 MESA standard Hydrogen-Helium EOS Representations

MESA provides a Hydrogen-Helium EOS that is designed to work over many orders of magnitude. The library provides function calls that work in Density-Temperature space as well as Pressure-Temperature space. MESA has been designed so that the dependent coordinates can be either Density-Temperature or Pressure-Temperature. To provide this MESA constructs a pre-computed tabular representation for both coordinate systems. The mixing equation of state uses the MESA EOS for the H/He component and then uses a user-specified equation of state for the heavy element component(s). The additive volume occurs for two species with the same pressure and temperature and as a result, the mixing equation of state is fastest if it is called with

pressure and temperature as independent variables. When density and temperature are used as independent variables, the package performs a less efficient, but functional, root find over pressure for a fixed temperature, which typically takes on the order of 10 function calls.

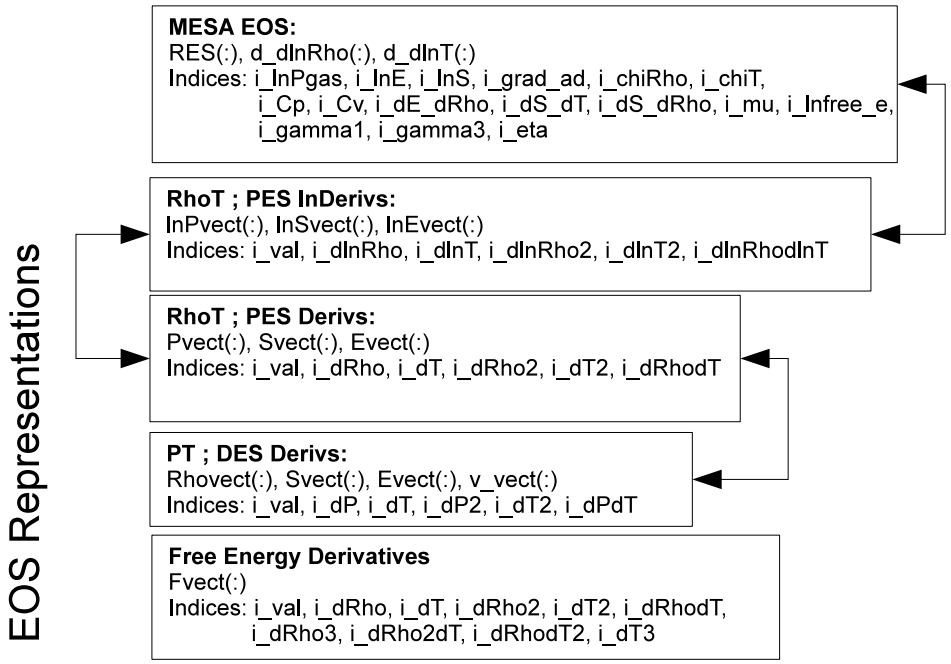

Figure 5.1: The equation of state at a given point can be represented in multiple different ways. Inside the mixeos module, the transformations convert the equation of state between representations. These transformation functions are defined in the file thermo.f and have been well tested for correctness.

The equation of state from MESA is represented in a slightly different way than is convenient for the additive volume calculation. In Figure 5.1 I outline a few of the different representations of the equation of state that I have developed for the mixing

equation of state. The MESA representation consists of three vectors: res, d_dlnRho, d_dlnT with each index of these vectors describe an individual thermodynamic quantity, in the case of res or a derivative of the thermodynamic quantity, in the case of d_dlnRho or d_dlnT. The list of indices are defined in eos_def.f from MESA itself and are:

```
integer, parameter :: i_lnPgas = 1
! gas pressure (total pressure minus radiation pressure)
integer, parameter :: i_lnE = 2
! internal energy per gram
integer, parameter :: i_lnS = 3
! entropy per gram
integer, parameter :: i_grad_ad = 4
! dlnT_dlnP at constant S
integer, parameter :: i_chiRho = 5
! dlnP_dlnRho at constant T
integer, parameter :: i_chiT = 6
! dlnP_dlnT at constant Rho
integer, parameter :: i_Cp = 7
! dh_dT at constant P, specific heat at constant total pressure
! where h is enthalpy, h = E + P/Rho
integer, parameter :: i_Cv = 8
! dE_dT at constant Rho, specific heat at constant volume
integer, parameter :: i_dE_dRho = 9
! at constant T
integer, parameter :: i_dS_dT = 10
! at constant Rho
integer, parameter :: i_dS_dRho = 11
! at constant T
integer, parameter :: i_mu = 12
! mean molecular weight per gas particle (ions + free electrons)
integer, parameter :: i_lnfree_e = 13
! free_e := total combined number per nucleon of free e- and e+
integer, parameter :: i_gamma1 = 14
! dlnP_dlnRho at constant S
integer, parameter :: i_gamma3 = 15
! gamma3 - 1 = dlnT_dlnRho at constant S
integer, parameter :: i_eta = 16
! electron degeneracy parameter (eta > 1 for significant degeneracy)
! eta = ratio of electron chemical potential to kT
```

The second representation in Figure 5.1 is composed of three vectors: lnPvect, lnEvect, and lnSvect for $\ln(P)$, $\ln(E)$, and $\ln(S)$. Each of these are 6-component vectors that for the value, first derivatives, and second derivatives in natural log space. Derivatives are with respect to $\ln(\rho)$ and $\ln(T)$. The third representation is the same as the second except that the vectors describe the behavior of P, E, and S and have derivatives with respect to ρ and T. The fourth representation is similarly organized except that the independent variables have been rotated to be P and T. Throughout this work, I often use the free energy and up to third derivatives to determine P, E and S and their derivatives up to second. By first determining the free energy derivatives, I guarantee that the output vectors will be thermodynamically self consistent. The arrows in this diagram represent some of the most frequently used functions that transition from one representation to another. For each function, the inverse is also defined. These have been and are continuously being checked for correctness. They are also described in more detail in the appendix and can be found in the mixeos/private/thermo.f module.

5.7 Testing the library

To check that the additive volume rule is working correctly, the density, internal energy and entropy have been plotted as a function of water mass fraction for a fixed Pressure and Temperature in Figures 5.2 and 5.3, and 5.4. The analytic relationship is plotted in red and perfectly fits these points. I use the end points of Z water = 0 and Z water = 1 to calculate the analytic relationship. This plot demonstrates that with

respect to ρ, E and S, the additive volume rule in the code is behaving as expected.

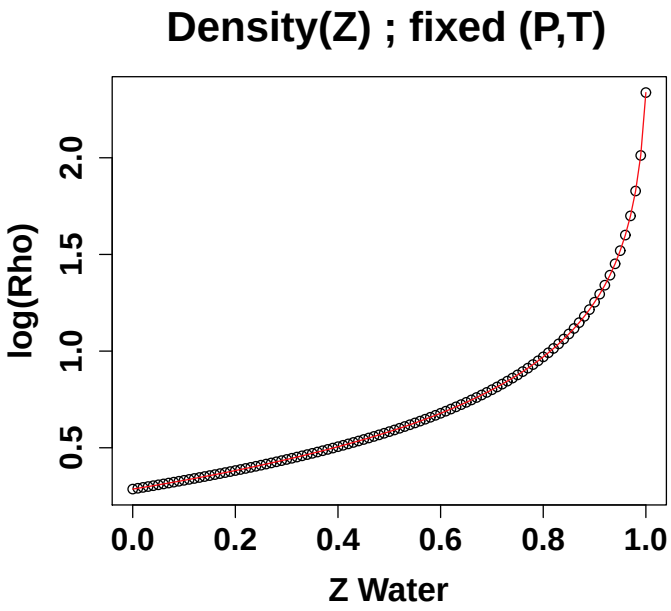

Figure 5.2: The density as a function of water mass fraction for fixed pressure = 10^{13} dyne/cm^2 and temperature = 10^5 K. The points are the output density from calls to the mixeos library. The red line is the analytic relationship that is determined by using the endpoints. This shows no unexpected behavior in the additive volume rule.

An ongoing concern in developing this software has been checking smoothness. Any lack of smoothness is likely due to data issues rather than a software problem. For the MESA H/He equation of state, it is known that the data is unphysical and appears to also have strange discontinuities at low temperature and high pressure. The hope that we have is to generally avoid that region such that the table is still useful. In Figure 5.5, 5.6, 5.7, 5.8, 5.9, and 5.10, I have plotted $\log \rho$, $\log E$, $\log S$, $\nabla_{\rm ad}$, C_p, and C_v respectively. These plots are for a mixture of 50% MESA H/He, 50% ideal water.

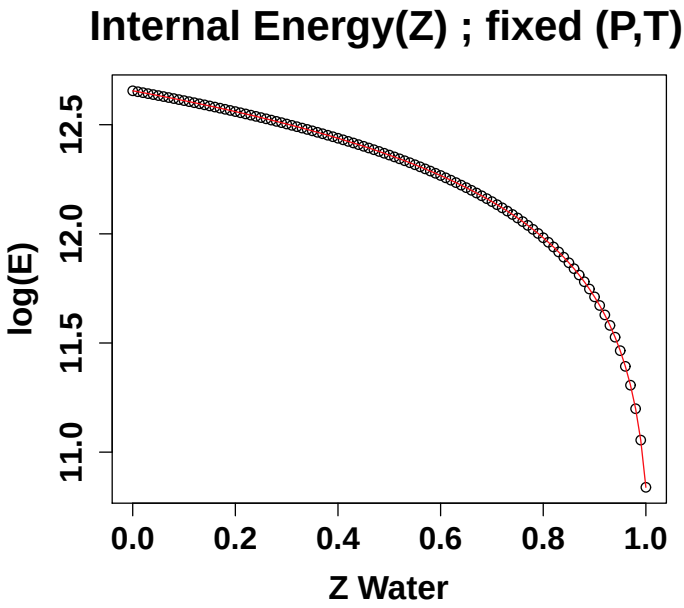

Figure 5.3: The internal energy as a function of water mass fraction for fixed pressure = 10^{13} dyne/cm^2 and temperature = 10^5 K. The red line is the analytic relationship that is derived using the endpoints. This plot shows no unexpected behavior from the additive volume rule.

Ideal water is an analytic equation of state - described in the Appendix, which we are using because it is believed to be problem free. When using tabular equation of states for representing heavy elements such as water, it was not clear if issues were due to the tabular method, the tabular data itself, or the mixing methods. Ideal water is being used as a control such that the mixing methods can be first shown to work.

In these figures, the green line denotes the low temperature or high pressure boundary where the H/He equation of state data is generally coherent. Planet profiles are also plotted in various colors: blue for HD 80606 b, purple for Jupiter, Yellow for

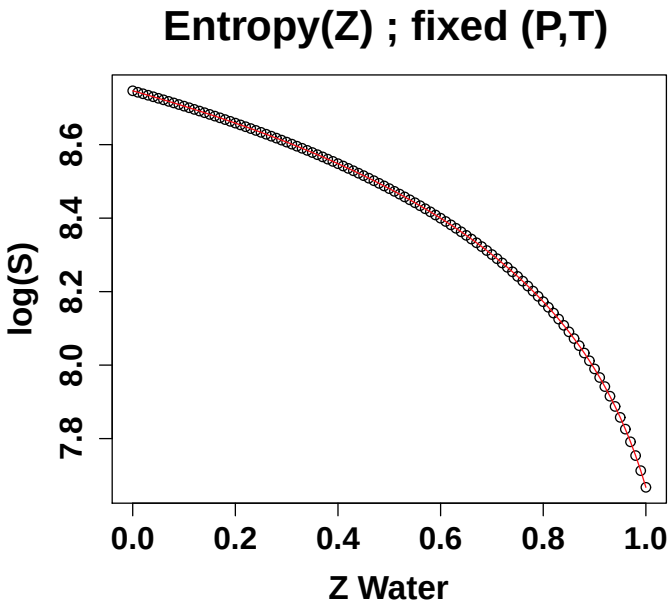

Figure 5.4: The entropy as a function of water mass fraction for fixed pressure = 10^{13} dyne/cm^2 and temperature = 10^5 K. The red line is the analytic relationship that is derived using the endpoints. This plot shows no unexpected behavior from the additive volume rule.

Saturn. It appears that these profiles are within the region where the H/He equation of state works. At first glance, these surfaces appear to be generally smooth in the region of planetary interiors.

Another overall concern is that the quantities in the derivatives output: d_dlnRho and d_dlnT may not be consistent with the overall behavior of the primary results output. It is important that these be consistent with the behavior of the res output because MESA uses root finding routines to determine the planetary structure and perform evolution steps. In Figure, 5.11, and 5.12 I have plotted the output derivative (black)

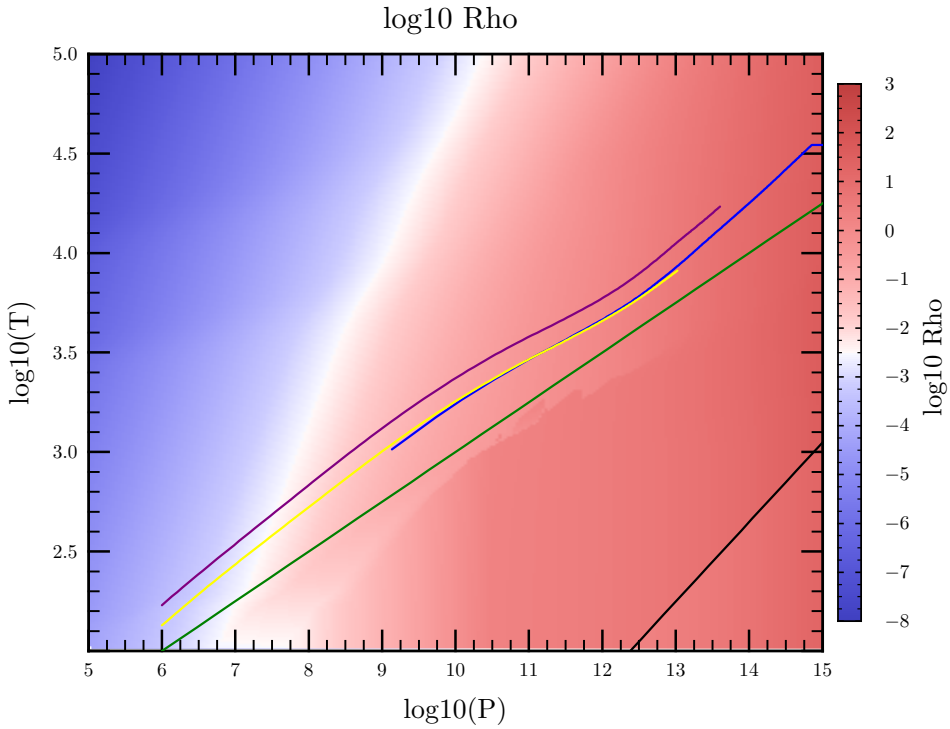

Figure 5.5: This is the result of looking up $\log_{10}(\rho)$ as a function of P and T for the mixing equation of state with 50% H/He and 50% ideal water. The H/He equation of state is questionable to the right of the green line, but this area is disjoint from where planet profiles lie. Therefore, the code attempts to avoid the region to the right of the green line. The blue profile corresponds to a model of HD 80606 b. The purple profile corresponds to a model of Jupiter. The yellow profile corresponds to a model of Saturn. The black line is a boundary that separates a region to the right where the ideal gas has negative entropy.

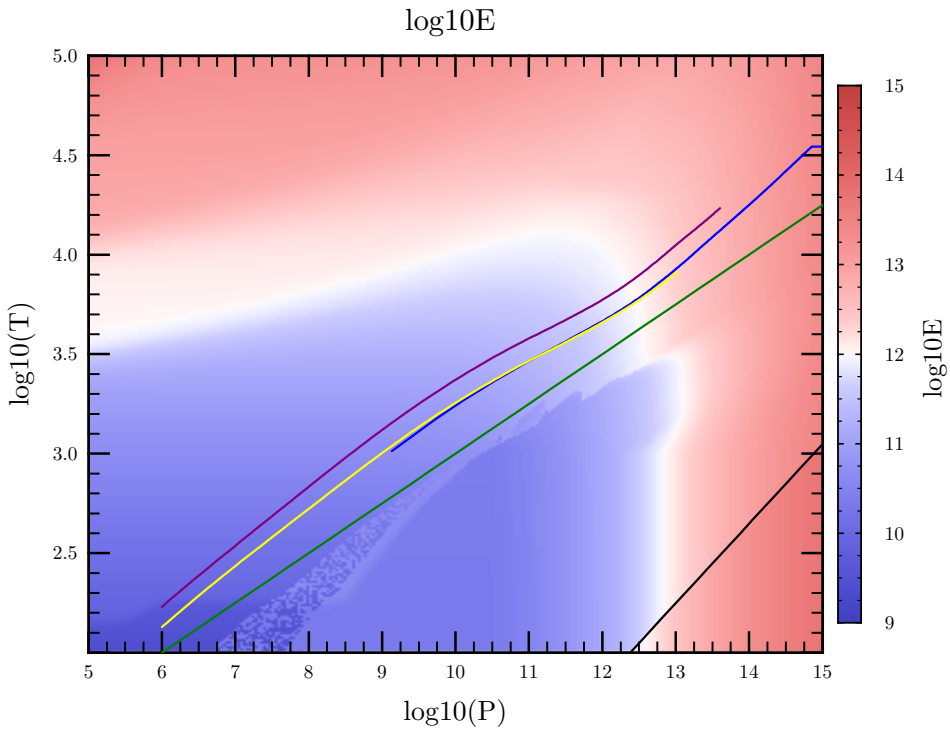

Figure 5.6: This is the result of looking up $\log_{10}(E)$ as a function of P and T for the mixing equation of state with 50% H/He and 50% ideal water. Profiles are similarly colored to Figure 5.5.

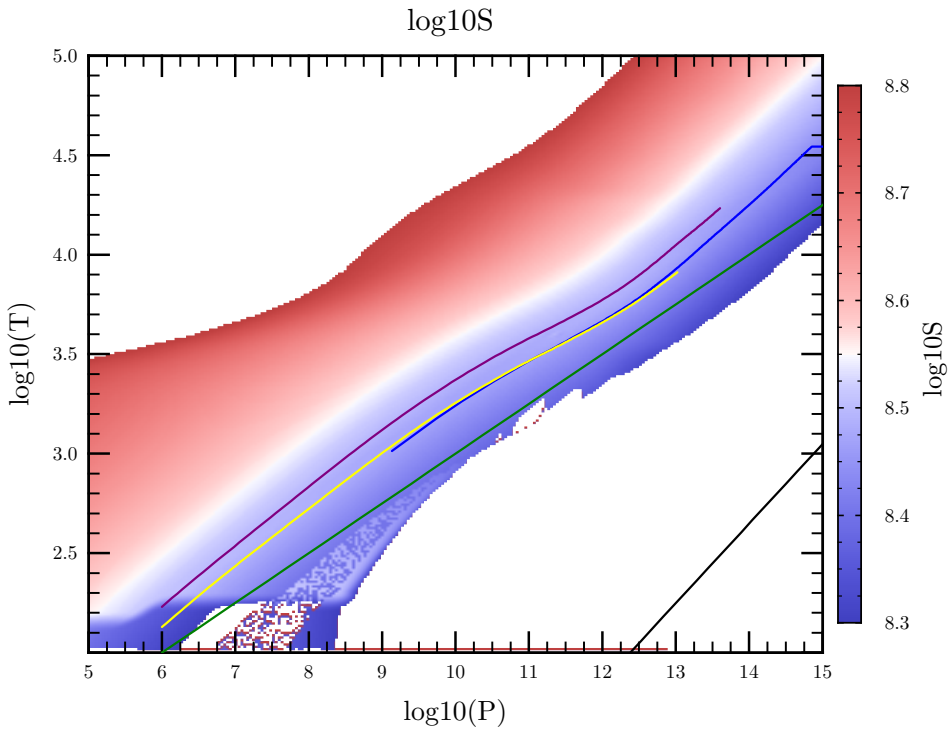

Figure 5.7: This is the result of looking up $\log_{10}(S)$ as a function of P and T for the mixing equation of state with 50% H/He and 50% ideal water. Profiles are similarly colored to Figure 5.5.

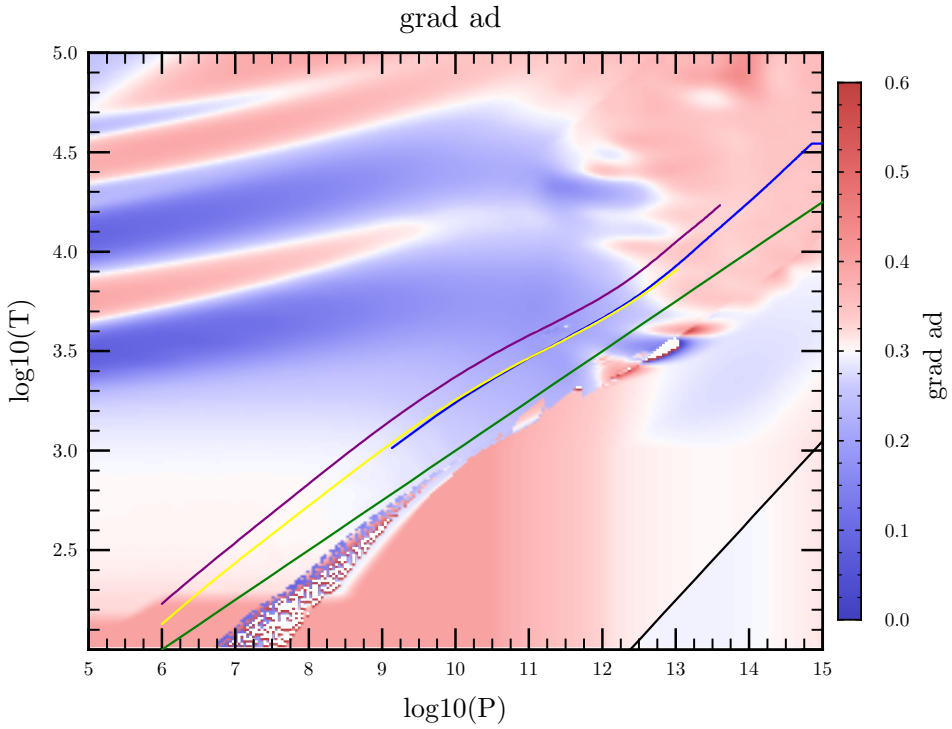

Figure 5.8: This is the result of looking up $\nabla_{\rm ad}$ as a function of P and T for the mixing equation of state with 50% H/He and 50% ideal water. Profiles are similarly colored to Figure 5.5. Structure in the upper left is due to H and He ionization

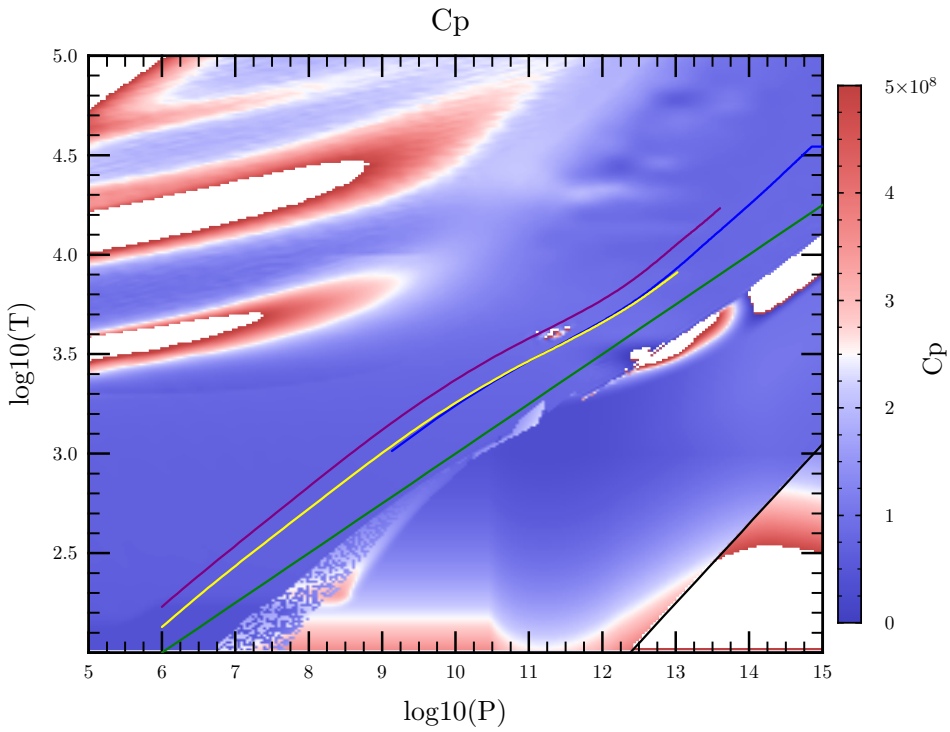

Figure 5.9: This is the result of looking up C_p as a function of P and T for the mixing equation of state with 50% H/He and 50% ideal water. Profiles are similarly colored to Figure 5.5.

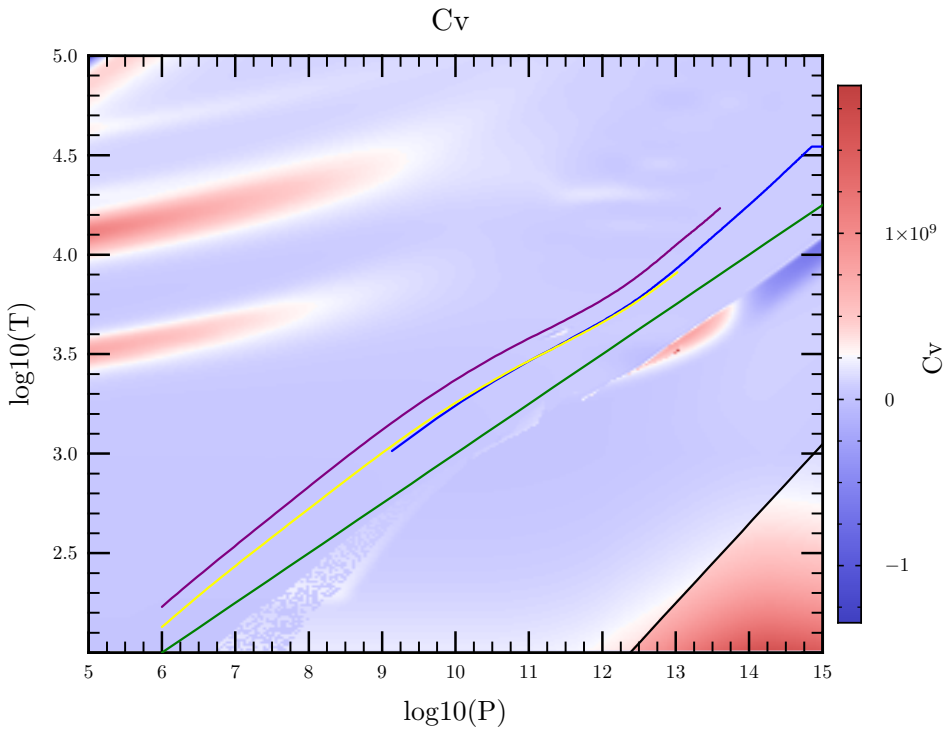

Figure 5.10: This is the result of looking up C_v as a function of P and T for the mixing equation of state with 50% H/He and 50% ideal water. Profiles are similarly colored to Figure 5.5.

against the numeric derivative of the output (red). The adiabatic gradient is an interesting quantity to plot here because it is critical for the structure of the planet. In development there previously existed bugs where the behavior of $\nabla_{\rm ad}$ deviated from its derivatives. were different, Building the adiabatic gradient is not directly represented in the additive volume step. Note that for this figure, the mixture is 50% MESA H/He, 50% ideal water. Although there isn't a perfect match, the numeric derivative appears to closely follow the derivative from the equation of state.

5.8 Setting up the mixing EOS with MESA

The mixeos code repository is on bitbucket at `https://bitbucket/org/NeilMiller/mixeos`. After cloning the repository to a local directory, you will need to build and export the library to your MESA library.

If you are planning on using your own equation of state tables, then you may want to construct them at this point. This task may not be trivial. The mixeos currently implements the Helmholtz free energy equation of state table (Timmes & Swesty 2000), the ideal gas analytic equation of state (for testing), and work has been partially completed on another representation, which I call the three-table approach. The $\log(P)$, $\log(E)$, $\log(S)$ tables are independently passed to this equation of state. The downside of this approach is that the output is not guaranteed to be thermodynamically self consistent. However, it may be easier to build smooth tables than the Helmholtz free energy approach. Just to get started, the user may want to use the ideal gas implementation

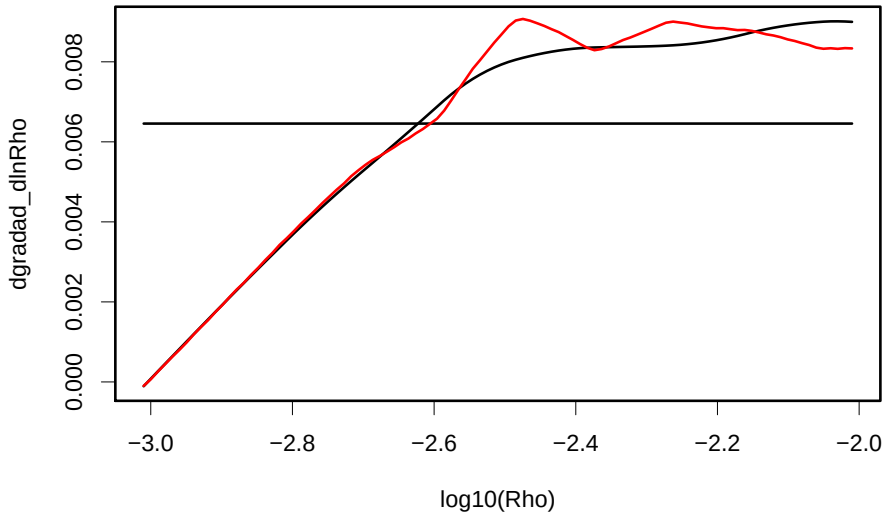

Figure 5.11: $d\nabla_{\rm ad}/d\ln\rho$ from the EOS itself (black) and the numeric derivative with respect to $\ln(\rho)$ of $\nabla_{\rm ad}$ (red). The Temperature is fixed to be 10^3 K. This test shows that the behavior of the output value behaves fairly similarly to the derivative. The horizontal line is the average value of the derivative of $\nabla_{\rm ad}$ over the interval. It appears that the numerical derivative and derivative of the adiabatic gradient somewhat closely agree.

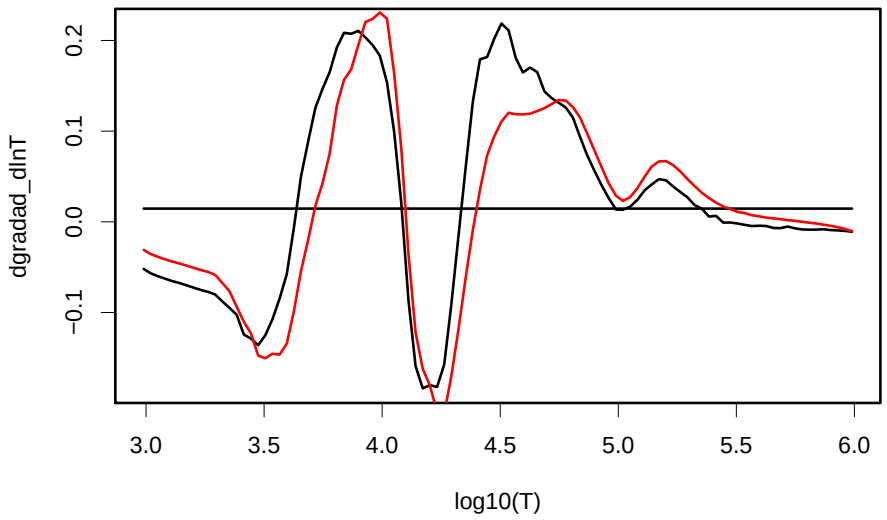

Figure 5.12: $d\nabla_{\rm ad}/d\ln T$ from the EOS itself (black) and numeric derivative of the with respect to T of $\nabla_{\rm ad}$ (red). This test is for a fixed density of 10^{-3} g / cm^3 varying only temperature. This also shows relatively close consistency between the output value and the derivative. The horizontal line is the average value of the derivative of $\nabla_{\rm ad}$ over the interval.

and then do this step later.

5.8.1 Setting up Evolution Runs

Append water to the list of isotopes (chem/chem_data/isotopes.data)

```
water      18.0     0   18   0.0   0.0
 1.0E+0  1.0E+0  1.0E+0  1.0E+0  1.0E+0  1.0E+0  1.0E+0  1.0E+0
 1.0E+0  1.0E+0  1.0E+0  1.0E+0  1.0E+0  1.0E+0  1.0E+0  1.0E+0
 1.0E+0  1.0E+0  1.0E+0  1.0E+0  1.0E+0  1.0E+0  1.0E+0  1.0E+0
```

The user should add any other species in a similar way that are defined in the mixeos library.

The nuclear network needs to also be modified. Here is an example file of my "planet.net"

```
      add_isos(
         h1
         he3
         he4
         c12
         n14
         o16
         ne20
         mg24
         water
         )

      add_reactions(

         ! pp chains

         rpp_to_he3          ! p(p e+nu)h2(p g)he3
         rpep_to_he3         ! p(e-p nu)h2(p g)he3
         r_he3_he3_to_h1_h1_he4       ! he3(he3 2p)he4
         r34_pp2             ! he4(he3 g)be7(e- nu)li7(p a)he4
         r34_pp3             ! he4(he3 g)be7(p g)b8(e+ nu)be8( a)he4
         r_h1_he3_wk_he4              ! he3(p e+nu)he4
```

```
   ! cno cycles

   rc12_to_n14         ! c12(p g)n13(e+nu)c13(p g)n14
   rn14_to_c12         ! n14(p g)o15(e+nu)n15(p a)c12
   rn14_to_o16         ! n14(p g)o15(e+nu)n15(p g)o16
   ro16_to_n14         ! o16(p g)f17(e+nu)o17(p a)n14

   ! helium burning

   r_he4_he4_he4_to_c12

   r_c12_ag_o16
   rc12ap_to_o16       ! c12(a p)n15(p g)o16

   rn14ag_lite         ! n14 + 1.5 alpha = ne20

   r_o16_ag_ne20
   ro16ap_to_ne20      ! o16(a p)f19(p g)ne20

   r_ne20_ag_mg24
   rne20ap_to_mg24     ! ne20(a p)na23(p g)mg24

   ! auxiliaries

   rbe7ec_li7_aux
   rbe7pg_b8_aux
   rn14pg_aux
   rn15pg_aux
   rn15pa_aux
   ro16ap_aux
   rf19pg_aux
   rf19pa_aux
   rne20ap_aux
   rna23pg_aux
   rna23pa_aux

   )
```

You need to tell MESA that you are using this network inside the inlist file with

```
change_net = .true.
```

```
new_net_name = 'planet.net'
```

Inside the run/src, Modify the file run_star_extras.f so that the "extra_controls" routine tell MESA to use our custom "other_eos".

```
subroutine extras_controls(s, ierr)
   type (star_info), pointer :: s
   integer, intent(out) :: ierr
   real(dp) :: mu
   character (len=256) :: name

   ierr = 0

   write(*,*) "Setting custome EOS => mixeos"
   s% other_eosDT_get              => mixeos_get
   s% other_eosDT_get_T            => mixeos_get_t
   s% other_eosDT_get_Rho          => mixeos_get_rho
   s% other_eosPT_get              => mixeosPT_get
   s% other_eosPT_get_T            => mixeosPT_get_T
   s% other_eosPT_get_Pgas         => mixeosPT_get_Pgas
   s% other_eosPT_get_Pgas_for_Rho => mixeosPT_get_Pgas_for_Rho
   s% use_other_eos = .true.

   name = "water"
   mu = 18.d0
   call mixeos_add_ideal(mu, name)
end subroutine extras_controls
```

This connects MESA to our custom other_eos library. The line s% use_other_eos = .true. is the switch that MESA uses to determine if it should use these other_eos functions.

The mixeos library has been setup such that the user calls initialization functions like mixeos_add_ideal. This function both creates an object for an ideal gas equation of state with $\mu = 18.$ as well as adds it to the list of metal EOS tables inside of mixeos. Because the implementation is object-oriented, other EOS representations built

in a similar way and integrated into the mixeos library.

5.9 Evolution Run

I have constructed an evolution run by modifying the irradiated planet test case (0.001 M_s) to show that the mixeos module works correctly without any additional species. This applies the MESA H/He EOS through the mixing EOS, but without mixing in another species. This is plotted in black in Figure 5.13. The idential evolution run with the mixing equation of state is shown in green. This base case demonstrates that in the null case, the mixing equation of state does not behave significantly different than the origonal equation of state.

I have also constructed planet evolution runs with Jupiter-like water mass fraction ($Z_{\rm water} = 0.02$) as shown in Figure 5.14. The black line here corresponds to the run with $Z_{\rm water} = 0.00$ mass fraction of water, while the red line corresponds to $Z_{\rm water} = 0.02$ mass fraction water. The $Z_{\rm water} = 0.02$ mass fraction of water has a smaller radius as expected.

5.10 Conclusion

This chapter has presented a mixing equation of state code designed for using within the MESA stellar evolution code. The code has been developed with flexibility in mind with the hope that other researchers may be easily able to use it. Test cases have been presented that demonstrate that the EOS is smooth, self-consistent, and behaves

Figure 5.13: This is a comparison of the evolution run using the mixing equation of state and the origonal MESA EOS. The mixing EOS is only using the H/He, however since the H/He EOS values are being run through the mixing machinery, they are slightly different in the mixing model. The black line is the origonal EOS thermal evolution run, while the green line is the mixing EOS thermal evolution run.

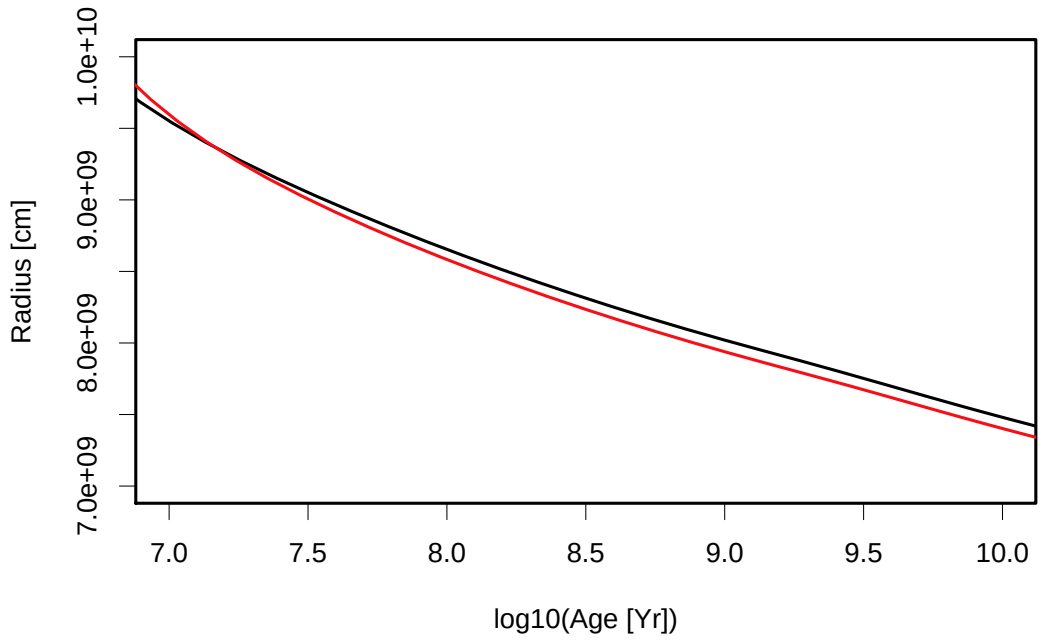

Figure 5.14: This is a comparison of the evolution run using the mixing equation of state with purely Hydrogen and Helium ($Z_{\rm water}$=0) and Jupiter-like composition ($Z_{\rm water}$=0.02). The black line is the evolution run with $Z_{\rm water}$=0 and the red line is the evolution run with $Z_{\rm water}$=0.02. The planet that is metal enriched has a smaller radius, which is expected.

as expected. This chapter has also discussed how to use the EOS inside of MESA.

Chapter 6

Conclusions and Future Directions

In summary, this thesis has examined various aspects of the structure and evolution of giant planets. Here, I summarize the overall findings.

In Chapter 2, tidal heating as a mechanism for inflating hot Jupiters was examined for a sample of systems. Although tidal heating through orbital circularization may be able to temporarily increase the radii of planets for short periods of time, this requires that many of these systems are being observed at a special time as they often concurrently have small eccentricity. This would require that they be observed just after the orbit was approximately circularized. However, these planets should contract in less than 100 Myrs. Also, in some cases our model is not able to pump enough energy into the planet to achieve the radius given the observed orbital parameters. Tidal evolution processes however are certainly important for the dynamics of these planets. Tides on the star induced by the planet will take angular momentum from the planet and cause the planet to migrate inward. At some point, the planet may fall into the parent star.

The planet may also undergo various mass loss processes that would intensify as the planet moved closer to the parent star.

In Chapter 3, the tidal-thermal evolution model is applied to a few especially interesting systems: CoRoT-2b, CoRoT-7b, and Kepler-11. The CoRoT-2 system is fairly young and the planet CoRoT-2b is inflated. This planet can be explained through tidal heating, but can't be explained under a normal contraction model. CoRoT-7b is a rocky planet in a fairly close-in orbit to its parent star. A mass loss evolution model was explored and it was found that this planet could have originally been as large as 200 Earth masses. Finally, we investigate Kepler-11, a six transiting planet system. The thermal evolution and structure model allows us to infer the interior composition for these planets by comparing to the theoretical mass-radius relation.

In Chapter 4, a population of Jupiter class planets were focused on that had low levels of incident flux. These systems did not indicate any evidence of being inflated relative to our cooling model. By assuming that the inflation mechanism does not extend out to these planets - with low levels of incident flux, we can use our thermal evolution models to infer the heavy element mass required for these planets. By focusing on this subsample, we are able to avoid making an assumption about the behavior of the heating mechanism. We find that the heavy element mass inside each system increases for higher metallicity systems. It appears that there is a lower bound on the amount of heavy elements in each system, which may be evidence for the core accretion formation scenario. We also find that although the amount of heavy elements implied by the models increases with more massive planets, the planet's enrichment decreases with

mass. This is similar to the pattern found in the solar system.

In Chapter 5, a custom equation of state for mixing multiple species, extending the MESA stellar evolution code, is presented. The focus of this section is to show that the equation of state is correctly mixing multiple species. The EOS is shown to produce a smooth mixture in the region where the planetary profile lies. The derivatives of the equation of state outputs are compared with the actual variance of these same EOS outputs and agree well.

6.0.1 Future Work

The MESA planet project is an ongoing effort.

- Substitute a more realistic equation of state for water such as ANEOS such that the EOS is a better description of a physically realistic scenario
- Build planet evolution models with intrinsic composition gradients. Preliminary work in this area appears promising. MESA appears to interface with the mixing EOS and can perform initial structure and evolution steps.
- Build planet models with evolving composition gradients that are coupled to the thermal evolution of the planet.

The study of composition of giant exoplanets will also be an interesting arena going forward. It will be interesting to see how the composition for the less irradiated giant planets evolves with increased sample sizes. If a strong relationship can be found,

then it may be useful for inferring the heavy element fraction for inflated planets. This may be useful for understanding the radius inflation mechanism.

Bibliography

Arras, P. & Socrates, A. 2010, *ApJ*, **714**, 1

Asplund, M., Grevesse, N., Sauval, A. J., & Scott, P. 2009, *ARA&A*, **47**, 481

Bakos, G. Á., Torres, G., Pál, A., Hartman, J., Kovács, G., Noyes, R. W., Latham, D. W., Sasselov, D. D., Sipőcz, B., Esquerdo, G. A., Fischer, D. A., Johnson, J. A., Marcy, G. W., Butler, R. P., Isaacson, H., Howard, A., Vogt, S., Kovács, G., Fernandez, J., Moór, A., Stefanik, R. P., Lázár, J., Papp, I., & Sári, P. 2010, *ApJ*, **710**, 1724

Baraffe, I., Chabrier, G., Barman, T. S., Allard, F., & Hauschildt, P. H. 2003, *A&A*, **402**, 701

Baraffe, I., Selsis, F., Chabrier, G., Barman, T. S., Allard, F., Hauschildt, P. H., & Lammer, H. 2004, *A&A*, **419**, L13

Batygin, K., Stevenson, D. J., & Bodenheimer, P. H. 2011, *ArXiv e-prints*

Bodenheimer, P., Laughlin, G., & Lin, D. N. C. 2003, *ApJ*, **592**, 555

Bodenheimer, P., Lin, D. N. C., & Mardling, R. A. 2001, *ApJ*, **548**, 466

Boley, A. C. & Durisen, R. H. 2010, *ApJ*, **724**, 618

Bonomo, A. S., Santerne, A., Alonso, R., Gazzano, J., Havel, M., Aigrain, S., Auvergne, M., Baglin, A., Barbieri, M., Barge, P., Benz, W., Bordé, P., Bouchy, F., Bruntt, H., Cabrera, J., Cameron, A. C., Carone, L., Carpano, S., Csizmadia, S., Deleuil, M., Deeg, H. J., Dvorak, R., Erikson, A., Ferraz-Mello, S., Fridlund, M., Gandolfi, D., Gillon, M., Guenther, E., Guillot, T., Hatzes, A., Hébrard, G., Jorda, L., Lammer, H., Lanza, A. F., Léger, A., Llebaria, A., Mayor, M., Mazeh, T., Moutou, C., Ollivier, M., Pätzold, M., Pepe, F., Queloz, D., Rauer, H., Rouan, D., Samuel, B., Schneider, J., Tingley, B., Udry, S., & Wuchterl, G. 2010, *A&A*, **520**, A65+

Bordé, P., Bouchy, F., Deleuil, M., Cabrera, J., Jorda, L., Lovis, C., Csizmadia, S., Aigrain, S., Almenara, J. M., Alonso, R., Auvergne, M., Baglin, A., Barge, P., Benz, W., Bonomo, A. S., Bruntt, H., Carone, L., Carpano, S., Deeg, H., Dvorak, R., Erikson, A., Ferraz-Mello, S., Fridlund, M., Gandolfi, D., Gazzano, J., Gillon, M., Guenther, E., Guillot, T., Guterman, P., Hatzes, A., Havel, M., Hébrard, G., Lammer, H., Léger, A., Mayor, M., Mazeh, T., Moutou, C., Pätzold, M., Pepe, F., Ollivier, M., Queloz, D., Rauer, H., Rouan, D., Samuel, B., Santerne, A., Schneider, J., Tingley, B., Udry, S., Weingrill, J., & Wuchterl, G. 2010, *A&A*, **520**, A66+

Borucki, W. J., Koch, D. G., Basri, G., Batalha, N., Brown, T. M., Bryson, S. T., Caldwell, D., Christensen-Dalsgaard, J., Cochran, W. D., DeVore, E., Dunham, E. W., Gautier, III, T. N., Geary, J. C., Gilliland, R., Gould, A., Howell, S. B., Jenkins, J. M., Latham, D. W., Lissauer, J. J., Marcy, G. W., Rowe, J., Sasselov, D., Boss, A.,

Charbonneau, D., Ciardi, D., Doyle, L., Dupree, A. K., Ford, E. B., Fortney, J., Holman, M. J., Seager, S., Steffen, J. H., Tarter, J., Welsh, W. F., Allen, C., Buchhave, L. A., Christiansen, J. L., Clarke, B. D., Désert, J., Endl, M., Fabrycky, D., Fressin, F., Haas, M., Horch, E., Howard, A., Isaacson, H., Kjeldsen, H., Kolodziejczak, J., Kulesa, C., Li, J., Machalek, P., McCarthy, D., MacQueen, P., Meibom, S., Miquel, T., Prsa, A., Quinn, S. N., Quintana, E. V., Ragozzine, D., Sherry, W., Shporer, A., Tenenbaum, P., Torres, G., Twicken, J. D., Van Cleve, J., & Walkowicz, L. 2011, *ArXiv e-prints*

Boss, A. P. 2001a, *ApJ*, **551**, L167

Boss, A. P. 2001b, *ApJ*, **563**, 367

Burrows, A., Hubeny, I., Budaj, J., & Hubbard, W. B. 2007, *ApJ*, **661**, 502

Burrows, A., Sudarsky, D., & Hubbard, W. B. 2003, *ApJ*, **594**, 545

Chabrier, G. & Baraffe, I. 2007, *ApJ*, **661**, L81

Chabrier, G., Gallardo, J., & Baraffe, I. 2007, *A&A Letters in press, astro-ph/0707.1792*

Charbonneau, D., Allen, L. E., Megeath, S. T., Torres, G., Alonso, R., Brown, T. M., Gilliland, R. L., Latham, D. W., Mandushev, G., O'Donovan, F. T., & Sozzetti, A. 2005, *ApJ*, **626**, 523

Charbonneau, D., Brown, T. M., Latham, D. W., & Mayor, M. 2000, *ApJ*, **529**, L45

Chatterjee, S., Ford, E. B., Matsumura, S., & Rasio, F. A. 2008, *ApJ*, **686**, 580

Cochran, W. D., Fabrycky, D. C., Torres, G., Fressin, F., Désert, J.-M., Ragozzine, D., Sasselov, D., Fortney, J. J., Rowe, J. F., Brugamyer, E. J., Bryson, S. T., Carter, J. A., Ciardi, D. R., Howell, S. B., Steffen, J. H., Borucki, W. J., Koch, D. G., Winn, J. N., Welsh, W. F., Uddin, K., Tenenbaum, P., Still, M., Seager, S., Quinn, S. N., Mullally, F., Miller, N., Marcy, G. W., MacQueen, P. J., Lucas, P., Lissauer, J. J., Latham, D. W., Knutson, H., Kinemuchi, K., Johnson, J. A., Jenkins, J. M., Isaacson, H., Howard, A., Horch, E., Holman, M. J., Henze, C. E., Haas, M. R., Gilliland, R. L., Gautier, III, T. N., Ford, E. B., Fischer, D. A., Everett, M., Endl, M., Demory, B.-O., Deming, D., Charbonneau, D., Caldwell, D., Buchhave, L., Brown, T. M., & Batalha, N. 2011, *ApJS*, **197**, 7

Deeg, H. J., Moutou, C., Erikson, A., Csizmadia, S., Tingley, B., Barge, P., Bruntt, H., Havel, M., Aigrain, S., Almenara, J. M., Alonso, R., Auvergne, M., Baglin, A., Barbieri, M., Benz, W., Bonomo, A. S., Bordé, P., Bouchy, F., Cabrera, J., Carone, L., Carpano, S., Ciardi, D., Deleuil, M., Dvorak, R., Ferraz-Mello, S., Fridlund, M., Gandolfi, D., Gazzano, J., Gillon, M., Gondoin, P., Guenther, E., Guillot, T., Hartog, R. D., Hatzes, A., Hidas, M., Hébrard, G., Jorda, L., Kabath, P., Lammer, H., Léger, A., Lister, T., Llebaria, A., Lovis, C., Mayor, M., Mazeh, T., Ollivier, M., Pätzold, M., Pepe, F., Pont, F., Queloz, D., Rabus, M., Rauer, H., Rouan, D., Samuel, B., Schneider, J., Shporer, A., Stecklum, B., Street, R., Udry, S., Weingrill, J., & Wuchterl, G. 2010, *Nat*, **464**, 384

Deming, D., Seager, S., Richardson, L. J., & Harrington, J. 2005, *Nature*, **434**, 740

Erkaev, N. V., Kulikov, Y. N., Lammer, H., Selsis, F., Langmayr, D., Jaritz, G. F., & Biernat, H. K. 2007, *A&A*, **472**, 329

Fabrycky, D. & Tremaine, S. 2007, *ApJ*, **669**, 1298

Fabrycky, D. C. & Winn, J. N. 2009, *ApJ*, **696**, 1230

Fontaine, G., Graboske, Jr., H. C., & van Horn, H. M. 1977, *ApJS*, **35**, 293

Ford, E. B. & Rasio, F. A. 2008, *ApJ*, **686**, 621

Fortney, J. J. 2008, in D. Fischer, F. A. Rasio, S. E. Thorsett, & A. Wolszczan (eds.), *Astronomical Society of the Pacific Conference Series*, Vol. 398, p. 405

Fortney, J. J., Demory, B.-O., Désert, J.-M., Rowe, J., Marcy, G. W., Isaacson, H., Buchhave, L. A., Ciardi, D., Gautier, T. N., Batalha, N. M., Caldwell, D. A., Bryson, S. T., Nutzman, P., Jenkins, J. M., Howard, A., Charbonneau, D., Knutson, H. A., Howell, S. B., Everett, M., Fressin, F., Deming, D., Borucki, W. J., Brown, T. M., Ford, E. B., Gilliland, R. L., Latham, D. W., Miller, N., Seager, S., Fischer, D. A., Koch, D., Lissauer, J. J., Haas, M. R., Still, M., Lucas, P., Gillon, M., Christiansen, J. L., & Geary, J. C. 2011, *ApJS*, **197**, 9

Fortney, J. J. & Hubbard, W. B. 2003, *Icarus*, **164**, 228

Fortney, J. J. & Hubbard, W. B. 2004, *ApJ*, **608**, 1039

Fortney, J. J., Lodders, K., Marley, M. S., & Freedman, R. S. 2008, *ApJ*, **678**, 1419

Fortney, J. J., Marley, M. S., & Barnes, J. W. 2007a, *ApJ*, **659**, 1661

Fortney, J. J., Marley, M. S., & Barnes, J. W. 2007b, *ApJ*, **659**, 1661

Fortney, J. J. & Nettelmann, N. 2010, *Space Sci. Rev.*, **152**, 423

Fortney, J. J., Saumon, D., Marley, M. S., Lodders, K., & Freedman, R. S. 2006, *ApJ*, **642**, 495

Fortney, J. J., Sudarsky, D., Hubeny, I., Cooper, C. S., Hubbard, W. B., Burrows, A., & Lunine, J. I. 2003, *ApJ*, **589**, 615

Gaudi, B. S. & Winn, J. N. 2007, *ApJ*, **655**, 550

Gillon, M., Lanotte, A. A., Barman, T., Miller, N., Demory, B.-O., Deleuil, M., Montalbán, J., Bouchy, F., Collier Cameron, A., Deeg, H. J., Fortney, J. J., Fridlund, M., Harrington, J., Magain, P., Moutou, C., Queloz, D., Rauer, H., Rouan, D., & Schneider, J. 2010, *A&A*, **511**, A3

Gillon, M., Pont, F., Demory, B.-O., Mallmann, F., Mayor, M., Mazeh, T., Queloz, D., Shporer, A., Udry, S., & Vuissoz, C. 2007, *A&A*, **472**, L13

Goldreich, P. & Soter, S. 1966, *Icarus*, **5**, 375

Gu, P.-G., Bodenheimer, P. H., & Lin, D. N. C. 2004, *ApJ*, **608**, 1076

Gu, P.-G., Lin, D. N. C., & Bodenheimer, P. H. 2003, *ApJ*, **588**, 509

Guillot, T. 2010, *A&A*, **520**, A27

Guillot, T., Burrows, A., Hubbard, W. B., Lunine, J. I., & Saumon, D. 1996, *ApJ*, **459**, L35

Guillot, T. & Gladman, B. 2000, in *ASP Conf. Ser. 219: Disks, Planetesimals, and Planets, ed. F. Garzon, C. Eiroa, D. de Winter, & T. J. Mahoney (San Francisco: ASP)*, p. 475

Guillot, T., Santos, N. C., Pont, F., Iro, N., Melo, C., & Ribas, I. 2006, *A&A*, **453**, L21

Guillot, T. & Showman, A. P. 2002, *A&A*, **385**, 156

Hansen, B. M. S. & Barman, T. 2007, *ApJ*, **671**, 861

Hartman, J. D., Bakos, G. Á., Sato, B., Torres, G., Noyes, R. W., Latham, D. W., Kovács, G., Fischer, D. A., Howard, A. W., Johnson, J. A., Marcy, G. W., Buchhave, L. A., Füresz, G., Perumpilly, G., Béky, B., Stefanik, R. P., Sasselov, D. D., Esquerdo, G. A., Everett, M., Csubry, Z., Lázár, J., Papp, I., & Sári, P. 2010, *ArXiv e-prints*

Hartman, J. D., Bakos, G. Á., Torres, G., Kovács, G., Noyes, R. W., Pál, A., Latham, D. W., Sipőcz, B., Fischer, D. A., Johnson, J. A., Marcy, G. W., Butler, R. P., Howard, A. W., Esquerdo, G. A., Sasselov, D. D., Kovács, G., Stefanik, R. P., Fernandez, J. M., Lázár, J., Papp, I., & Sári, P. 2009, *ApJ*, **706**, 785

Hebb, L., Collier-Cameron, A., Loeillet, B., Pollacco, D., Hébrard, G., Street, R. A., Bouchy, F., Stempels, H. C., Moutou, C., Simpson, E., Udry, S., Joshi, Y. C., West, R. G., Skillen, I., Wilson, D. M., McDonald, I., Gibson, N. P., Aigrain, S., Anderson, D. R., Benn, C. R., Christian, D. J., Enoch, B., Haswell, C. A., Hellier, C., Horne, K., Irwin, J., Lister, T. A., Maxted, P., Mayor, M., Norton, A. J., Parley, N., Pont, F., Queloz, D., Smalley, B., & Wheatley, P. J. 2009, *ApJ*, **693**, 1920

Hébrard, G., Bouchy, F., Pont, F., Loeillet, B., Rabus, M., Bonfils, X., Moutou, C., Boisse, I., Delfosse, X., Desort, M., Eggenberger, A., Ehrenreich, D., Forveille, T., Lagrange, A.-M., Lovis, C., Mayor, M., Pepe, F., Perrier, C., Queloz, D., Santos, N. C., Ségransan, D., Udry, S., & Vidal-Madjar, A. 2008, *A&A*, **488**, 763

Helled, R., Bodenheimer, P., & Lissauer, J. J. 2010, *ArXiv e-prints*

Helled, R., Podolak, M., & Kovetz, A. 2006, *Icarus*, **185**, 64

Helled, R. & Schubert, G. 2009, *ApJ*, **697**, 1256

Hellier, C., Anderson, D. R., Collier Cameron, A., Gillon, M., Hebb, L., Maxted, P. F. L., Queloz, D., Smalley, B., Triaud, A. H. M. J., West, R. G., Wilson, D. M., Bentley, S. J., Enoch, B., Horne, K., Irwin, J., Lister, T. A., Mayor, M., Parley, N., Pepe, F., Pollacco, D. L., Segransan, D., Udry, S., & Wheatley, P. J. 2009, *Nat*, **460**, 1098

Hidas, M. G., Tsapras, Y., Mislis, D., Ramaprakash, A. N., Barros, S. C. C., Street, R. A., Schmitt, J. H. M. M., Steele, I., Pollacco, D., Ayiomamitis, A., Antoniadis, J., Nitsos, A., Seiradakis, J. H., & Urakawa, S. 2010, *MNRAS*, **406**, 1146

Holman, M. J., Fabrycky, D. C., Ragozzine, D., Ford, E. B., Steffen, J. H., Welsh, W. F., Lissauer, J. J., Latham, D. W., Marcy, G. W., Walkowicz, L. M., Batalha, N. M., Jenkins, J. M., Rowe, J. F., Cochran, W. D., Fressin, F., Torres, G., Buchhave, L. A., Sasselov, D. D., Borucki, W. J., Koch, D. G., Basri, G., Brown, T. M., Caldwell, D. A., Charbonneau, D., Dunham, E. W., Gautier, T. N., Geary, J. C., Gilliland,

R. L., Haas, M. R., Howell, S. B., Ciardi, D. R., Endl, M., Fischer, D., Fürész, G., Hartman, J. D., Isaacson, H., Johnson, J. A., MacQueen, P. J., Moorhead, A. V., Morehead, R. C., & Orosz, J. A. 2010, *Science*, **330**, 51

Howard, A. W., Bakos, G. Á., Hartman, J., Torres, G., Shporer, A., Mazeh, T., Kovacs, G., Latham, D. W., Noyes, R. W., Fischer, D. A., Johnson, J. A., Marcy, G. W., Esquerdo, G. A., Béky, B., Butler, R. P., Sasselov, D. D., Stefanik, R. P., Perumpilly, G., Lázár, J., Papp, I., & Sári, P. 2010, *ArXiv e-prints*

Hubbard, W. B., Fortney, J. J., Lunine, J. I., Burrows, A., Sudarsky, D., & Pinto, P. 2001, *ApJ*, **560**, 413

Ibgui, L. & Burrows, A. 2009, *ApJ submitted, ArXiv e-prints/0902.3998*

Ida, S. & Lin, D. N. C. 2010, *ApJ*, **719**, 810

Ikoma, M., Guillot, T., Genda, H., Tanigawa, T., & Ida, S. 2006, *ApJ*, **650**, 1150

Jackson, B., Barnes, R., & Greenberg, R. 2009, *ApJ in press, ArXiv e-prints/0904.1170*

Jackson, B., Greenberg, R., & Barnes, R. 2008a, *ApJ*, **678**, 1396

Jackson, B., Greenberg, R., & Barnes, R. 2008b, *ApJ*, **681**, 1631

Jackson, B., Miller, N., Barnes, R., Raymond, S. N., Fortney, J. J., & Greenberg, R. 2010, *MNRAS*, **407**, 910

Knutson, H. A., Charbonneau, D., Burrows, A., O'Donovan, F. T., & Mandushev, G. 2009, *ApJ*, **691**, 866

Kovács, G., Bakos, G. Á., Hartman, J. D., Torres, G., Noyes, R. W., Latham, D. W., Howard, A. W., Fischer, D. A., Johnson, J. A., Marcy, G. W., Isaacson, H., Sasselov, D. D., Stefanik, R. P., Esquerdo, G. A., Fernandez, J. M., Lázár, B. B. J., Papp, I., & Sári, P. 2010a, *ApJ*, **724**, 866

Kovács, G., Bakos, G. Á., Hartman, J. D., Torres, G., Noyes, R. W., Latham, D. W., Howard, A. W., Fischer, D. A., Johnson, J. A., Marcy, G. W., Isaacson, H., Sasselov, D. D., Stefanik, R. P., Esquerdo, G. A., Fernandez, J. M., Lázár, B. B. J., Papp, I., & Sári, P. 2010b, *ApJ*, **724**, 866

Lammer, H., Odert, P., Leitzinger, M., Khodachenko, M. L., Panchenko, M., Kulikov, Y. N., Zhang, T. L., Lichtenegger, H. I. M., Erkaev, N. V., Wuchterl, G., Micela, G., Penz, T., Biernat, H. K., Weingrill, J., Steller, M., Ottacher, H., Hasiba, J., & Hanslmeier, A. 2009, *A&A*, **506**, 399

Laughlin, G., Crismani, M., & Adams, F. C. 2011, *ApJ*, **729**, L7+

Laughlin, G., Marcy, G. W., Vogt, S. S., Fischer, D. A., & Butler, R. P. 2005, *ApJ*, **629**, L121

Leconte, J., Baraffe, I., Chabrier, G., Barman, T., & Levrard, B. 2009, *A&A*, **506**, 385

Leconte, J. & Chabrier, G. 2012, *A&A*, **540**, A20

Léger, A., Rouan, D., Schneider, J., Barge, P., Fridlund, M., Samuel, B., Ollivier, M., Guenther, E., Deleuil, M., Deeg, H. J., Auvergne, M., Alonso, R., Aigrain, S., Alapini, A., Almenara, J. M., Baglin, A., Barbieri, M., Bruntt, H., Bordé, P., Bouchy, F.,

Cabrera, J., Catala, C., Carone, L., Carpano, S., Csizmadia, S., Dvorak, R., Erikson, A., Ferraz-Mello, S., Foing, B., Fressin, F., Gandolfi, D., Gillon, M., Gondoin, P., Grasset, O., Guillot, T., Hatzes, A., Hébrard, G., Jorda, L., Lammer, H., Llebaria, A., Loeillet, B., Mayor, M., Mazeh, T., Moutou, C., Pätzold, M., Pont, F., Queloz, D., Rauer, H., Renner, S., Samadi, R., Shporer, A., Sotin, C., Tingley, B., Wuchterl, G., Adda, M., Agogu, P., Appourchaux, T., Ballans, H., Baron, P., Beaufort, T., Bellenger, R., Berlin, R., Bernardi, P., Blouin, D., Baudin, F., Bodin, P., Boisnard, L., Boit, L., Bonneau, F., Borzeix, S., Briet, R., Buey, J.-T., Butler, B., Cailleau, D., Cautain, R., Chabaud, P.-Y., Chaintreuil, S., Chiavassa, F., Costes, V., Cuna Parrho, V., de Oliveira Fialho, F., Decaudin, M., Defise, J.-M., Djalal, S., Epstein, G., Exil, G.-E., Fauré, C., Fenouillet, T., Gaboriaud, A., Gallic, A., Gamet, P., Gavalda, P., Grolleau, E., Gruneisen, R., Gueguen, L., Guis, V., Guivarc'h, V., Guterman, P., Hallouard, D., Hasiba, J., Heuripeau, F., Huntzinger, G., Hustaix, H., Imad, C., Imbert, C., Johlander, B., Jouret, M., Journoud, P., Karioty, F., Kerjean, L., Lafaille, V., Lafond, L., Lam-Trong, T., Landiech, P., Lapeyrere, V., Larqué, T., Laudet, P., Lautier, N., Lecann, H., Lefevre, L., Leruyet, B., Levacher, P., Magnan, A., Mazy, E., Mertens, F., Mesnager, J.-M., Meunier, J.-C., Michel, J.-P., Monjoin, W., Naudet, D., Nguyen-Kim, K., Orcesi, J.-L., Ottacher, H., Perez, R., Peter, G., Plasson, P., Plesseria, J.-Y., Pontet, B., Pradines, A., Quentin, C., Reynaud, J.-L., Rolland, G., Rollenhagen, F., Romagnan, R., Russ, N., Schmidt, R., Schwartz, N., Sebbag, I., Sedes, G., Smit, H., Steller, M. B., Sunter, W., Surace, C., Tello, M., Tiphène, D., Toulouse, P., Ulmer, B., Vandermarcq, O., Vergnault, E., Vuillemin, A., & Zanatta,

P. 2009, *A&A*, **506**, 287

Levrard, B., Correia, A. C. M., Chabrier, G., Baraffe, I., Selsis, F., & Laskar, J. 2007, *A&A*, **462**, L5

Levrard, B., Winisdoerffer, C., & Chabrier, G. 2009, *ApJ*, **692**, L9

Li, S., Miller, N., Lin, D., & Fortney, J. 2009, *Nature, submitted*

Lin, D. N. C., Bodenheimer, P., & Richardson, D. C. 1996, *Nat*, **380**, 606

Lissauer, J. J., Fabrycky, D. C., Ford, E. B., Borucki, W. J., Fressin, F., Marcy, G. W., Orosz, J. A., Rowe, J. F., Torres, G., Welsh, W. F., Batalha, N. M., Bryson, S. T., Buchhave, L. A., Caldwell, D. A., Carter, J. A., Charbonneau, D., Christiansen, J. L., Cochran, W. D., Desert, J.-M., Dunham, E. W., Fanelli, M. N., Fortney, J. J., Gautier, III, T. N., Geary, J. C., Gilliland, R. L., Haas, M. R., Hall, J. R., Holman, M. J., Koch, D. G., Latham, D. W., Lopez, E., McCauliff, S., Miller, N., Morehead, R. C., Quintana, E. V., Ragozzine, D., Sasselov, D., Short, D. R., & Steffen, J. H. 2011, *Nat*, **470**, 53

Liu, X., Burrows, A., & Ibgui, L. 2008, *ApJ*, **687**, 1191

Lopez, E. D., Fortney, J. J., & Miller, N. 2012, *ApJ*, **761**, 59

Lyon, S. P. & Johnson, J. D. 1992, *LANL Rep. LA-UR-92-3407 (Los Alamos: LANL)*

Mardling, R. A. 2007, *MNRAS*, **382**, 1768

Marley, M. S., Fortney, J., Seager, S., & Barman, T. 2007, in B. Reipurth, D. Jewitt, & K. Keil (eds.), *Protostars and Planets V*, pp 733–747

Mayor, M. & Queloz, D. 1995, *Nat*, **378**, 355+

McCullough, P. R., Burke, C. J., Valenti, J. A., Long, D., Johns-Krull, C. M., Machalek, P., Janes, K. A., Taylor, B., Gregorio, J., Foote, C. N., Gary, B. L., Fleenor, M., García-Melendo, E., & Vanmunster, T. 2008, *ApJ submitted, ArXiv e-prints/0805.2921*

Miller, N., Fortney, J. J., & Jackson, B. 2009, *ApJ*, **702**, 1413

Mizuno, H. 1980, *Progress of Theoretical Physics*, **64**, 544

Mordasini, C., Alibert, Y., & Benz, W. 2009, *A&A*, **501**, 1139

Nagasawa, M., Ida, S., & Bessho, T. 2008, *ApJ*, **678**, 498

Nayakshin, S. 2010, *MNRAS*, **408**, 2381

Nutzman, P., Gilliland, R. L., McCullough, P. R., Charbonneau, D., Christensen-Dalsgaard, J., Kjeldsen, H., Nelan, E. P., Brown, T. M., & Holman, M. J. 2010, *ArXiv e-prints*

Ogilvie, G. I. & Lin, D. N. C. 2004, *ApJ*, **610**, 477

Ogilvie, G. I. & Lin, D. N. C. 2007, *ApJ*, **661**, 1180

Papaloizou, J. C. B., Nelson, R. P., Kley, W., Masset, F. S., & Artymowicz, P. 2007, in B. Reipurth, D. Jewitt, & K. Keil (eds.), *Protostars and Planets V*, pp 655–668

Paxton, B., Bildsten, L., Dotter, A., Herwig, F., Lesaffre, P., & Timmes, F. 2011, *ApJS*, **192**, 3

Peale, S. J. 2008, in D. Fischer, F. A. Rasio, S. E. Thorsett, & A. Wolszczan (eds.), *Astronomical Society of the Pacific Conference Series*, Vol. 398 of *Astronomical Society of the Pacific Conference Series*, pp 281–+

Pollack, J. B., Hubickyj, O., Bodenheimer, P., Lissauer, J. J., Podolak, M., & Greenzweig, Y. 1996, *Icarus*, **124**, 62

Queloz, D., Anderson, D., Collier Cameron, A., Gillon, M., Hebb, L., Hellier, C., Maxted, P., Pepe, F., Pollacco, D., Ségransan, D., Smalley, B., Triaud, A. H. M. J., Udry, S., & West, R. 2010, *A&A*, **517**, L1+

Rasio, F. A. & Ford, E. B. 1996, *Science*, **274**, 954

Ribas, I., Guinan, E. F., Güdel, M., & Audard, M. 2005, *ApJ*, **622**, 680

Robinson, S. E., Laughlin, G., Bodenheimer, P., & Fischer, D. 2006, *ApJ*, **643**, 484

Sato, B., Fischer, D. A., Henry, G. W., Laughlin, G., Butler, R. P., Marcy, G. W., Vogt, S. S., Bodenheimer, P., Ida, S., Toyota, E., Wolf, A., Valenti, J. A., Boyd, L. J., Johnson, J. A., Wright, J. T., Ammons, M., Robinson, S., Strader, J., McCarthy, C., Tah, K. L., & Minniti, D. 2005, *ApJ*, **633**, 465

Saumon, D., Chabrier, G., & van Horn, H. M. 1995, *ApJS*, **99**, 713

Stevenson, D. J. 1985, *Icarus*, **62**, 4

Stevenson, D. J. & Salpeter, E. E. 1977a, *ApJS*, **35**, 239

Stevenson, D. J. & Salpeter, E. E. 1977b, *ApJS*, **35**, 221

Thommes, E. W., Matsumura, S., & Rasio, F. A. 2008, *Science*, **321**, 814

Thompson, S. L. 1990, *ANEOS—Analytic Equations of State for Shock Physics Codes, Sandia Natl. Lab. Doc. SAND89-2951*

Timmes, F. X. & Swesty, F. D. 2000, *ApJS*, **126**, 501

Torres, G., Winn, J. N., & Holman, M. J. 2008, *ApJ*, **677**, 1324

Valencia, D., Ikoma, M., Guillot, T., & Nettelmann, N. 2010, *A&A*, **516**, A20

Ward, W. R. 1997a, *Icarus*, **126**, 261

Ward, W. R. 1997b, *ApJ*, **482**, L211

Weidenschilling, S. J. & Marzari, F. 1996, *Nat*, **384**, 619

Wilson, H. F. & Militzer, B. 2012a, *Physical Review Letters*, **108(11)**, 111101

Wilson, H. F. & Militzer, B. 2012b, *ApJ*, **745**, 54

Winn, J. N. & Holman, M. J. 2005, *ApJ*, **628**, L159

Winn, J. N., Johnson, J. A., Narita, N., Suto, Y., Turner, E. L., Fischer, D. A., Butler, R. P., Vogt, S. S., O'Donovan, F. T., & Gaudi, B. S. 2008, *ApJ*, **682**, 1283

Winn, J. N., Johnson, J. A., Peek, K. M. G., Marcy, G. W., Bakos, G. Á., Enya, K., Narita, N., Suto, Y., Turner, E. L., & Vogt, S. S. 2007, *ApJ*, **665**, L167

Wisdom, J. 2008, *Icarus*, **193**, 637

Wright, J. T., Fakhouri, O., Marcy, G. W., Han, E., Feng, Y., Johnson, J. A., Howard, A. W., Fischer, D. A., Valenti, J. A., Anderson, J., & Piskunov, N. 2011, *PASP*, **123**, 412

Wu, Y. & Lithwick, Y. 2011, *ApJ*, **735**, 109

Yelle, R., Lammer, H., & Ip, W.-H. 2008, *Space Sci. Rev.*, **139**, 437

Appendix A

Thermodynamic Transformations

A.1 Thermodynamic Transformations

The mixing equation of state performs various transformations from the MESA equation of state representation to derivatives of $log(P)$, $log(E)$, and $log(S)$. These transformations are done to perform the additive volume calculation.

Recall that the additive volume rule is

$$v(P,T) = \sum X_i v_i(P,T) \tag{A.1}$$

$$E(P,T) = \sum X_i E_i(P,T) \tag{A.2}$$

$$S(P,T) = \sum X_i S_i(P,T) \tag{A.3}$$

where $v = 1/\rho$ is the specific volume, E is the internal energy, S is the entropy, and X_i

is the mixture mass fraction. Derivatives of these values are then

$$\partial v(P,T) = \sum X_i(\partial v_i(P,T)) \quad \text{(A.4)}$$

$$\partial E(P,T) = \sum X_i(\partial E_i(P,T)) \quad \text{(A.5)}$$

$$\partial S(P,T) = \sum X_i(\partial S_i(P,T)) \quad \text{(A.6)}$$

where ∂ denotes first and second derivatives with respect to P or T.

All of these can be found in the file mixeos/private/thermo.f.

A.2 Converting from MESA/results format to lnDerivs

The value, first, and second derivatives are encoded in a vector called "lnDerivs". For example, vector lnPvect is determined from the MESA eos as follows

```
lnPvect(i_val)        = res(i_lnPgas)
lnPvect(i_dlnRho)     = d_dlnRho(i_lnPgas)
lnPvect(i_dlnT)       = d_dlnT(i_lnPgas)
lnPvect(i_dlnRho2)    = d_dlnRho(i_chiRho)
lnPvect(i_dlnT2)      = d_dlnT(i_chiT)
lnPvect(i_dlnRhodlnT) = d_dlnRho(i_chiT)
```

Similarly for lnS

```
lnSvect(i_val) = res(i_lnS)
lnSvect(i_dlnRho) = d_dlnRho(i_lnS)
lnSvect(i_dlnT) =   d_dlnT(i_lnS)
lnSvect(i_dlnRho2) = (d/S) * d_dlnRho(i_dS_dRho) &
                      - lnSvect(i_dlnRho)**2d0 &
                      + lnSvect(i_dlnRho)
lnSvect(i_dlnT2) =  (T/S) * d_dlnT(i_dS_dT) &
                    - lnSvect(i_dlnT)**2d0 &
                    + lnSvect(i_dlnT)
lnSvect(i_dlnRhodlnT) = (d/S) * d_dlnT(i_dS_dRho) &
                        - lnSvect(i_dlnRho) * lnSvect(i_dlnT)
```

and lnE

```
lnEvect(i_val)        = res(i_lnE)
lnEvect(i_dlnRho)     = d_dlnRho(i_lnE)
lnEvect(i_dlnT)       = d_dlnT(i_lnE)
lnEvect(i_dlnRho2)    = (d/E) * d_dlnRho(i_dE_dRho) &
                        - lnEvect(i_dlnRho)**2d0 &
                        + lnEvect(i_dlnRho)
lnEvect(i_dlnT2)      = (T/E) * d_dlnT(i_Cv) &
                        - lnEvect(i_dlnT)**2d0  &
                        +  lnEvect(i_dlnT)
lnEvect(i_dlnRhodlnT) = (d/E) * d_dlnT(i_dE_dRho) &
                        - lnEvect(i_dlnRho) * lnEvect(i_dlnT)
```

A.2.1 Transforming from $\ln P(\ln \rho, T)$ to MESA EOS results vector

```
res(:) = 0.
d_dlnRho_c_T(:) = 0.
d_dlnT_c_Rho(:) = 0.

lnP = lnPvect(i_val)
lnE = lnEvect(i_val)
lnS = lnSvect(i_val)

dlnPdlnRho_ct =       lnPvect(i_dlnRho)
dlnPdlnT_cd =         lnPvect(i_dlnT)
d2lnPdlnRho2_ct =     lnPvect(i_dlnRho2)
d2lnPdlnT2_cd =       lnPvect(i_dlnT2)
d2lnPdlnRhodlnT =     lnPvect(i_dlnRhodlnT)

dlnEdlnRho_ct =       lnEvect(i_dlnRho)
dlnEdlnT_cd =         lnEvect(i_dlnT)
d2lnEdlnRho2_ct =     lnEvect(i_dlnRho2)
d2lnEdlnT2_cd =       lnEvect(i_dlnT2)
d2lnEdlnRhodlnT =     lnEvect(i_dlnRhodlnT)

dlnSdlnRho_ct =       lnSvect(i_dlnRho)
dlnSdlnT_cd =         lnSvect(i_dlnT)
d2lnSdlnRho2_ct =     lnSvect(i_dlnRho2)
d2lnSdlnT2_cd =       lnSvect(i_dlnT2)
d2lnSdlnRhodlnT =     lnSvect(i_dlnRhodlnT)

d = exp(lnRho)
```

```
T = exp(lnT)
P = exp(lnP)
E = exp(lnE)
S = exp(lnS)

Cv = (E/T) * dlnEdlnT_cd
dCvdlnRho_ct = (E / T) * dlnEdlnRho_ct * dlnEdlnT_cd &
     + (E / T) * d2lnEdlnRhodlnT
dCvdlnT_cd = (E / T) * dlnEdlnT_cd**2 &
     - (E / T) * dlnEdlnT_cd + (E/T) * d2lnEdlnT2_cd

alpha = dlnPdlnT_cd / (T*dlnPdlnRho_ct)
dalphadlnRho_ct = d2lnPdlnRhodlnT / (T*dlnPdlnRho_ct) &
     - (dlnPdlnT_cd*d2lnPdlnRho2_ct) / (T*dlnPdlnRho_ct**2)
dalphadlnT_cd = d2lnPdlnT2_cd / (T * dlnPdlnRho_ct) &
     - alpha &
     - (dlnPdlnT_cd * d2lnPdlnRhodlnT) / (T * dlnPdlnRho_ct**2)

beta = 1/(P * dlnPdlnRho_ct)
dbetadlnRho_ct = - dlnPdlnRho_ct / (P * dlnPdlnRho_ct) &
     - d2lnPdlnRho2_ct / (P * dlnPdlnRho_ct)
dbetadlnT_cd = - dlnPdlnT_cd / (P * dlnPdlnRho_ct) &
     - d2lnPdlnRhodlnT / (P * dlnPdlnRho_ct**2)

Cp = -(E/T) * dlnPdlnT_cd * dlnEdlnRho_ct / dlnPdlnRho_ct &
   + (E/T) * dlnEdlnT_cd &
   + (P/(d*T))*dlnPdlnT_cd/dlnPdlnRho_ct

dCpdlnRho_ct = &
     -(E/T)*dlnEdlnRho_ct*dlnPdlnT_cd*dlnEdlnRho_ct/dlnPdlnRho_ct &
     -(E/T)*d2lnPdlnRhodlnT*dlnEdlnRho_ct/dlnPdlnRho_ct &
     -(E/T)*dlnPdlnT_cd*d2lnEdlnRho2_ct/dlnPdlnRho_ct &
     +(E/T)*dlnPdlnT_cd*dlnEdlnRho_ct&
           *d2lnPdlnRho2_ct/dlnPdlnRho_ct**2d0 &
     +(E/T)*dlnEdlnRho_ct*dlnEdlnT_cd&
     +(E/T)*d2lnEdlnRhodlnT &
     +(P/(d*T))*dlnPdlnT_cd&
     -(P/(d*T))*dlnPdlnT_cd/dlnPdlnRho_ct&
     +(P/(d*T))*d2lnPdlnRhodlnT/dlnPdlnRho_ct&
     -(P/(d*T))*dlnPdlnT_cd*d2lnPdlnRho2_ct/dlnPdlnRho_ct**2d0
dCpdlnT_cd = &
     -(E/T)*dlnEdlnT_cd*dlnPdlnT_cd*dlnEdlnRho_ct/dlnPdlnRho_ct&
     +(E/T)*dlnPdlnT_cd*dlnEdlnRho_ct/dlnPdlnRho_ct&
```

```
     -(E/T)*d2lnPdlnT2_cd*dlnEdlnRho_ct/dlnPdlnRho_ct&
     -(E/T)*dlnPdlnT_cd*d2lnEdlnRhodlnT/dlnPdlnRho_ct&
     +(E/T)*dlnPdlnT_cd*dlnEdlnRho_ct&
           *d2lnPdlnRhodlnT/dlnPdlnRho_ct**2d0&
     +(E/T)*dlnEdlnT_cd**2&
     -(E/T)*dlnEdlnT_cd&
     +(E/T)*d2lnEdlnT2_cd&
     +(P/(d*T))*dlnPdlnT_cd**2d0 / dlnPdlnRho_ct &
     -(P/(d*T))*dlnPdlnT_cd / dlnPdlnRho_ct&
     +(P/(d*T))*d2lnPdlnT2_cd / dlnPdlnRho_ct&
     -(P/(d*T))*dlnPdlnT_cd*d2lnPdlnRhodlnT/dlnPdlnRho_ct**2d0!&

res(i_lnPgas) = lnP
d_dlnRho_c_T(i_lnPgas) = dlnPdlnRho_ct
d_dlnT_c_Rho(i_lnPgas) = dlnPdlnT_cd
res(i_lnE) = lnE
d_dlnRho_c_T(i_lnE) = dlnEdlnRho_ct
d_dlnT_c_Rho(i_lnE) = dlnEdlnT_cd
res(i_lnS) = lnS
d_dlnRho_c_T(i_lnS) = dlnSdlnRho_ct
d_dlnT_c_Rho(i_lnS) = dlnSdlnT_cd

res(i_Cp) = Cp
d_dlnT_c_Rho(i_Cp) = dCpdlnT_cd
d_dlnRho_c_T(i_Cp) = dCpdlnRho_ct

res(i_grad_ad) = 1.d0/(-dlnSdlnT_cd*dlnPdlnRho_ct/dlnSdlnRho_ct &
                       + dlnPdlnT_cd)
d_dlnRho_c_T(i_grad_ad) = (- res(i_grad_ad)**2d0) &
   *(-d2lnSdlnRhodlnT*dlnPdlnRho_ct/dlnSdlnRho_ct &
     -dlnSdlnT_cd*d2lnPdlnRho2_ct/dlnSdlnRho_ct &
      +dlnSdlnT_cd*d2lnSdlnRho2_ct*
           *dlnPdlnRho_ct/(dlnSdlnRho_ct**2d0) &
      + d2lnPdlnRhodlnT)
d_dlnT_c_Rho(i_grad_ad) = (- res(i_grad_ad)**2d0) &
    * (-d2lnSdlnT2_cd*dlnPdlnRho_ct/dlnSdlnRho_ct &
       -dlnSdlnT_cd * d2lnPdlnRhodlnT/dlnSdlnRho_ct &
       +dlnSdlnT_cd * d2lnSdlnRhodlnT&
          * dlnPdlnRho_ct/(dlnSdlnRho_ct**2d0) &
       +d2lnPdlnT2_cd)

res(i_chiRho) = dlnPdlnRho_ct
d_dlnRho_c_T(i_chiRho) = d2lnPdlnRho2_ct
```

```
d_dlnT_c_Rho(i_chiRho) = d2lnPdlnRhodlnT

res(i_chiT) = dlnPdlnT_cd
d_dlnRho_c_T(i_chiT) = d2lnPdlnRhodlnT
d_dlnT_c_Rho(i_chiT) = d2lnPdlnT2_cd

res(i_Cv) = (E / T) * dlnEdlnT_cd
d_dlnRho_c_T(i_Cv) = (E / T) * dlnEdlnRho_ct * dlnEdlnT_cd &
                   + (E / T) * d2lnEdlnRhodlnT
d_dlnT_c_Rho(i_Cv) = (E / T) * dlnEdlnT_cd**2d0 &
                   - (E / T) * dlnEdlnT_cd &
                   + (E / T) * d2lnEdlnT2_cd

res(i_dE_dRho) = dlnEdlnRho_ct * E / d
d_dlnRho_c_T(i_dE_dRho) = (E / d) * dlnEdlnRho_ct**2 &
                        - (E / d)*dlnEdlnRho_ct &
                        + (E / d)*d2lnEdlnRho2_ct
d_dlnT_c_Rho(i_dE_dRho) = (E/d) * dlnEdlnT_cd * dlnEdlnRho_ct &
                        + (E/d) * d2lnEdlnRhodlnT

res(i_dS_dT) = (S / T) * dlnSdlnT_cd
d_dlnRho_c_T(i_dS_dt) = (S / T) * dlnSdlnRho_ct * dlnSdlnT_cd &
                      + (S / T) * d2lnSdlnRhodlnT
d_dlnT_c_Rho(i_dS_dt) = (S / T) * dlnSdlnT_cd**2d0 &
                      - (S / T) * dlnSdlnT_cd &
                      + (S / T) * d2lnSdlnT2_cd

(i_dS_dRho) = (S / d) * dlnSdlnRho_ct
d_dlnRho_c_T(i_dS_dRho) = (S / d) * dlnSdlnRho_ct**2d0 &
            - (S / d)*dlnSdlnRho_ct &
            + (S / d) * d2lnSdlnRho2_ct
d_dlnT_c_Rho(i_dS_dRho) = (S/d) * dlnSdlnT_cd * dlnSdlnRho_ct &
                        + (S/d) * d2lnSdlnRhodlnT

res(i_gamma1) = dlnPdlnRho_ct-dlnSdlnRho_ct&
                   *dlnPdlnT_cd/dlnSdlnT_cd
d_dlnRho_c_T(i_gamma1) = d2lnPdlnRho2_ct &
             -d2lnSdlnRho2_ct*dlnPdlnT_cd/dlnSdlnT_cd &
             -dlnSdlnRho_ct*d2lnPdlnRhodlnT/dlnSdlnT_cd &
             +dlnSdlnRho_ct*d2lnSdlnRhodlnT&
                *dlnPdlnT_cd/dlnSdlnT_cd**2
d_dlnT_c_Rho(i_gamma1) = d2lnPdlnRhodlnT &
             -d2lnSdlnRhodlnT*dlnPdlnT_cd/dlnSdlnT_cd&
```

```
              -dlnSdlnRho_ct*d2lnPdlnT2_cd/dlnSdlnT_cd&
              +dlnSdlnRho_ct*d2lnSdlnT2_cd*
                 *dlnPdlnT_cd/dlnSdlnT_cd**2
res(i_gamma3) = 1 - dlnSdlnRho_ct/dlnSdlnT_cd
d_dlnT_c_Rho(i_gamma3) = -d2lnSdlnRho2_cT/dlnSdlnT_cd &
              + dlnSdlnRho_ct*d2lnSdlnRhodlnT/dlnSdlnT_cd**2
d_dlnRho_c_T(i_gamma3) = -d2lnSdlnRhodlnT/dlnSdlnT_cd &
              +dlnSdlnRho_ct*d2lnSdlnT2_cd/dlnSdlnT_cd**2
```

A.2.2 Transformation from free energy derivatives to P,E,S derivatives

In the case of the ideal gas law, I have initially represented the equation of state using free energy derivatives. I then use the following thermodynamic variables to get derivatives of P, E, and S with respect to ρ and T. Of course, before these are added with other species, they must be transformed into $\rho(P,T)$, $E(P,T)$, and $S(P,T)$ and the first and second derivatives.

$$P = \rho^2 * \frac{\partial F}{\partial \rho} \tag{A.7}$$

$$\frac{\partial P}{\partial \rho} = 2\rho\frac{\partial F}{\partial \rho} + \rho^2 * \frac{\partial^2 F}{\partial \rho^2} \tag{A.8}$$

$$\frac{\partial P}{\partial T} = \rho^2\frac{\partial^2 F}{\partial \rho \partial T} \tag{A.9}$$

$$\frac{\partial^2 P}{\partial \rho^2} = 2\frac{\partial F}{\partial \rho} + 4\rho\frac{\partial^2 F}{\partial \rho^2} + \rho^2\frac{\partial^3 F}{\partial \rho^3} \tag{A.10}$$

$$\frac{\partial^2 P}{\partial \rho \partial T} = 2\rho\frac{\partial^2 F}{\partial \rho \partial T} + \rho^2\frac{\partial^3 F}{\partial \rho^2 \partial T} \tag{A.11}$$

$$\frac{\partial^2 P}{\partial T^2} = \rho^2\frac{\partial^3 F}{\partial \rho \partial T^2} \tag{A.12}$$

$$E = F - T\frac{\partial F}{\partial T} \tag{A.13}$$
$$\frac{\partial E}{\partial \rho} = \frac{\partial F}{\partial \rho} - T\frac{\partial^2 F}{\partial \rho \partial T} \tag{A.14}$$
$$\frac{\partial E}{\partial T} = -T\frac{\partial^2 F}{\partial T^2} \tag{A.15}$$
$$\frac{\partial^2 E}{\partial \rho^2} = \frac{\partial^2 F}{\partial \rho^2} - T\frac{\partial^3 F}{\partial \rho^2 \partial T} \tag{A.16}$$
$$\frac{\partial^2 E}{\partial \rho \partial T} = -T\frac{\partial^3 F}{\partial \rho \partial T^2} \tag{A.17}$$
$$\frac{\partial^2 E}{\partial T^2} = -\frac{\partial^2 F}{\partial T^2} - T\frac{\partial^3 F}{\partial T^3} \tag{A.18}$$

$$S = -\frac{\partial F}{\partial T} \tag{A.19}$$
$$\frac{\partial S}{\partial \rho} = -\frac{\partial^2 F}{\partial \rho \partial T} \tag{A.20}$$
$$\frac{\partial S}{\partial T} = -\frac{\partial^2 F}{\partial T^2} \tag{A.21}$$
$$\frac{\partial^2 S}{\partial \rho^2} = -\frac{\partial^3 F}{\partial \rho^2 \partial T} \tag{A.22}$$
$$\frac{\partial^2 S}{\partial \rho \partial T} = -\frac{\partial^3 F}{\partial \rho \partial T^2} \tag{A.23}$$
$$\frac{\partial^2 S}{\partial T^2} = -\frac{\partial^3 F}{\partial T^3} \tag{A.24}$$

A.3 Ideal Gas Implementation

The ideal gas implementation is fairly straightforward. I use the analytic expression for the free energy to determine first, second and third derivatives. I then use thermodynamic identities to determine the eos in terms of P,E,S derivatives format.

```
!! Powers are calculated just once
rho2 = rho*rho
rho3 = rho2 * rho
T2 = T*T

!! Get free energy derivatives of the ideal EOS
f_val = -(N_A / this%mu) * k_pc * T &
  * ( - lnRho - this%lnN_A_mu - this%lnalpha + 1.5 * lnT + 1.)
df_drho =  (N_A / this%mu) * k_pc * T / rho
df_dt = -(N_A / this%mu) * k_pc &
  * ( - lnRho - this%lnN_A_mu - this%lnalpha + 1.5 * lnT + 2.5)
d2f_drho2 = -(N_A / this%mu) * k_pc * T / rho2
d2f_dt2 =  -(N_A / this%mu) * 1.5 * k_pc  / T
d2f_drhodt =  (N_A / this%mu) * k_pc / rho
d3f_drho3 = (N_A / this%mu) * 2.d0 * k_pc * T / rho3
d3f_drho2dt = -(N_A / this%mu) * k_pc / rho2
d3f_drhodt2 = 0.d0
d3f_dt3 = (N_A / this%mu) * 1.5 * k_pc / T2
d4f_drho2dt2 = 0.d0

!! Convert the Free Energy Derivatives into P, E, S & derivatives
Pvect(i_val) = Rho2 * df_drho
Pvect(i_drho) = Rho2 * d2f_drho2 + 2 * rho * df_drho
Pvect(i_dt) = Rho2 * d2f_drhodt
Pvect(i_drho2) = Rho2 * d3f_drho3 &
         + 4. * rho * d2f_drho2 + 2. * df_drho
Pvect(i_dt2) = Rho2 * d3f_drhodt2
Pvect(i_drhodt) = Rho2 * d3f_drho2dt + 2. * rho * d2f_drhodt

Svect(i_val) = -df_dt
Svect(i_drho) = -d2f_drhodt
Svect(i_dt) = -d2f_dt2
Svect(i_drho2) = -d3f_drho2dt
Svect(i_dt2) = - d3f_dt3
Svect(i_drhodt) = - d3f_drhodt2

Evect(i_val) = f_val - T * df_dt
Evect(i_drho) = df_drho - T * d2f_drhodt
Evect(i_dt) = -T * d2f_dt2
Evect(i_drho2) = d2f_drho2 - T*d3f_drho2dt
Evect(i_dt2) = -d2f_dt2 - T * d3f_dt3
Evect(i_drhodt) = - T * d3f_drhodt2
```